สมบัติเชิงเคมีไฟฟ้าของสารประกอบเพอรอฟสไกต์แบบชั้น $(Ln_xSr_{4-x}M_yFe_{6-y}O_{13+\delta}$; Ln = La, Pr, Sm และ M = Co, Ni) เพื่อใช้เป็นแคโทดสำหรับเซลล์เชื้อเพลิงออกไซด์แข็งที่อุณหภูมิปานกลาง

นายกิตติวัฒน์ กำลังเสือ

จุฬาลงกรณ์มหาวิทยาลัย
Chulalongkorn University

บทคัดย่อและแฟ้มข้อมูลฉบับเต็มของวิทยานิพนธ์ตั้งแต่ปีการศึกษา 2554 ที่ให้บริการในคลังปัญญาจุฬาฯ (CUIR)
เป็นแฟ้มข้อมูลของนิสิตเจ้าของวิทยานิพนธ์ ที่ส่งผ่านทางบัณฑิตวิทยาลัย
The abstract and full text of theses from the academic year 2011 in Chulalongkorn University Intellectual Repository (CUIR)
are the thesis authors' files submitted through the University Graduate School.

วิทยานิพนธ์นี้เป็นส่วนหนึ่งของการศึกษาตามหลักสูตรปริญญาวิทยาศาสตรมหาบัณฑิต
สาขาวิชาเคมี ภาควิชาเคมี
คณะวิทยาศาสตร์ จุฬาลงกรณ์มหาวิทยาลัย
ปีการศึกษา 2559
ลิขสิทธิ์ของจุฬาลงกรณ์มหาวิทยาลัย

ELECTROCHEMICAL PROPERTIES OF LAYERED PEROVSKITE ($Ln_xSr_{4-x}M_yFe_{6y}O_{13+\delta}$; Ln = La, Pr, Sm AND M = Co, Ni) AS CATHODES FOR INTERMEDIATE - TEMPERATURE SOLID OXIDE FUEL CELLS

Mr. Kittiwat Kamlungsua

จุฬาลงกรณ์มหาวิทยาลัย
Chulalongkorn University

A Thesis Submitted in Partial Fulfillment of the Requirements
for the Degree of Master of Science Program in Chemistry
Department of Chemistry
Faculty of Science
Chulalongkorn University
Academic Year 2016

Copyright of Chulalongkorn University

Thesis Title	ELECTROCHEMICAL PROPERTIES OF LAYERED PEROVSKITE ($Ln_xSr_{4-x}M_yFe_{6y}O_{13+\delta}$; Ln = La, Pr, Sm AND M = Co, Ni) AS CATHODES FORINTERMEDIATE - TEMPERATURE SOLID OXIDE FUEL CELLS
By	Mr. Kittiwat Kamlungsua
Field of Study	Chemistry
Thesis Advisor	Assistant Professor Soamwadee Chaianansutcharit, Ph.D.
Thesis Co-Advisor	Chanapa Kongmark, Ph.D.

Accepted by the Faculty of Science, Chulalongkorn University in Partial Fulfillment of the Requirements for the Master's Degree

.....Dean of the Faculty of Science
(Associate Professor Polkit Sangvanich, Ph.D.)

THESIS COMMITTEE

.....Chairman
(Associate Professor Vudhichai Parasuk, Ph.D.)

.....Thesis Advisor
(Assistant Professor Soamwadee Chaianansutcharit, Ph.D.)

.....Thesis Co-Advisor
(Chanapa Kongmark, Ph.D.)

.....Examiner
(Wipark Anutrasakda, Ph.D.)

.....External Examiner
(Assistant Professor Jinda Yeyongchaiwat, Ph.D.)

กิตติวัฒน์ กำลังเสือ : สมบัติเชิงเคมีไฟฟ้าของสารประกอบเพอรอฟสไกต์แบบชั้น ($Ln_xSr_{4-x}M_yFe_{6-y}O_{13+\delta}$; Ln = La, Pr, Sm และ M = Co, Ni) เพื่อใช้เป็นแคโทดสำหรับเซลล์เชื้อเพลิงออกไซด์แข็งที่อุณหภูมิปานกลาง (ELECTROCHEMICAL PROPERTIES OF LAYERED PEROVSKITE (Ln_xSr_{4-x} $M_yFe_{6y}O_{13+\delta}$; Ln = La, Pr, Sm AND M = Co, Ni) AS CATHODES FORINTERMEDIATE - TEMPERATURE SOLID OXIDE FUEL CELLS) อ.ที่ปรึกษาวิทยานิพนธ์หลัก: ผศ. ดร.โสมวดี ไชยอนันต์สุจริต, อ.ที่ปรึกษาวิทยานิพนธ์ร่วม: ดร.ชนาภา คงมาก, 84 หน้า.

ศึกษาสมบัติของเพอรอฟสไกต์แบบชั้น $Sr_4Fe_6O_{13}$, $La_xSr_{4-x}Fe_6O_{13}$, $Pr_xSr_{4-x}Fe_6O_{13}$, $Sm_xSr_{4-x}Fe_6O_{13}$, $Sr_4Co_xFe_{6-x}O_{13}$, และ $Sr_4Ni_xFe_{6-x}O_{13}$สำหรับใช้เป็นแคโทดในเซลล์เชื้อเพลิงออกไซด์แข็งที่อุณหภูมิปานกลาง วัสดุดังกล่าวสามารถเตรียมได้จากปฏิกิริยาที่สภาวะของแข็ง โดยการเผาที่อุณหภูมิ 850 ^oC เป็นเวลา 16 ชั่วโมง และเผาผนึกที่ 1185 ^oC เป็นเวลา 5 ชั่วโมง และวัสดุดังกล่าวแสดงการเปลี่ยนเฟสจากเพอรอฟสไกต์แบบชั้นเป็นเพอรอฟสไกต์เมื่อเพิ่มปริมาณธาตุอื่นที่เติมลงไป นอกจากนี้ การเติม Pr, Sm, และ Co ทำให้ค่าการนำไฟฟ้าเพิ่มขึ้นตามปริมาณธาตุที่เติมสำหรับออกไซด์ของ PSFx, SSFx, และ SFCox แต่การเติม La และ Ni จะเหนี่ยวนำให้เกิดการเปลี่ยนแปลงพฤติกรรมการนำไฟฟ้าจากการนำไฟฟ้าแบบสารกึ่งตัวนำไปสู่การนำไฟฟ้าเชิงโลหะในออกไซด์ของ LSFx และ SFNix ผลการวิเคราะห์ด้วย XPS และการวิเคราะห์เชิงความร้อนแสดงให้เห็นถึงการรักษาสมดุลของประจุที่แตกต่างกันจากการเติมธาตุในกลุ่มแลนทาไนด์และธาตุโลหะทรานซิชัน นอกจากนี้ การเพิ่มปริมาณธาตุที่เติมลงไปส่งผลให้ค่าความต้านทานสำหรับปฏิกิริยารีดักชันของแก๊สออกซิเจนของออกไซด์ทุกกลุ่มลดลง ซึ่งการเพิ่มขึ้นของค่าการนำไฟฟ้าและการลดลงของความต้านทานดังกล่าวสืบเนื่องมาจากการมีอยู่ของวัฏภาคสองวัฏภาคนั่นก็คือ เพอรอฟสไกต์ที่ทำหน้าที่เป็นโครงข่ายต่อเนื่องสำหรับการถ่ายโอนอิเล็กตรอนและเพอรอฟสไกต์แบบชั้นที่ทำหน้าที่เป็นช่องทางสำหรับการแพร่ของออกไซด์ไอออนที่ดี

ภาควิชา เคมี	ลายมือชื่อนิสิต .....
สาขาวิชา เคมี	ลายมือชื่อ อ.ที่ปรึกษาหลัก .....
ปีการศึกษา 2559	ลายมือชื่อ อ.ที่ปรึกษาร่วม .....

5671916523 : MAJOR CHEMISTRY
KEYWORDS: SOLID OXIDE FUEL CELL / LAYERED PEROVSKITE / MULTIPHASE SYSTEM

KITTIWAT KAMLUNGSUA: ELECTROCHEMICAL PROPERTIES OF LAYERED PEROVSKITE ($Ln_xSr_{4-x}M_yFe_{6y}O_{13+\delta}$; Ln = La, Pr, Sm AND M = Co, Ni) AS CATHODES FORINTERMEDIATE - TEMPERATURE SOLID OXIDE FUEL CELLS. ADVISOR: ASST. PROF. SOAMWADEE CHAIANANSUTCHARIT, Ph.D., CO-ADVISOR: CHANAPA KONGMARK, Ph.D., 84 pp.

Layered perovskites, $Sr_4Fe_6O_{13}$, $La_xSr_{4-x}Fe_6O_{13}$, $Pr_xSr_{4-x}Fe_6O_{13}$, $Sm_xSr_{4-x}Fe_6O_{13}$, $Sr_4Co_xFe_{6-x}O_{13}$, and $Sr_4Ni_xFe_{6-x}O_{13}$ have been investigated as cathode materials for intermediate – temperature solid oxide fuel cell (IT-SOFC). All layered oxides were prepared through conventional solid – state reaction method with the respective calcination and sintering temperatures of 850°C for 16 hours and 1185°C for 5 hours and they exhibited a gradual phase transformation from the pure layered phase to the perovskite phase with increasing the dopant content. In addition, the incorporation of Pr, Sm, and Co led to the increasing of electrical conductivity in PSFx, SSFx, and SFCox oxides whereas doping of La and Ni resulted in the transition in electrical conduction from semiconducting to metallic – like behaviours for LSFx and SFNix oxides. XPS analyses and thermogravimetric analyses revealed the different charge compensation mechanisms in lanthanide – and transition metal – containing oxides. The reduction in polarisation resistances with the increased dopant concentration was also observed, in general, for all oxides. The increase in the electrical conductivity and the decrease of the polarisation resistance of the synthesised oxides with increasing the dopant concentration have stemmed from the synergistic effect on the presence of both perovskite and layered phases that provided fast oxide ion diffusion channels and acted as a continuous network for electron transport.

จุฬาลงกรณ์มหาวิทยาลัย
CHULALONGKORN UNIVERSITY

Department:	Chemistry	Student's Signature	.....
Field of Study:	Chemistry	Advisor's Signature	.....
Academic Year:	2016	Co-Advisor's Signature	.....

ACKNOWLEDGEMENTS

I would like to express a deep sense of gratitude to my thesis advisor Assistant Professor Dr. Soamwadee Chaianantsucharit for her valuable advice and encouragement throughout the course of research without hesitation and reluctance, not only academic stuff but also future career path. Moreover, I wish to thank my co – advisor Dr. Chanapa Kongmark who also supports and provides me with technical solutions to tackle the problem at hand and introduces me with a French Professor Rose – Noelle Vannier from Unite de Catalyse et Chimie du Solide at Ecole Nationale Supérieure de Chimie du Solide. Without these supports, I would not have completed my thesis. In addition, I would like to thank Associate Professor Dr. Vudhichai Parasuk as the chairman, Dr. Wipark Anutrasakda and Assistant Professor Dr. Jinda Yeyongchaiwat for serving as the thesis committee.

Acknowledgement is also extended to National Reserch Council of Thailand (NRCT) who provides financial support for Graudate Study Fund (2015) as well as Science Achievement Scholarship of Thailand (SAST) who has granted me a long – term scholarship since undergraduate study.

Finally, I wish to mention and forward a complete gratitude to my family, laboratory colleagues, instrumental technicians for their assistance and sincere determination to push me through difficulties to achieve the ultimate goal.

จุฬาลงกรณ์มหาวิทยาลัย
CHULALONGKORN UNIVERSITY

CONTENTS

Page

Chulalongkorn University

Page

จุฬาลงกรณ์มหาวิทยาลัย
CHULALONGKORN UNIVERSITY

Page

จุฬาลงกรณ์มหาวิทยาลัย
Chulalongkorn University

LIST OF FIGURES

Chulalongkorn University

Chulalongkorn University

จุฬาลงกรณ์มหาวิทยาลัย
Chulalongkorn University

LIST OF TALBES

LIST OF ABBREVIATIONS

SOFC	Solid Oxide Fuel Cell
MCFC	Molten Carbonate Fuel Cell
PAFC	Phosphoric Acid Fuel Cell
AFC	Alkaline Fuel Cell
PEMFC	Polymer Electrolyte Membrane Fuel Cell
XRD	X – ray Diffractometry
TGA	Thermogravimetric Analysis
mm	millimetre
T	absolute temperature
K	Kelvin
σ	specific conductivity
Å	angstrom
E_a	activation energy
R_p	polarisation resistance
L	length
I	current
T	thickness
V	voltage
W	width
Z	impedance
IT	intermediate – temperature
MIEC	mixed ionic – electronic conductor
ORR	oxygen reduction reaction
δ	oxygen non – stoichiometry

CHAPTER I
INTRODUCTION

Due to a rapid growth in human population and the global industrialisation, an immense increase in worldwide energy consumption and the substantial reduction in natural resources, especially fossil fuels, have been triggered and led to environmental deterioration. As a result, other clean and efficient emerging technologies to deal with these problems are needed as alternative sources for the better future. They include; for instance, solar cells, batteries, biofuels, photoelectrochemical conversion of fuels, and fuel cells.

1.1 Fuel Cells [1-4]

Fuel cells are electrochemical devices that convert chemical energy stored in fuels such as hydrogen gas and hydrocarbons into electricity directly. The direct electricity conversion shows an outstanding advantage over other electricity – generating technologies. Typically, fuel cells are classified into five major types according to electrolytes: proton exchange membrane fuel cell or polymer electrolyte membrane fuel cell (PEMFC), phosphoric acid fuel cell (PAFC), alkaline fuel cell (AFC), molten carbonate fuel cell (MCFC), and solid oxide fuel cell (SOFC). Concerning the electrolytes, the first three types of the fuel cells mentioned are operated at low temperature (60 – 220^{o}C) while the latter two are at higher temperature (500 – 1000^{o}C). Therefore, the first three fuel cells yield relatively low conversion efficiency of 40 – 50% but the latter two provide higher efficiency up to 60 %. Among these fuel cells, PEMFCs and SOFCs have attracted much attention than any others because of their high efficiency, fuel flexibility, easy handling, compatibility with other modules, and versatile applications for both stationary and portable devices. The overall properties and specifications of the five types of fuel cells are summarised in Table 1.1.

1.2. Solid Oxide Fuel Cells (SOFCs) [5-10]

Unlike other types of fuel cells, sold oxide fuel cell is operational at fairly higher temperature range, which results in a number of outstanding characteristics and properties. They include high conversion efficiency, clean combustion of fuels and environmental friendliness, fuel adaptability, practical application to cogeneration systems, and ability to miniaturise the whole fuel cell. In addition, SOFCs can provide a wide range of power from watts to megawatts to supply any types of building or devices with sufficient energy.

Table 1. 1 Description of major fuel cell types [11]

	PEMFC	PAFC	AFC	MCFC	SOFC
Electrolyte	Polymer Membrane	Liquid H_3PO_4 (immobilised)	Liquid KOH (immobilised)	Molten Carbonate	Ceramic
Charge Carrier	H^+	H^+	OH^-	CO_3^{2-}	O^{2-}
Operating Temperature	80 °C	200 °C	60 – 220 °C	650 °C	600 – 1000 °C
Catalyst	Platinum	Platinum	Platinum	Nickel	Perovskites (ceramic)
Cell Components	Carbon Based	Carbon Based	Carbon Based	Stainless Based	Ceramic Based
Fuel Compatibility	H_2, Methanol	H_2	H_2	H_2, CH_4	H_2, CH_4, CO
Efficiency	40 – 50 %	40 – 50 %	30 %	50 – 60 %	50 – 60 %

จุฬาลงกรณ์มหาวิทยาลัย
Chulalongkorn University

1.2.1 Principle of Solid Oxide Fuel Cells [5]

Like other electrochemical devices, a typical solid oxide fuel cell consists of three main parts: an oxide ion – conducting electrolyte which is sandwiched between the two electrodes, cathode and anode. During the fuel cell operation, the oxygen gas or air is fed into the cathode compartment and it subsequently undergoes the oxygen reduction reaction (ORR) which involves the conversion of molecular oxygens (O_2) into oxide ions (O^{2-}). After that, the oxide ions migrate through the cathode – electrolyte interface into the ceramic electrolyte and then to the anode compartment. At the anode, hydrogen gas is fed and then oxidised, which releases electrons into the external circuit to produce electricity, and the oxidation product combines with the oxide ions to form water as a by – product. The electrons generated from the oxidation of the hydrogen are transferred to the cathode compartment to complete the cell circuit. The overall process for the conversion of fuels into electricity is illustrated in Figure 1.1.

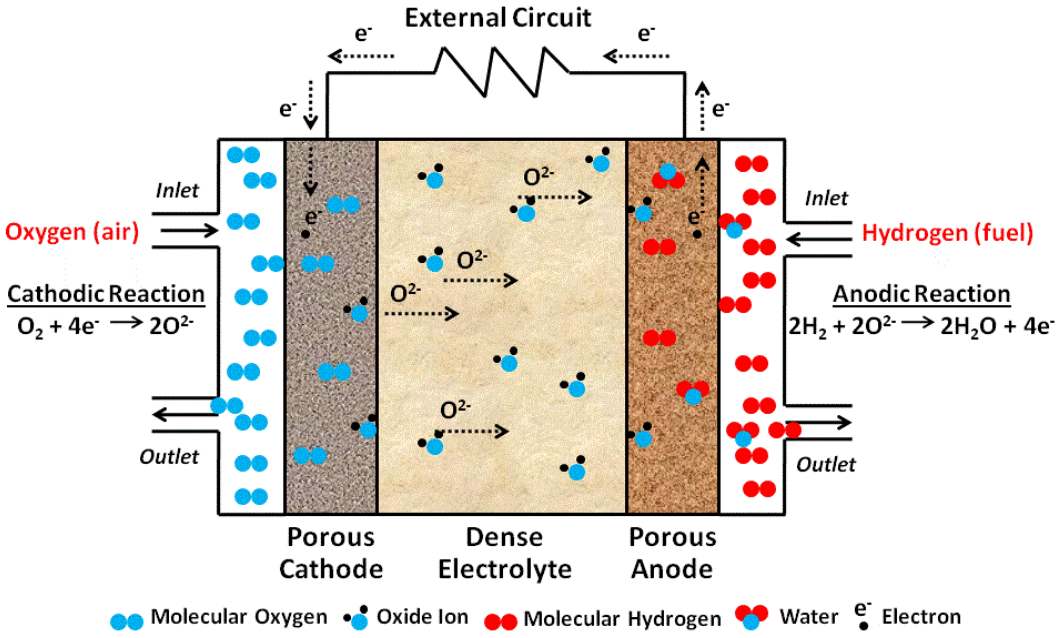

Figure 1. 1 Schematic illustration of the operation in typical SOFCs.

1.2.2 Material Selection for SOFCs

Since normal solid oxide fuel cells are operated at elevated temperature, this operating condition has featured a unique advantage over other types of fuel cells and that is fuel flexibility. On the other hand, it also imposes some limitations upon SOFCs including the durability of the material suitable to meet the SOFC operating requirements. Therefore, material selection becomes a crucial factor that influences the fuel cell performance and it requires an understanding of the basic principle of SOFCs.

1.2.2.1 Electrolyte [12-23]

Electrolyte also plays an important role that dictates the performance of solid oxide fuel cells. In SOFCs, the electrolyte is basically a dense metal – oxide ceramic that solely conducts oxide ions and prevents the migration of electrons from the anode to the cathode. In order to achieve the high performance, several requirements for the material selection are needed and they include high oxide ion conduction (high ionic conductivity), negligible electronic conduction, high density to prevent gas crossover, stability over a wide range of temperature and oxygen partial pressure, chemical compatibility with electrode materials to avoid the formation of unwanted interfacial phases, and thermal compatibility with the electrodes which is represented by comparable thermal expansion coefficients (TEC).

In typical SOFCs, yttria – stabilised zirconia (YSZ), gadolinium – or samarium – doped ceria (GDC or SDC respectively), and strontium – and magnesium – doped lanthanum gallate (LSGM) are three electrolytes that have been widely used due to different advantages and disadvantages. For instance, YSZ has been employed as a conventional electrolyte for high – temperature solid oxide fuel cells on account of high ionic conductivity at elevated temperature. Moreover, the fabrication process of YSZ electrolyte is now commercialised on the industrial scale and the raw materials necessary for YSZ preparation is naturally abundant. In case of the ceria – based electrolytes, they show superior ionic conductivity at lower temperature in comparison with that of the YSZ. However, Ce^{4+} ions in the electrolyte are inclined to the reduction reaction under reducing conditions, which results in the formation of Ce^{3+} ions. The presence of both Ce^{4+} and Ce^{3+} ions induces the electron transfer within the electrolyte and therefore decreases the fuel cell performance. For the perovskite – based electrolyte, LSGM exhibits higher ionic conductivity than those of YSZ and SDC at intermediate temperatures. Despite the costly starting materials of La_2O_3, $SrCO_3$, and Ga_2O_3, the LSGM electrolyte is less susceptible to react with other lanthanum – containing oxide cathodes and becomes the most appropriate candidate for intermediate – temperature solid oxide fuel cells (IT – SOFCs).

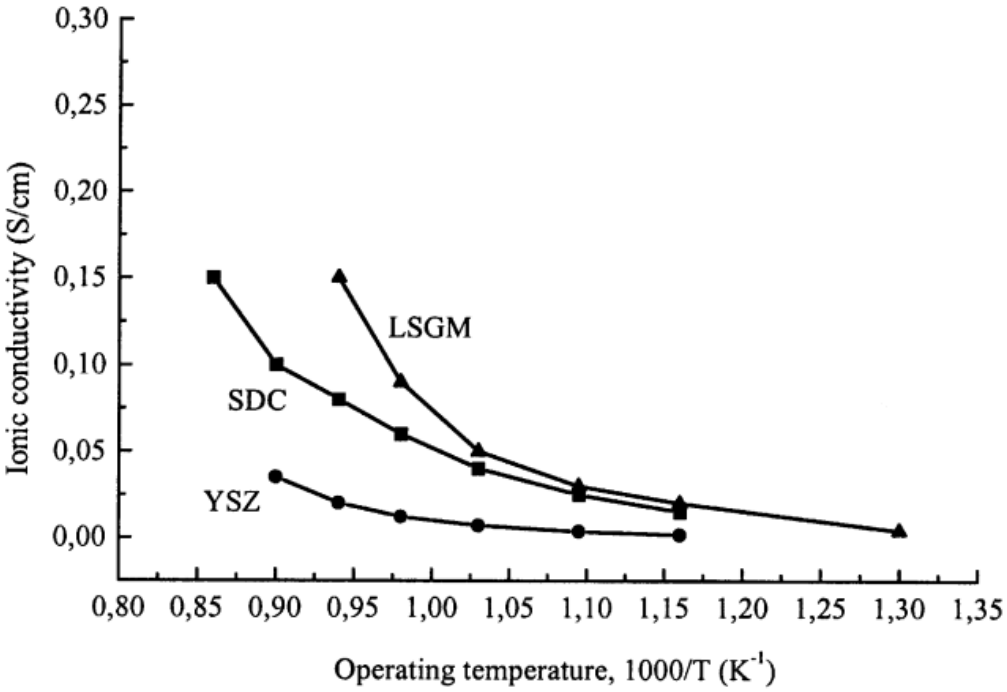

Figure 1. 2 Ionic conductivity against 1000/T for the electrolytes previously mentioned (YSZ, SDC, LSGM) [4]

Another variable that must be taken into account apart from the high ionic conductivity is thermal expansion coefficient (TEC). The mismatch of the TEC values between electrolyte and electrodes would probably cause the delamination of the single cell and it could lead to the drastic decrease in the fuel cell performance. Consequently, the TEC values of the electrolyte and the electrodes should be comparable and they are shown in Table 1.2.

Table 1. 2 Thermal expansion coefficients of some electrolytes.

Electrolyte	Thermal Expansion Coefficient (K^{-1})	[ref]
YSZ	10.8×10^{-6}	[24]
SDC	13.5×10^{-6}	[25]
LSGM	11.7×10^{-6}	[26]

1.2.2.2 Anode [27-31]

At the anode side, the electrocatalytic oxidation of fuels such as hydrogen and hydrocarbons takes place and generates the highly reducing atmosphere. Therefore, any materials that are chosen must be able to withstand such a low – oxygen partial pressure environment and maintain high electrical conductivity to attain the high cell

performance. Furthermore, the desirable anode should have both chemical and thermal compatibility with adjacent cell compartments, exhibit high tolerance to carbon coking and sulfur poisoning when hydrocarbon fuels are used, and contain sufficient porosity to facilitate the flow of gaseous reactants and products. One of the most commonly used anodes in SOFCs is Ni – based materials because they demonstrate excellent electrocatalytic activity towards hydrogen oxidation and hydrocarbon steam reforming. Nevertheless, the Ni – based anodes also show some disadvantages that prevent them from being the promising anodes such as carbon coking and sulfur poisoning. These problems then give rise to the development of new anode materials by alloying nickel with other metals including Co, Cu, and Fe to suppress the poisoning effect. The combination of nickel and alloying metals improves the tolerability of the Ni – based anodes but reduces the fuel cell performance and efficiency. As a result, new types of the anode material have been further developed to overcome the aforementioned problems and at the same time provide the adequate electrical conductivity in the reducing atmosphere. For example, CeO_2 – $LaFeO_3$ composite anode, chromium – based electrolytes such as $La_{0.8}Sr_{0.2}CrO_3$ perovskite, and Cu –GDC cermet.

1.2.2.3 Cathode [32-36]

In fuel cells, cathode is an electrode where the electrochemical oxygen reduction reaction (ORR) occurs and the corresponding reaction mechanism can be roughly described by the following steps:

i) Adsorption of the molecular oxygen onto the cathode surface

ii) Dissociation of the adsorbed molecular oxygen into oxygen atoms and the subsequent reduction to form oxide ions

iii) Diffusion of oxide ions in the bulk of the cathode

iv) Transfer of oxide ion from the cathode into the electrolyte

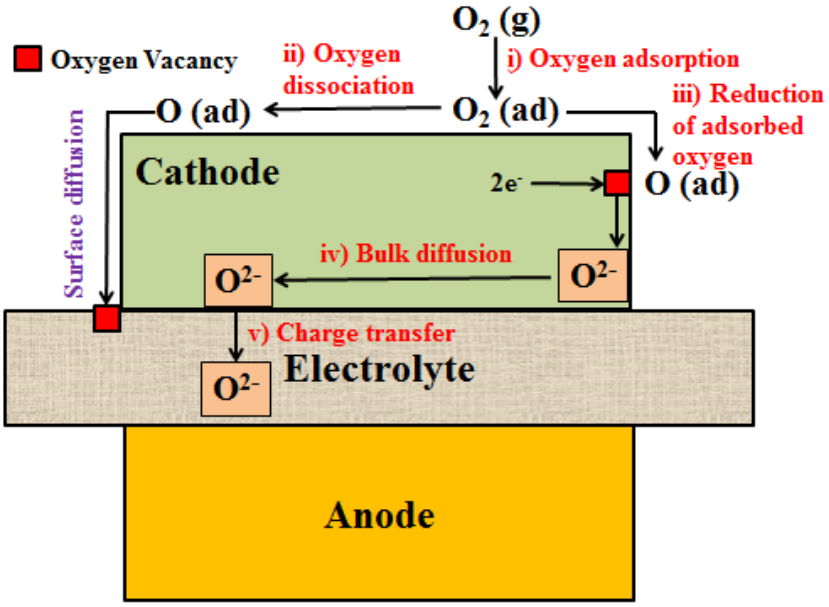

Figure 1. 3 Overall steps in the electrochemical oxygen reduction reaction.

Compared to the oxidation reaction at the anode, the rate of the oxygen reduction reaction is much slower and it becomes the rate – determining step that contributes to the polarisation resistance of the fuel cell. Therefore, in order to minimise the overall resistance, careful material selection for a promising cathode is essential to meet the following requirements:

1) Exceptional electronic and ionic conductivities
2) Good chemical compatibility with other adjacent components
3) Similar thermal expansion coefficient to other components
4) Sufficient porosity to accommodate molecular oxygen diffusion
5) Chemical and microstructural stability under oxidising conditions

Several types of cathode materials have been developed over decades. They cover simple perovskites, double perovskites, Ruddlesden – Popper phases, and perovskite – based layered structures. One of the most extensively used cathodes is the lanthanum strontium manganite family ($La_{1-x}Sr_xMnO_3$, LSM) because it shows excellent electrical conductivity and good thermal compatibility with the YSZ electrolyte at elevated temperature (800 – 1000^{o}C). In addition to the structural classification of cathode materials, the cathodes can also be regarded as composite electrodes and mixed ionic – electronic conducting (MIEC) oxides. The composite cathode comprises the electronically – conducting and the ionically – conducting phases. The oxygen reduction reaction is restricted to take place only at a region called triple phase boundary where the gaseous phase of reactants, the electronic conductor,

and the ionic conductor meet. This limitation results in the high resistance of the whole cell and the poor cell performance. On the contrary, in MIEC cathode, the electrode is capable of conducting both electrons and oxide ions simultaneously and it leads to the significant enlargement of the triple phase boundary. As a result, the resistance of the cell is greatly reduced and the cell performance is much improved. The benefit of the employment of MIEC cathodes has greatly drawn attention to the development of cathode materials for SOFCs.

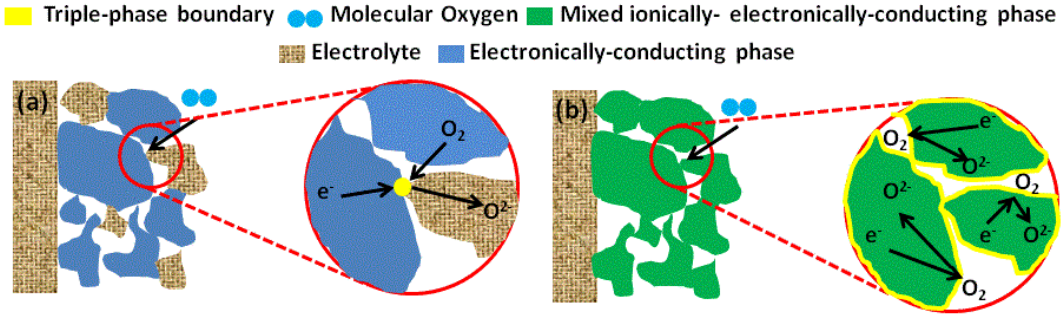

Figure 1. 4 Differences between the composite cathode and the MIEC cathode.

1.3 Electrical Conduction in SOFC Cathodes

Generally, the total electrical conductivity is normally comprised of two major components, which are electronic and ionic conductivities, and it can be calculated using the equation 1.1:

$$\sigma = \sigma_i + \sigma_{el} = n_i q \mu_i + n_{el} q \mu_{el} \qquad (1.1)$$

where n_i is the concentration of the ionic charge carriers (cm^{-3})

n_{el} are the concentration of the electronic charge carriers (cm^{-3})

q is the charge (C)

μ_i is the mobility of the ionic charge carriers ($cm^2\ s^{-1}\ V^{-1}$)

μ_{el} is the mobility of the ionic charge carriers ($cm^2\ s^{-1}\ V^{-1}$)

σ is the total electrical conductivity ($S\ cm^{-1}$)

σ_i is the ionic conductivity ($S\ cm^{-1}$)

σ_{el} is the electronic conductivity ($S\ cm^{-1}$)

These two types of conductivities also give rise to two types of electrical conduction, ionic and electronic conductions. In the electronic conduction, the charge is carried by either electrons or holes along B – O – B chains, where B and O represent transition metal ions and oxide ions respectively. The electron transfer along those chains is facilitated by the overlapping between *p* orbitals of the oxide ions and *d* orbitals of the transition metal ions but it is hindered when the angle between the B – O – B chains deviates from 180^{o}. Consequently, the electronic conduction is found to be dominant in perovskite – based oxide cathodes due to the proper overlapping angle between those octahedral units.

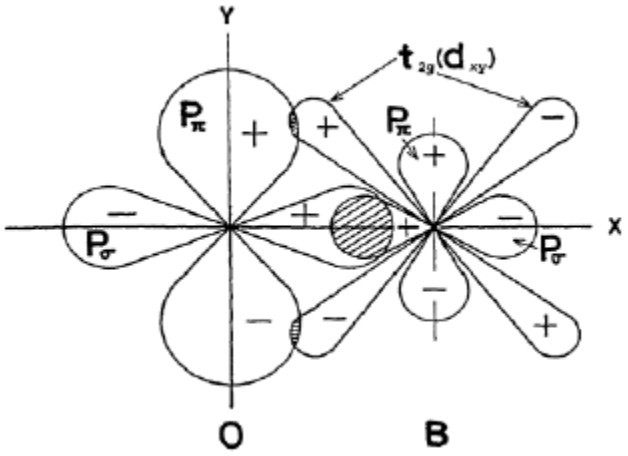

Figure 1. 5 Schematic diagram of the covalent bond between p orbitals of oxide ions and d orbitals of transition metal ions [37].

For ionic conduction, oxide ion migrations through oxygen vacancies and interstitials are two prevailing pathways that are commonly found in cathode materials. Regardless of the mechanism, the oxide ion must migrate to the most energetically unfavourable point at which the electrostatic repulsion has been substantially exerted on that oxide ion. This point is also called the saddle point and it creates an energetic barrier that prevents the oxide ion from migrating from one site to another. As a result, the migrating oxide ion requires an adequate energy to overcome the repulsion. In general, however, the ionic conductivity is comparatively lower than the electronic conduction.

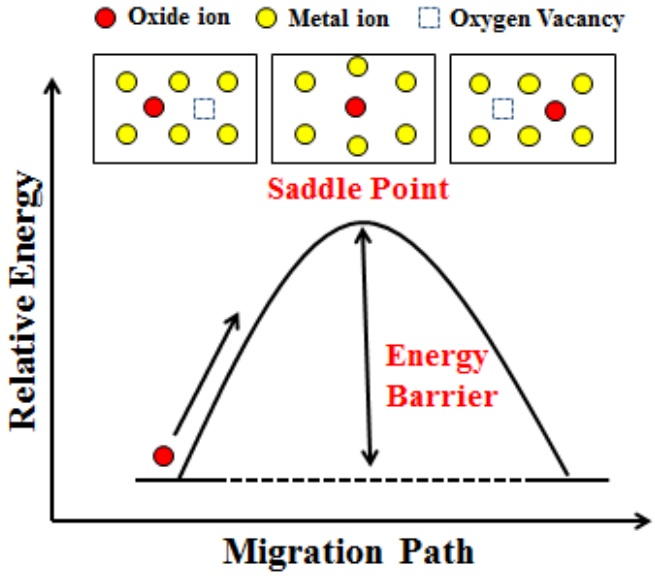

Figure 1. 6 Schematic illustrations of oxide ion migration via vacancy mechanism [38].

1.4 Layered Perovskite Related Strontium Ferrite ($Sr_4Fe_6O_{13}$) [39-47]

1.4.1 Crystal Structure

$Sr_4Fe_6O_{13}$ is a layered perovskite-related oxide which has recently gained much attention due to the practical industrial applications in oxygen – separating membrane and partial oxidation of methane. In term of crystallographic data, it adopts the orthorhombic crystal structure with the space group of *Iba2*. Moreover, it could be implied that $Sr_4Fe_6O_{13}$ is an intergrowth structure of the typical perovskite by which its structure features the intercalation of perovskite – like FeO_6 octahedral layers alternated with Fe_4O_5 polyhedral layers of tetrahedral and trigonal bipyramidal coordinations. Both of the coordination polyhedra are distorted to some extent. Additionally, $Sr_4Fe_6O_{13}$ have been perceived as an incommensurately – modulated structure, a property of a crystal possessing the average long – range structural periodicity but lacking translational periodicity in one or more of their lattice directions.

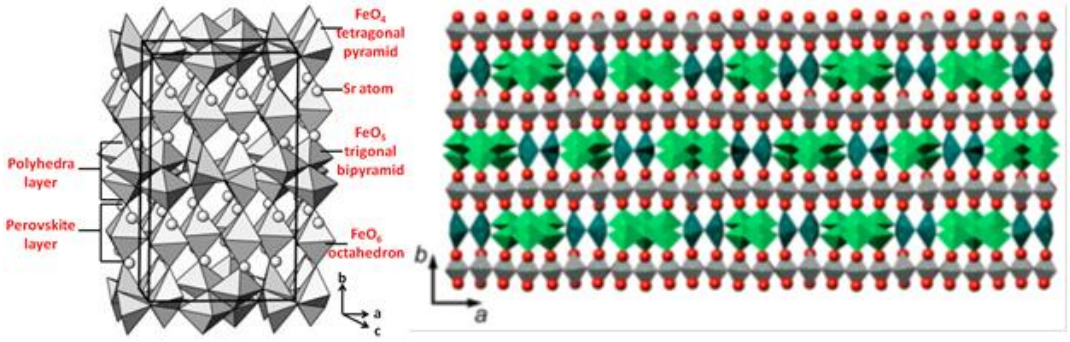

Figure 1. 7 Three-dimensional view of the crystal structure of $Sr_4Fe_6O_{13}$ (left) and the view along [001] plane showing the incommensurate modulation of the structure (right).

1.4.2 Electrical Conductivity

Like other cathode materials for SOFCs, $Sr_4Fe_6O_{13}$ demonstrates both electronic and ionic conduction behaviours. Under oxidising conditions, it acts as a *p* – type semiconductor using holes as an electronic charge carrier and oxygen interstitials as an ionic charge carrier. The holes are energetically favourable to be associated with the perovskite slabs while the oxygen interstitials are likely to reside in the polyhedral slabs. On the other hand, it acts as an *n* – type semiconductor by generating electrons in the polyhedral layers but oxygen vacancies in the perovskite layers in reducing environments. In relation to that, the deviation from the ideal overlapping angle between the *p* orbitals of the oxide ions and the *d* orbitals of the transition metal ions (180^o) enhances the energetic barrier for the charge transfer across the different layers. As a result, the electronic conduction has become anisotropic and the overall electrical conductivity is perceived as anisotropy.

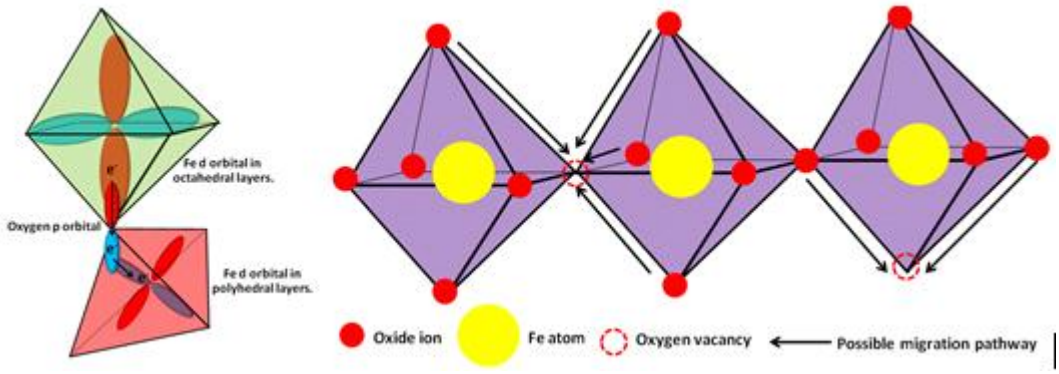

Figure 1. 8 Graphical illustration of the electronic conduction and the ionic conduction via oxygen vacancy.

1.5 Electrochemical Impedance Spectroscopy (EIS) [48-52]

Electrochemical impedance spectroscopy is a powerful technique which provides the information to identify polarisation resistances of the individual processes. The basic principle of the technique lies on the fact that each electrochemical process possesses different time constant and it responds to the electrical signal of different frequency. This is the advantage that makes the direct – current measurement impractical. However, the interpretation of results and the deconvolution of spectra require much knowledge in the system of interest and it is definitely time – consuming.

Typically, the EIS experiment begins with the application of the small sinusoidal perturbation to the system over a wide range of frequency and the sinusoidal response is finally recorded. The perturbation is done either on the voltage or the current applied. After the measurement is finished, the impedance (Z) is calculated and expressed as the following equation which is based on Ohm's Law:

$$Z = \frac{V(\omega)}{I(\omega)} = \frac{Vcos(\omega t)}{Icost(\omega t - \varphi)} = Z_0(cos\varphi + jsin\varphi) = Z_{re} + jZ_{im} \quad (1.2)$$

where

j	is the imaginary number
V	is the amplitude of the applied voltage (V)
I	is the amplitude of the current response (A)
φ	is the phase shift of the response compared to the applied signal
ω	is the applied frequency (Hz)
Z	is the total impedance response (Ω)
Z_{re}	is the real part of the total impedance (Ω)
Z_{im}	is the imaginary part of the total impedance (Ω)

The illustration between Z_{re} on the X – axis and - Z_{im} on the Y – axis is called the Nyquist plot. In addition, the Nyquist plot can also be described by equivalent circuit model (ECM) which corresponds to the electrochemical processes that really occur in SOFC system. The examples of the common electrical circuit components include resistors (R), capacitors (C), constant – phase elements (CPE), and inductors (L) and they specifically represent individual processes in the fuel cell.

จุฬาลงกรณ์มหาวิทยาลัย
Chulalongkorn University

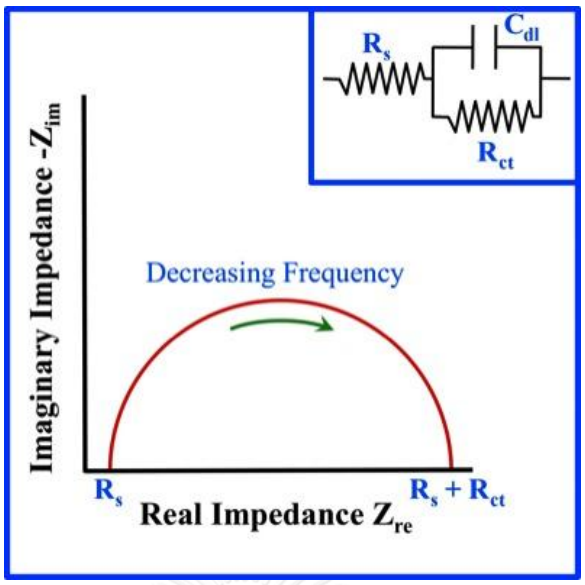

Figure 1. 9 Example of the Nyquist plot for the EIS measurement.

1.6 Literature Review

Nevertheless, both ionic and electronic conductivities of $Sr_4Fe_6O_{13}$ are considered extremely low compared to other ceramic materials such as $LaFeO_{3-\delta}$ and $SrCoO_{3-\delta}$. Therefore, the potential applications in high – temperature electrochemical devices seem to be problematic. Further structural modifications are essentially required to improve the electrical conductivity as well as oxygen diffusion. In general, the incorporation of aliovalent foreign atoms and the corresponding compositional variations have been extensively exploited by materials scientists since they possibly induce the formation of extrinsic defects in the original structure by means of charge compensation. Moreover, on account of the structural similarity between $Sr_2Fe_2O_5$ and $Sr_4Fe_6O_{13}$, any effects found in the incorporation of aliovalent atoms into $Sr_2Fe_2O_{5+\delta}$ or other brownmillerite structures improving their electrical conductivities and others should have the same effect on $Sr_4Fe_6O_{13}$ theoretically. As a result, these radical notions have been used as criteria for the selection of literature as follows.

Chen [53] et al. investigated the potential application of $LnBaFe_2O_{5+\delta}$ (Ln = La, Pr, Nd, Sm, Gd and Y; LnBF) as cathodes for intermediate – temperature solid oxide fuel cells (IT-SOFCs). It was found that the samples with Ln = La and Pr exhibited the single phase and adopted the orthorhombic perovskite structure whereas the samples with Ln = Nd and Sm were identified as cation – ordered layered structures. Impurity phases coexisted in GBF and YBF samples. All LnBF samples exhibited *p* –type semiconducting behaviours and their electronic conductivities increased with the increasing temperature and the decrease in the size of Ln^{3+} ions. In case of the electrochemical performance, the SBF electrode demonstrated the best electrocatalytic activity for ORR though.

Jin [54] et al. evaluated the performance of $LnBaCoFeO_{5+\delta}$ (Ln = Pr and Nd; PBCF and NBCF) as cathodes for IT-SOFCs. It was found that no impurities were observed in PBCF and NBCF and they showed relatively good chemical compatibility with LSGM electrolyte. For the electrical conductivity, PBCF displayed virtually two times higher than NBCF and both of them were semiconductors. In term of the electrochemical performance, PBCF illustrated high electrocatalytic activity for ORR.

Bredesen [55] et al. successfully synthesised the MIEC conductor $Sr_{3.6}La_{0.4}Fe_6O_{13}$ and it was found to be the multiphase mixture of the $Sr_{1-y}La_yFe_{12}O_{19}$ inclusions, $(Sr_{0.85}La_{1.5})FeO_3$ tetragonal perovskite, and a plate – like nano – scale intergrowth of $(Sr_{1-x}La_x)FeO_3$ and $Sr_4Fe_6O_{13}$ phases. In addition, the observations revealed the low solubility of La in the $Sr_4Fe_6O_{13}$ phase and increasing La concentration promoted the formation of the perovskite phase.

Manthiram [46] et al. investigated the crystal chemistry and the electrical property of $Sr_{4-x}Ca_xFe_{6-y}Co_yO_{13}$ which were synthesised by the conventional solid – state reaction. The results demonstrated the transition in electrical conduction behaviour from metallic to semiconducting mechanism in calcium – doped oxides. Furthermore, the transition behaviour was also affected by the presence of other transition metal such as Mn, Co, Ni and Cu.

Chen [41] et al. studied the effect of Co addition in $SrFe_{1.5}O_y$ on the phase composition, oxidation state, and electrical conductivity. It was revealed that the phase composition and the stability of $SrFe_{1.5-x}Co_xO_y$ were strongly dependent on the cobalt content. In addition, upon increasing the concentration of cobalt dopant, the valence number of transition metals did not change much within the single phase region while it varied significantly in the multiphase region. However, the total electrical conductivity still increased with increasing cobalt content.

Norby [56] et al. emphasised the impact of cobalt addition in the layered $Sr_4Fe_6O_{13}$ phase on its stability and the agglomeration of the oxygen vacancies and Co^{2+}. It was also suggested that the formation of the defect associates strongly influenced the electrical conductivity of the mixed $SrFe_{1.5-x}Co_xO_z$.

Shao [57] et al investigated the effect of calcination temperature and phase composition on the cell performance. The single cell was fabricated using SDC and YSZ as the double electrolyte, Ni – YSZ as the composite anode, and $Sr_4Fe_4Co_2O_{13}$ as the cathode. The results showed that the $Sr_4Fe_4Co_2O_{13}$ cathode sintered at 1050^{o}C contained 61 wt% of the perovskite phase and the corresponding single cell exhibited the highest maximum power density around 1465 mW cm^{-2} at 750^{o}C. The author also stated that the observations were due to the synergistic effect of the presence of both the perovskite and the layered phases.

According to the literature, the substitution of La, Pr, Sm into Sr sites and of Co and Ni into Fe sites is proposed for improving the electrical conductivity as well as the electrocatalytic activity for the oxygen reduction reaction and the lanthanide – and

transition metal – doped oxide cathodes would be a novel promising cathodes for intermediate – temperature solid oxide fuel cells.

1.7 Objectives

1.7.1 To synthesise the layered $Sr_4Fe_6O_{13}$ materials with the compositions shown below.

1.8.1.1 Substitution of Sr site with La, Pr, and Sm

- $Ln_xSr_{4-x}Fe_6O_{13}$ (Ln = La, Pr, Sm, x = 0.0 – 0.4)

1.8.1.1 Substitution of Fe site with Co and Ni

- $Sr_4Fe_{6-y}M_yO_{13}$ (M = Co, Ni, x = 0.0 – 1.7)

1.7.2 To determine the crystal structure of the synthesised oxides.

1.7.3 To measure the electrical conductivity of the oxide samples.

1.7.4 To evaluate the electrochemical property of the prepared oxides.

1.7.5 To calculate the oxygen non – stoichiometry of the synthesised oxides.

จุฬาลงกรณ์มหาวิทยาลัย
Chulalongkorn University

CHAPTER II
EXPERIMENTAL PROCUDURE

The chemicals, apparatuses and experimental descriptions including material preparation and characterisation are explained below.

2.1 Chemicals

The chemicals and reagents which were used without further purification are listed in Table 2.1.

Table 2. 1 Chemicals and reagents used in this research

Chemicals and Reagents	Formula Weight (g/mol)	Purity (%)	Company
$SrCO_3$	147.63	≥99.9	Aldrich
Fe_2O_3	159.69	81	Labchem
Co_3O_4	240.80	99.5	Aldrich
NiO	74.69	99	Aldrich
Pr_6O_{11}	1021.44	99.9	Aldrich
La_2O_3	325.81	99.99	Wako
Ga_2O_3	187.44	≥99.99	Aldrich
MgO	40.3	≥98.0	Fluka
Sm_2O_3	348.70	99.9	Aldrich

2.2 Material Preparation

2.2.1 Cathode Preparation

All cathode materials were synthesised through a conventional solid – state reaction method and their compositions and abbreviations are summarised in Table 2.2.

Table 2. 2 Cathodes composition and abbreviation.

Substituted Site	Dopant	Composition	Abbreviation
-	-	$Sr_4Fe_6O_{13}$	SFO
Strontium (Sr)	Lanthanum (La)	$La_{0.1}Sr_{3.9}Fe_6O_{13}$	LSF0.1
		$La_{0.2}Sr_{3.8}Fe_6O_{13}$	LSF0.2
		$La_{0.3}Sr_{3.7}Fe_6O_{13}$	LSF0.3
		$La_{0.4}Sr_{3.6}Fe_6O_{13}$	LSF0.4
	Praseodymium (Pr)	$Pr_{0.1}Sr_{3.9}Fe_6O_{13}$	PSF0.1
		$Pr_{0.2}Sr_{3.8}Fe_6O_{13}$	PSF0.2
		$Pr_{0.3}Sr_{3.7}Fe_6O_{13}$	PSF0.3
		$Pr_{0.4}Sr_{3.6}Fe_6O_{13}$	PSF0.4
	Samarium (Sm)	$Sm_{0.1}Sr_{3.9}Fe_6O_{13}$	SSF0.1
		$Sm_{0.2}Sr_{3.8}Fe_6O_{13}$	SSF0.2
		$Sm_{0.3}Sr_{3.7}Fe_6O_{13}$	SSF0.3
		$Sm_{0.4}Sr_{3.6}Fe_6O_{13}$	SSF0.4
Iron (Fe)	Cobalt (Co)	$Sr_4Fe_{5.9}Co_{0.1}O_{13}$	SFCo0.1
		$Sr_4Fe_{5.7}Co_{0.3}O_{13}$	SFCo0.3
		$Sr_4Fe_{5.5}Co_{0.5}O_{13}$	SFCo0.5
		$Sr_4Fe_{5.3}Co_{0.7}O_{13}$	SFCo0.7
		$Sr_4Fe_{5.1}Co_{0.9}O_{13}$	SFCo0.9
		$Sr_4Fe_{4.9}Co_{1.1}O_{13}$	SFCo1.1
		$Sr_4Fe_{4.7}Co_{1.3}O_{13}$	SFCo1.3
		$Sr_4Fe_{4.5}Co_{1.5}O_{13}$	SFCo1.5
		$Sr_4Fe_{4.3}Co_{1.7}O_{13}$	SFCo1.7

จุฬาลงกรณ์มหาวิทยาลัย
CHULALONGKORN UNIVERSITY

Table 2. 3 Cathodes composition and abbreviation (cont'd).

Substituted Site	Dopant	Composition	Abbreviation
	Nickel (Ni)	$Sr_4Fe_{5.9}Ni_{0.1}O_{13}$	SFNi0.1
		$Sr_4Fe_{5.7}Ni_{0.3}O_{13}$	SFNi0.3
		$Sr_4Fe_{5.5}Ni_{0.5}O_{13}$	SFNi0.5
		$Sr_4Fe_{5.3}Ni_{0.7}O_{13}$	SFNi0.7
		$Sr_4Fe_{5.1}Ni_{0.9}O_{13}$	SFNi0.9
		$Sr_4Fe_{4.9}Ni_{1.1}O_{13}$	SFNi1.1

The stoichiometric amounts of $SrCO_3$, Fe_2O_3, La_2O_3, Pr_6O_{11}, Sm_2O_3, Co_3O_4, and NiO were thoroughly mixed and ground for an hour and then calcined in air at 850^{o}C for 16 hours. After that, the calcined powders were grounded for another hour and subsequently sintered in air at 1185^{o}C for 5 hours to obtain the cathode powders.

2.2.2 Electrolyte Preparation [58]

Because of the high ionic conductivity in the intermediate – temperature range, the Sr – and Mg – doped lanthanum gallate with the composition of $La_{0.9}Sr_{0.1}Ga_{0.8}Mg_{0.2}O_3$ (LSGM) was employed as an electrolyte and it was prepared via the solid – state reaction method. The stoichiometric mixture of La_2O_3, Ga_2O_3, $SrCO_3$, and MgO was homogenously ground for one hour and then calcined in air at 1000^{o}C for 6 hours. Next, the calcined powder was re – ground for an hour and then pelletised into cylindrical discs with the diameter of 2 cm using a cold isostatic pressing (CIP) method. The pressure and the pressurization time applied for the pelletisation were 325 MPa and 30 minutes respectively. Finally, the resulting discs were sintered in air at 1500^{o}C for 5 hours and the sintered discs were made thin down to 0.3 mm in thickness by a diamond grinding machine.

2.3 Material Characterisation

2.3.1 X – ray Diffractometry (XRD)

The structural identification of prepared materials was performed using a Rigaku, DMAX 2002 Ultima Plus X – Ray powder diffractometer equipped with a monochromator and a Cu – target X – ray tube (40 kV, 30 mA). The diffraction angles (2Θ) varied from 20 to 70 degrees (scan speed of 5 degrees min^{-1}) were recorded at Department of Chemistry, Faculty of Science, Chulalongkorn University.

2.3.2 X – ray Photoelectron Spectroscopy (XPS)

Surface chemical properties of the rectangular (12 mm x 5 mm x 2 mm) oxide samples were evaluated by a Kratos Axis Ultra X – ray photoelectron spectrometer using a monochromatic Al Kα (1486.6 eV) as an X – ray source and a pass energy of 40 eV at The Petroleum and Petrochemical College, Chulalongkorn University. The analysis chamber was pressurised and manipulated around 10^{-7} – 10^{-9} Torr during the measurement. The binding energy of each species was recorded and calibrated with respect to that of the C1s reference peak at 284.6 eV.

2.3.3 Electrical Conductivity Measurement [59]

The electrical conductivity of the oxide materials was characterised via the DC four – point probe method. The sintered discs of oxide cathodes were cut into rectangular bars with the approximate dimension of 12 mm x 5 mm x 1.5 mm. Four platinum wires were used as electrodes: the outer two wires corresponded to the current – applying probes and the inner two ones represented the voltage – detecting probes as shown in Figure 2.1. These wires were attached to the specimen with platinum paste as a binder and heated at 950°C for 10 minutes to ensure a good electrical contact with the samples. When the direct current was applied through the current probes over the temperature range of 300°C to 800°C, the voltage difference between the inner probes was measured by the Autolab PGSTAT302N potentiostat/galvanostat and it was converted to the electrical conductivity using the equation 2.1:

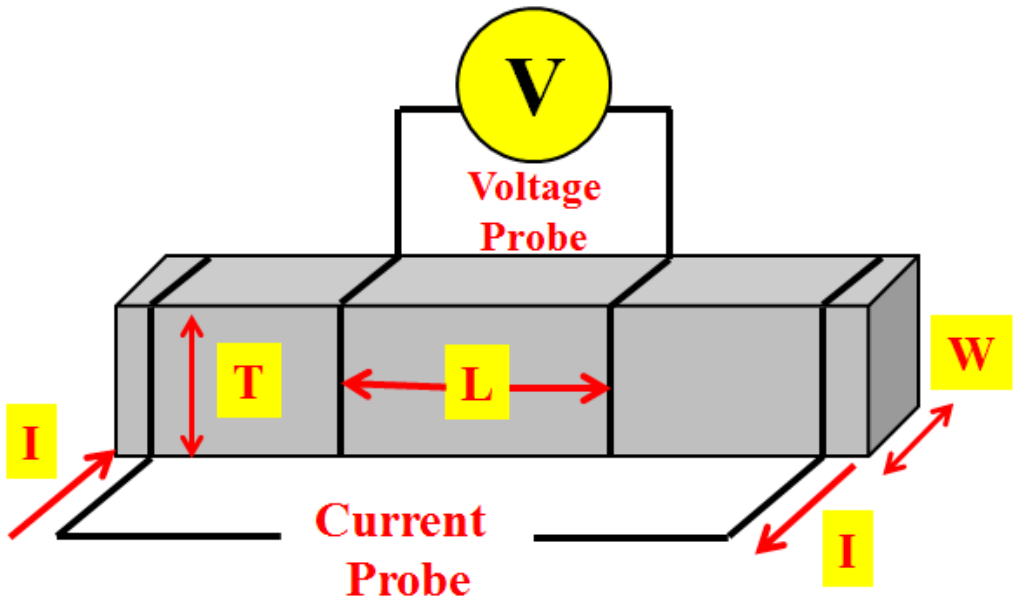

Figure 2. 1 Schematic illustration of the DC four – point probe experiment.

$$\sigma = \frac{I \times L}{V \times W \times T} \quad (2.1)$$

where σ is the electrical conductivity (S cm^{-1})

I is the applied DC current (A)

L is the distance between the two inner probes (cm)

V is the voltage difference between the two outer probes (V)

W is the width of the specimen (cm)

T is the thickness of the specimen (cm)

2.3.4 Electrochemical Impedance Spectroscopy (EIS)

Symmetric cells were fabricated using 300 – μm thick LSGM as the electrolyte and the cathode oxides as the electrodes to investigate the electrochemical property of the materials. The prepared cathode oxides were made into slurries using a mixture of ethyl cellulose and isobutyrate as a binder. The cathode slurry was then applied onto both sides of the electrolyte disc through screen printing technique and subsequently fired in air at 900ºC for 30 minutes for the complete adhesion of the electrodes and the electrolyte. After that, the cell was placed in between two sets of concentric alumina tubes without sealing and the electrodes were exposed to air under ambient pressure. The overall instrumentation is demonstrated in Figure 2.2. At the operating temperatures from 600ºC to 800ºC, the AC impedance response was recorded on the potentiostat mode of Autolab PGSTAT302N instrument equipped with the frequency response analyser (FRA) under open circuit conditions in the frequency range from 1 MHz to 0.01 Hz.

จุฬาลงกรณ์มหาวิทยาลัย
Chulalongkorn University

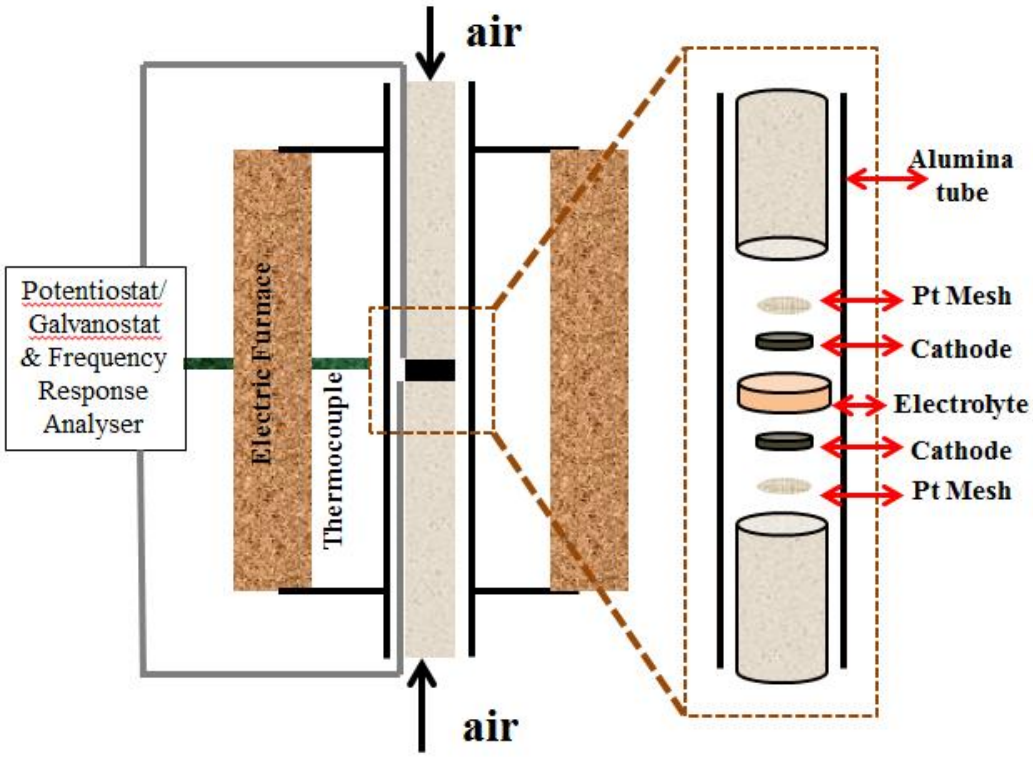

Figure 2. 2 Schematic diagram of the instrumental setup for EIS measurement.

2.3.5 Thermogravimetric Analysis (TGA)

The oxygen non – stoichiometry of prepared oxides was estimated by thermogravimetry using a NETZSCH simultaneous thermal analyser 449 F3 in the temperature range from 50ºC to 1000º. The measurement was carried out in air with the heating rate of 5ºC min^{-1}. The data was also collected at Scientific and Technological Research Equipment Centre, Chulalongkorn University.

CHAPTER III

RESULTS AND DISCUSSIONS

3.1 Structural Characterisation

3.1.1 $Ln_xSr_{4-x}Fe_6O_{13}$ (Ln = La, Pr, Sm)

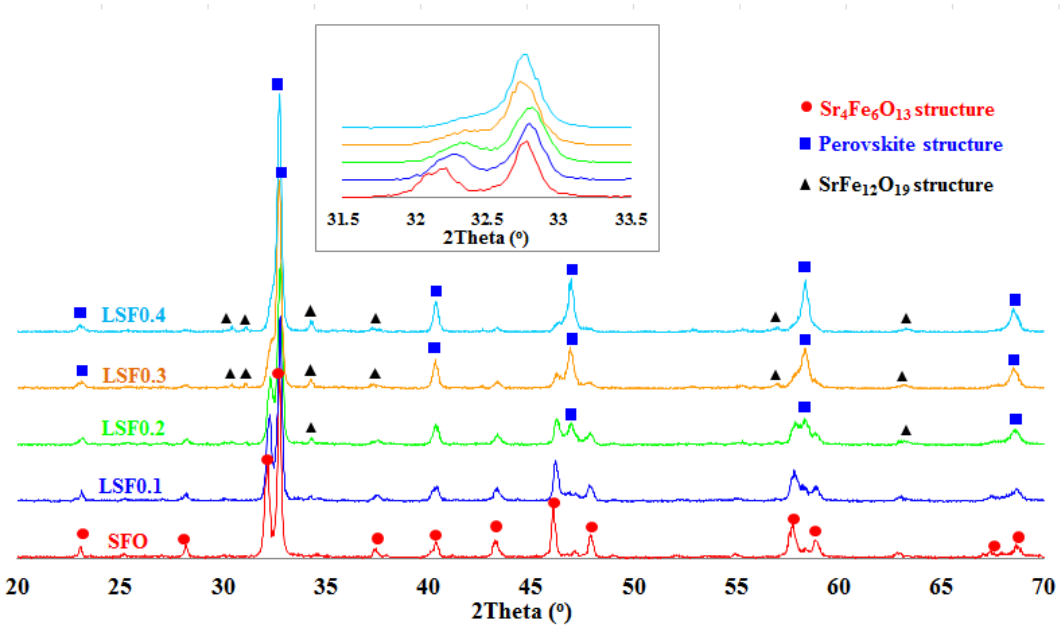

Figure 3. 1 X-ray diffractograms of LSFx oxides sintered in air at 1185°C for 5 hours.

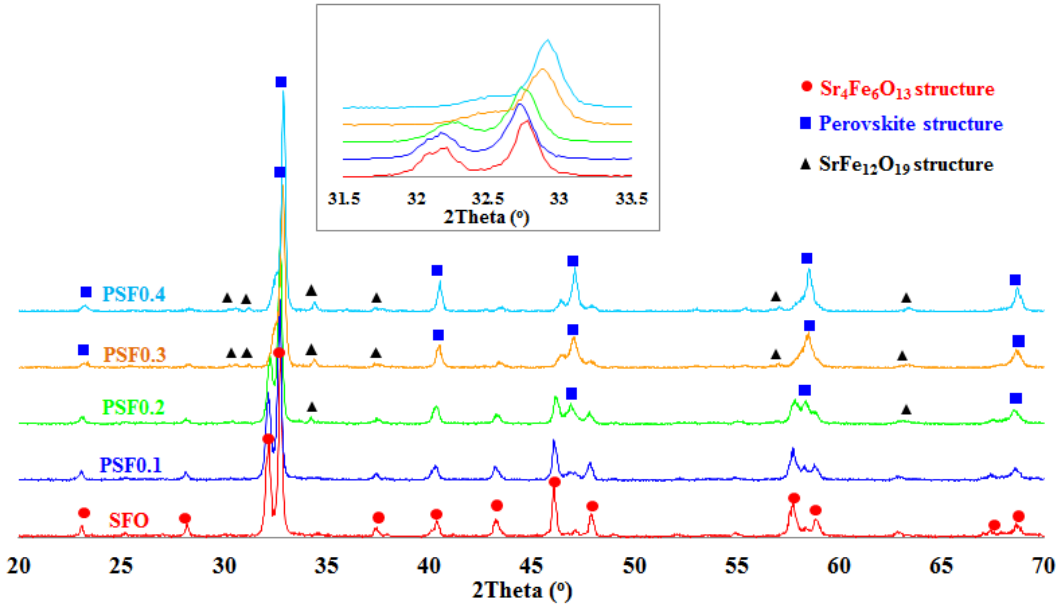

Figure 3. 2 X-ray diffractograms of PSFx oxides sintered in air at 1185°C for 5 hours.

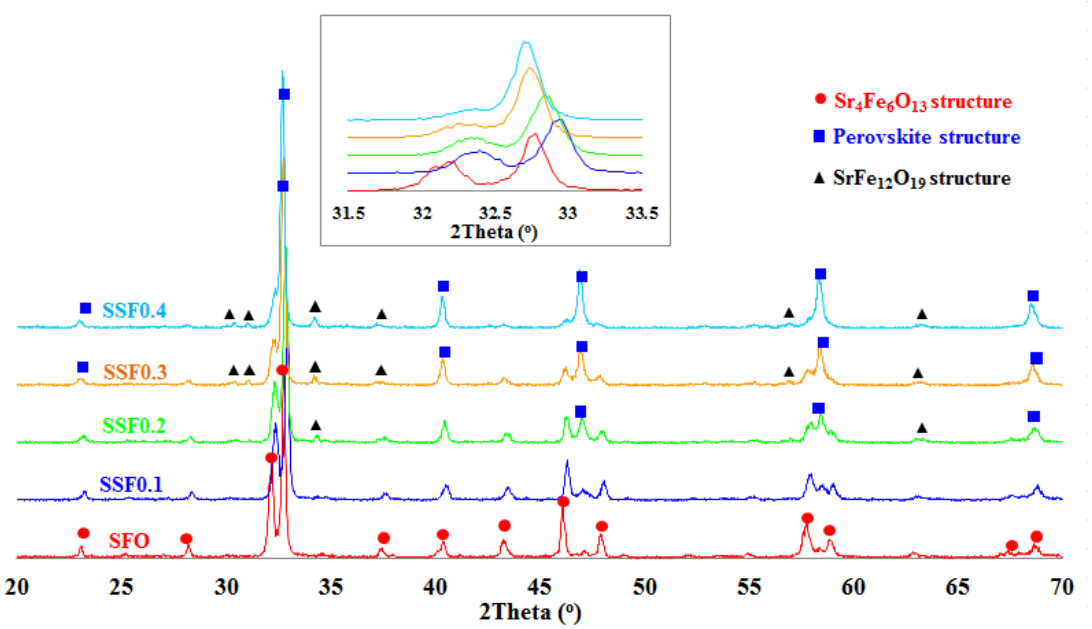

Figure 3. 3 X-ray diffractograms of SSFx oxides sintered in air at 1185°C for 5 hours.

Figures 3.1 – 3.3 demonstrate respectively the X-ray diffractograms of LSFx, PSFx, and SSFx oxides sintered in air at 1185°C for 5 hours. They obviously indicate the successful incorporation of lanthanide ions into the layered structure, $Sr_4Fe_6O_{13}$, at Sr sites up to the composition of x = 0.2, which is attributed to the similar size between substituted Sr^{2+} ions and the lanthanide dopants. In the layered structure, the Sr^{2+} ions adopt the coordination number of nine [60] and their ionic radius is 131 pm [61]. Likewise, the ionic radii of the lanthanide dopants with the 9 – fold coordination geometry also fall in the same range as that of Sr^{2+} ions (La^{3+} = 121.6 pm, Pr^{3+} = 117.9 pm, Sm^{3+} = 113.2 pm) [61]. As a result, the contraction of the structure causes a slight peak shift of the peak around 2Theta = 32.5° in all oxide series.

However, when the composition of the lanthanide dopants is greater than 0.1, the perovskite and the magnetoplumbite or *M* – type ($SrFe_{12}O_{19}$) phases begin to coexist with the layered phase. Upon raising the concentration of the dopants, the amount of the perovskite phase continues to increase whereas the *M* – type phase content remains essentially constant. The coexistence of the perovskite and the *M* – type phases can be explained by the phase equilibrium relationship reported by Fossdal et al. [43],

$$Sr_{1-x}FeO_{3-\delta}(s) + SrFe_{12}O_{19}(s) \rightarrow Sr_4Fe_6O_{13}(s) + O_2(g)\ at\ 1048\ K \quad (3.1)$$

where the oxygen non – stoichiometry for each oxide is neglected. At elevated temperatures above 775°C, the undoped layered phase is entropically – stabilised with respect to the parent perovskite and the *M* – type phases but it is still retained upon

cooling due to its intrinsic metastability. With the means of aliovalent doping, the doped layered structure is destabilised and the dopant – induced instability becomes a driving force to favour the backward reaction for structural relaxation and charge compensation. As a result, more perovskite and *M* – type phases are formed and the virtually complete transformation from the layered phase into the parent phases is observed at x = 0.4.

3.1.2 $Sr_4 M_yFe_{6-y}O_{13}$ (M = Co, Ni)

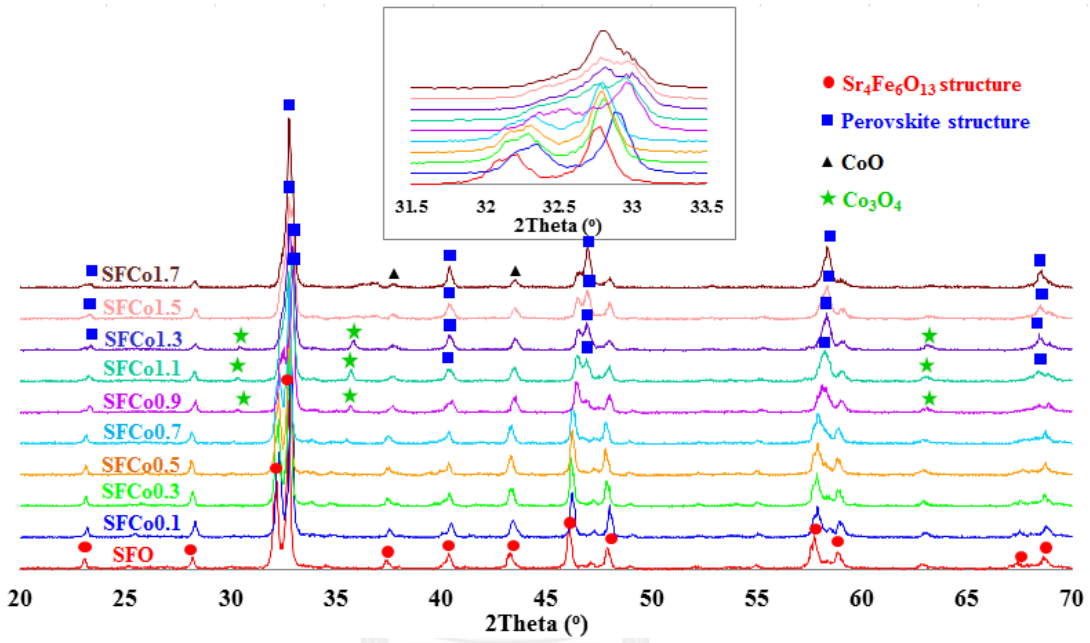

Figure 3. 4 X-ray diffractograms of SFCox oxides sintered in air at 1185°C for 5 hours.

With regard to the X – ray diffractograms of SFCox oxides sintered in air at 1185°C for 5 hours shown in Figure 3.4, they reveal that the introduction of Co^{2+} and Co^{3+} ions into the layered structure is successful up to the composition of x = 1.1, which is also clarified by the slight peak shift around 2Theta of 32.5° to higher peak positions. The incorporation of Co^{n+} ions into Fe^{3+} sites stems from the similarity in the ionic radii of the substituted ion and the dopant. In the layered structure, three possible types of environment in which Fe^{3+} ions are surrounded are found [61, 62]; one with the octahedral coordination (r = 64.5 pm) in the perovskite slab and the other two with the 4 – fold (r = 49 pm) and 5 – fold (r = 72 pm) coordination geometries in the polyhedral slab. Concerning the ionic radii of Co ion species, it is assumed that both Co^{2+} and Co^{3+}ions having the trigonal bipyramidal coordination geometry (r = 67 and 61 pm respectively) are, therefore, able to replace the Fe^{3+} ions and the computational [63] and the experimental [41, 64] investigations also confirm the site preference and the plausible oxidation state of Co ions.

Nevertheless, the spinel phase (Co_3O_4) firstly appears when the composition of the Co dopant reaches x = 0.9 but it then no longer exists when the amount of the dopant is greater than 1.3. In addition, the perovskite phase starts to coexist with the layered phase at x = 1.1 and its content gradually rises with the dopant concentration. The presence of both the perovskite and the spinel phases with the layered phase is also illustrated by the heterogeneous phase equilibrium reported by Fossdal et al [42],

$$SrFe_{1-z}Co_zO_{3-\delta}(s) + Co_{3-y}Fe_yO_4(s) \rightarrow Sr_4Fe_{6-x}Co_xO_{13}(s) + O_2(g) \quad (3.2)$$

where oxygen non – stoichiometry is omitted. The explanation which accounts for the observation in case of the lanthanide – containing layered phase can also be applied to the Co – doped layered phase as well. Furthermore, at higher Co concentration, the new phase equilibrium relationship is established due to the decreased solubility of Co in the layered phase, which explains the presence of CoO at x = 1.7,

$$Sr_4Fe_{6-x}Co_xO_{13}(s) \rightarrow Co_{1-y}Fe_yO(s) + SrFe_{1-z}Co_zO_{3-\delta}(s) + O_2(g) \quad (3.3)$$

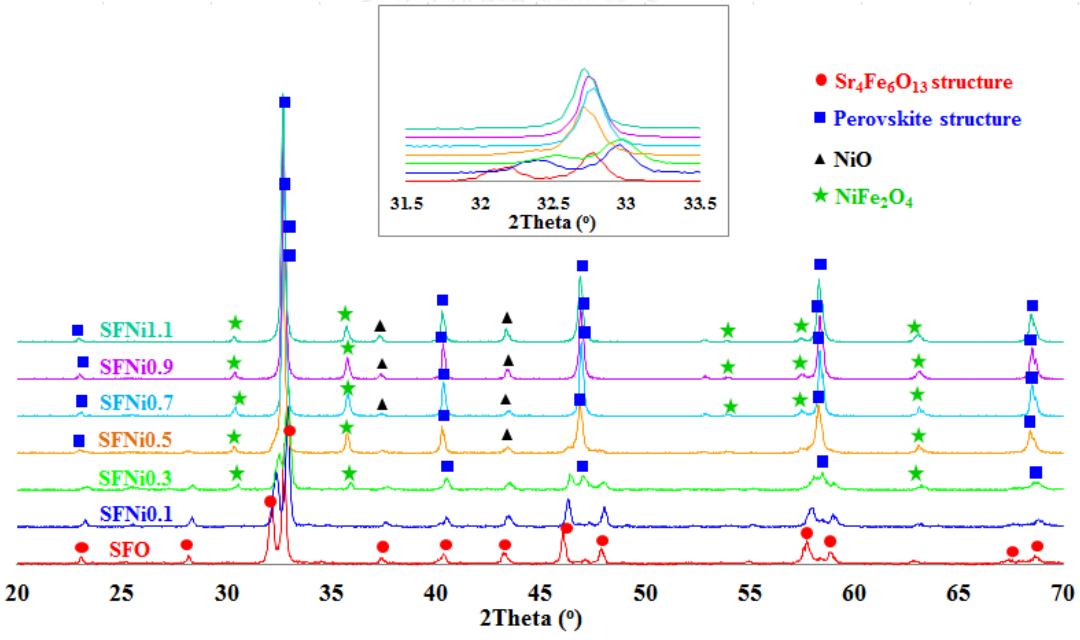

Figure 3. 5 X-ray diffractograms of SFNix oxides sintered in air at 1185°C for 5 hours.

Regarding the X – ray diffractograms of SFNix oxides sintered in air at 1185°C for 5 hours shown in Figure 3.5, they exhibit the successful incorporation of Ni^{2+} into the layered structure up to the composition of x = 0.3. Also, it is evidenced by the slight peak shift around 2Theta of 32.5° and attributed to the similar size between Ni^{2+} ions and Fe^{3+} ions. The most likeliest environment for the Ni^{2+} ions to be located is at the trigonal bipyramidal site since the ionic radius of the Ni^{2+} ions achieving the 5 – fold

coordination geometry is 63 pm [61] and the tetrahedral coordination site is energetically unfavourable for Ni^{2+} ions [65].

However, like other doped layered oxides, increasing the Ni content induces the formation of the perovskite phase, NiO, and the spinel phase ($NiFe_2O_4$). For the perovskite phase, it is firstly observed when the composition of the Ni dopant is 0.3 and its content increases rapidly and completely becomes the dominant phase at the expense of the layered phase at x = 0.7. On the contrary, the spinel and the NiO phases exist respectively at x = 0.3 and 0.5 and their concentrations are maintained relatively constant regardless of the concentration of the dopant. These observations can probably be explained by applying the heterogeneous equilibria described in the Co – doped layered phase instance [42].

3.2 Electrical Conductivity Characterisation

3.2.1 $Ln_xSr_{4-x}Fe_6O_{13}$ (Ln = La, Pr, Sm)

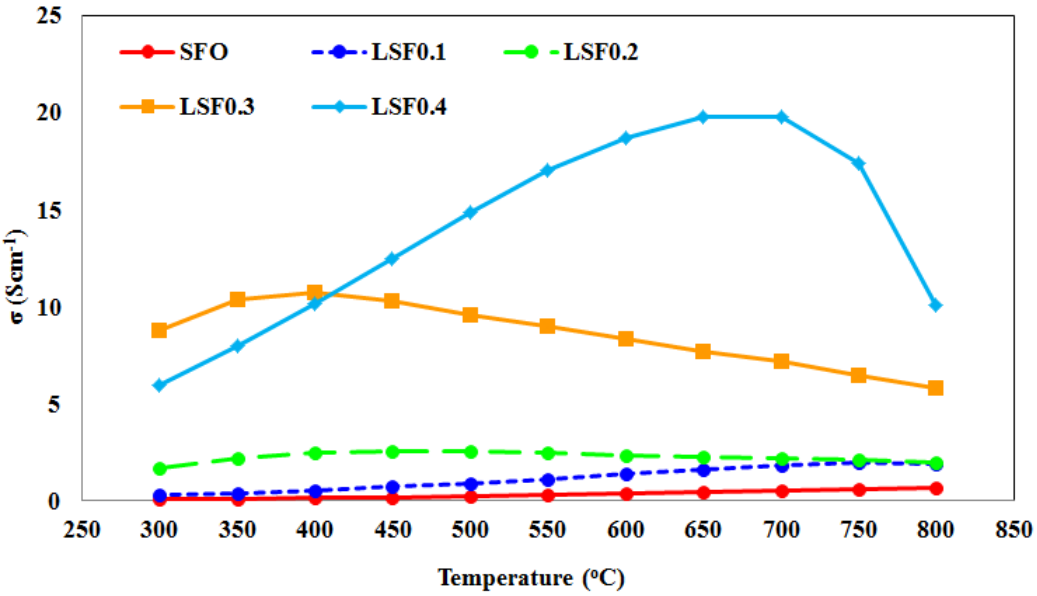

Figure 3. 6 Temperature – dependence electrical conductivity of LSFx oxides in air.

Figure 3.6 shows the temperature dependence of the total electrical conductivity of LSFx oxides in air within the temperature range from 300°C to 800°C. Apparently, it can be seen that the electrical conductivities of the undoped layered phase, SFO, and the LSF0.1 oxide increase with increasing temperature and both oxides consequently indicate the typical semiconducting behaviour. However, LSFx oxides with the composition above x = 0.1 illustrate the semiconductor with the transition at approximately 400°C – 450°C in LSF0.2 and LSF0.3 but at 650°C – 700°C in LSF0.4.

The change in the electrical conduction behaviour can be explained on the basis of charge redistribution proposed by Manthiram et al. [46]. In the undoped layered phase, the net charges in the perovskite FeO_2 and the polyhedral Fe_4O_5 slabs are supposed to be +1 and -1, respectively. This implies that the actual oxidation state of Fe could probably be higher than 3+ in the perovskite layer but lower than 3+ in the polyhedral one. When the temperature rises above 450ºC, thermal energy activates the transfer of electrons from the polyhedral layer to the perovskite layer and it leads to the reduction of the concentration of holes in the perovskite slab. And since the perovskite layer serves as a primary conducting path for charged carriers [44], which in this case holes, it gives rise to the decrease in the electronic conductivity and in turn the total electrical conductivity at high temperatures. Furthermore, the introduction of the smaller La^{3+} ions into the layered structure triggers the generation of negatively – charged species and facilitates the charge redistribution process due to the contraction of the unit cell. Therefore, it has a more pronounced impact on the decreased total conductivity. As a result, the decreasing slope of LSF0.3 oxide is steeper than that of LSF0.2.

In case of LSF0.4 where the perovskite phase dominates the entire oxide, the effect of the semiconductor – to – metal – like transition is barely noticed because the La^{3+} ion content is mainly enriched in the perovskite phase [44]. As a result, the apparent total conductivity reflects the total conductivity found in $La_{1-x}Sr_xFeO_3$ oxides [66] and the decrease in the electrical conductivity above 650ºC is derived primarily from the decline in the concentration of *p* – type charge carriers due to the formation of oxygen vacancies [67]. The defect reaction responsible for the reduction in the hole content is expressed in equation 3.4.

$$O_O^x + 2Fe_{Fe}^{\cdot} \rightleftharpoons 2Fe_{Fe}^x + V_O^{\cdot\cdot} + \frac{1}{2}O_2(g) \qquad (3.4)$$

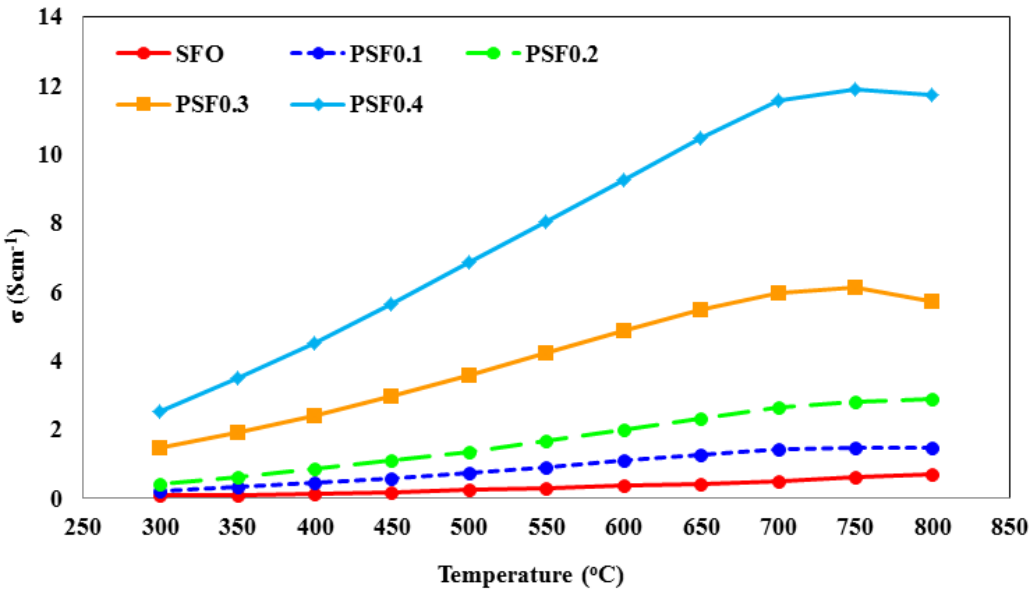

Figure 3. 7 Temperature – dependence electrical conductivity of PSFx oxides in air.

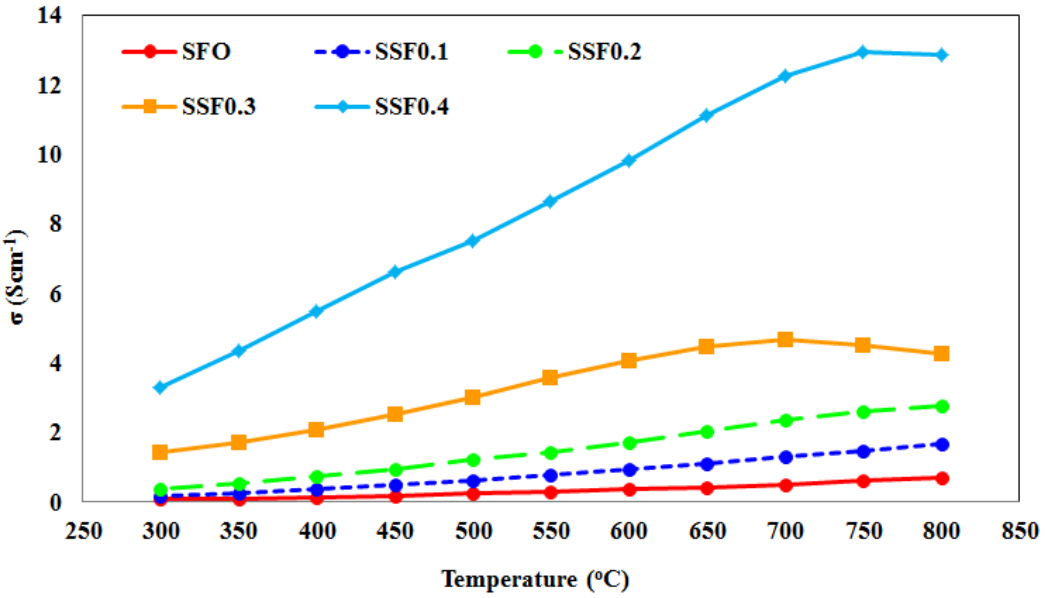

Figure 3. 8 Temperature – dependence electrical conductivity of SSFx oxides in air.

On the contrary, in Figures 3.7 and 3.8, the total electrical conductivities of PSFx and SSFx oxides in air clearly reveal the semiconducting behaviour over the experimental conditions. For all lanthanide – containing oxides, the total electrical conductivity increases as the concentration of the lanthanide dopants is raised. This observation is principally based on the effect of the presence of the perovskite phase

[44]. In general, the perovskite phase shows higher total electrical conductivity than the layered phase. When increasing lanthanide concentration, the amount of the perovskite phase steadily grows larger, which is identified by X – ray diffractometry, thereby increasing the total electrical conductivity.

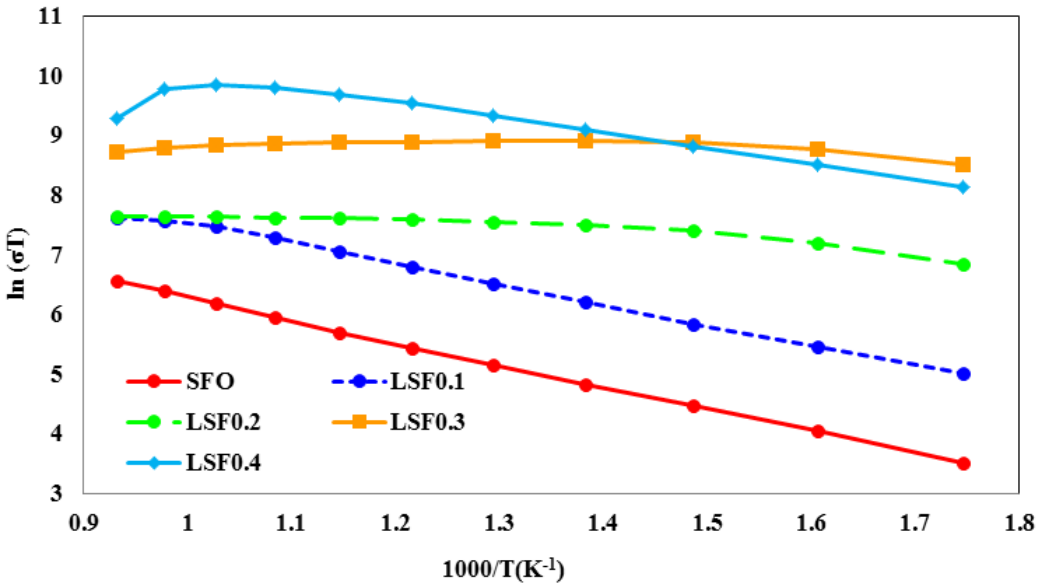

Figure 3. 9 Arrhenius plot for the electrical conductivity of LSFx oxides in air.

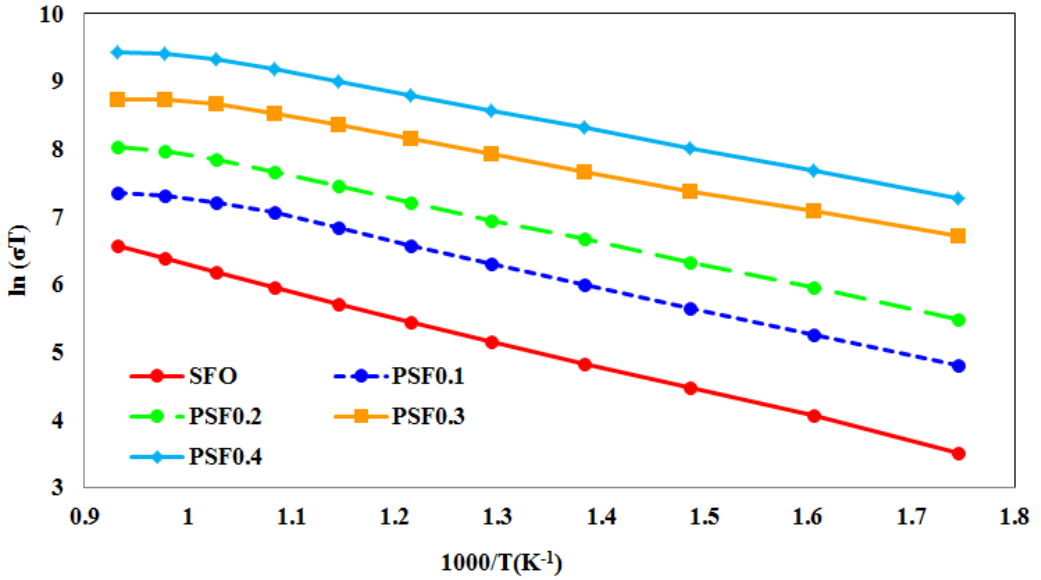

Figure 3. 10 Arrhenius plot for the electrical conductivity of PSFx oxides in air.

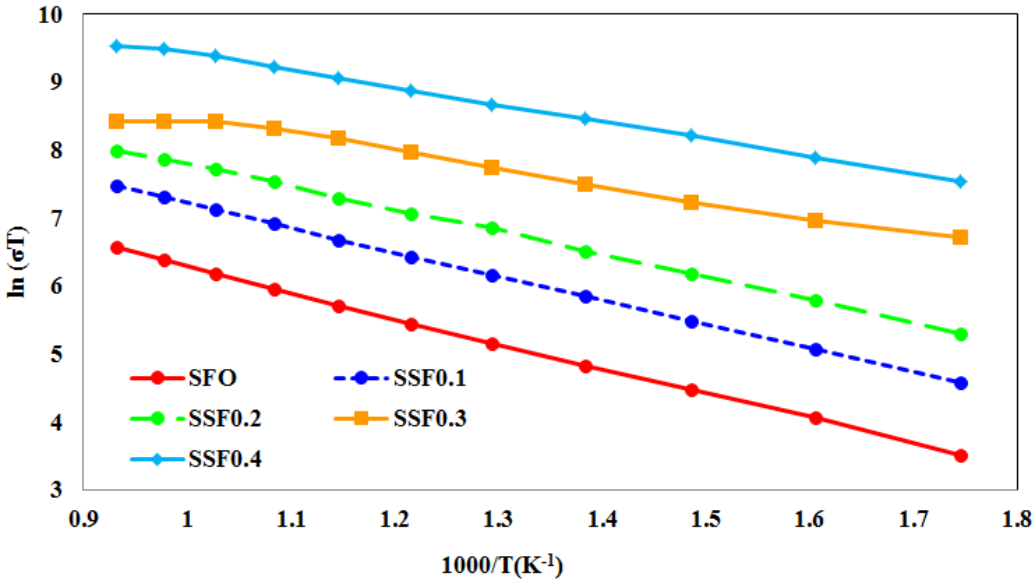

Figure 3. 11 Arrhenius plot for the electrical conductivity of SSFx oxides in air.

Being consistent with the temperature – dependence electrical conductivity plots, the Arrhenius plots of the undoped and LSF0.1 oxides in air presented in Figure 3.9 reveal the linear relationship between ln(σT) and 1000/T over the entire temperature range. This indicates the thermally – activated conduction behaviour by small polaron hopping mechanism as in the pure layered phase [68]. In addition, the Arrhenius plots of the other LSFx oxides also illustrate the change in the conduction mechanism from small polaron hopping to band theory mechanism, which corresponds to the conductivity plot in Figure 3.6 as well. The reason for the change in the conduction behaviour is the same as previously mentioned. Similarly, the observations of the Arrhenius plots for PSFx and SSFx oxides also support the small polaron hopping mechanism for the electrical conductivity in Figures 3.7 and 3.8.

Table 3. 1 Activation energy for the small polaron conduction mechanism of the lanthanide – doped oxides.

Composition (x)	Activation Energy (eV)		
	La – doped	Pr – doped	Sm – doped
0.0	0.322	0.322	0.322
0.1	0.289	0.282	0.306
0.2	0.159	0.277	0.287
0.3	0.121	0.227	0.200
0.4	0.222	0.237	0.216

Regarding the Arrhenius plots, the activation energy for the semiconduction by small polaron hopping can be calculated from the slope of the straight line by using the equation fitted,

$$\ln(\sigma T) = \ln A - \frac{E_a}{kT} \tag{3.5}$$

where A is a pre – exponential factor, k is the Boltzmann's constant, T is the absolute temperature, E_a is the activation energy for the small polaron hopping mechanism. The activation energy derived from the aforementioned equation is tabulated in Table 3.1. Obviously, all lanthanide – doped oxides demonstrate the similar trend in which the activation energy decreases with increasing dopant content and reaches the lowest value at x = 0.3. Increasing more lanthanide content than x = 0.3, however, increases the activation energy. The observation presumably stems from the effect of the presence of both the perovskite and the layered phases [69]. Typically, in the single layered phase, the hole conduction for *p* – type semiconducting behaviour takes place in the octahedral FeO_2 sheet along the *ac* plane and the charge transfer across the octahedral and the polyhedral slabs is inhibited by the high energetic barrier induced from the deviation of the Fe – O – Fe angle from 180º [40]. As a result, the electronic conduction is considered anisotropic. Conversely, the electronic conduction in typical perovskites is isotropic due to the continuous network of octahedrally – coordinated iron units. The presence of the perovskite phase in the system provides more possible pathways for the hole conduction instead of being restricted in the perovskite sheets of the layered phase. Then, the activation energy is decreased. Nevertheless, when the perovskite phase contributes the most to the whole system as in LnSF0.4, where Ln are lanthanide ions, the isotropy of the electronic conduction causes electronic holes to migrate with longer path length and it is reflected in the increase in the activation energy. This means that the appropriate amount of the perovskite phase and the layered phase should yield the fastest channel for hole migration, which is at the com position of x = 0.3 in this instance.

3.2.2 $Sr_4M_yFe_{6-y}O_{13}$ (M = Co, Ni)

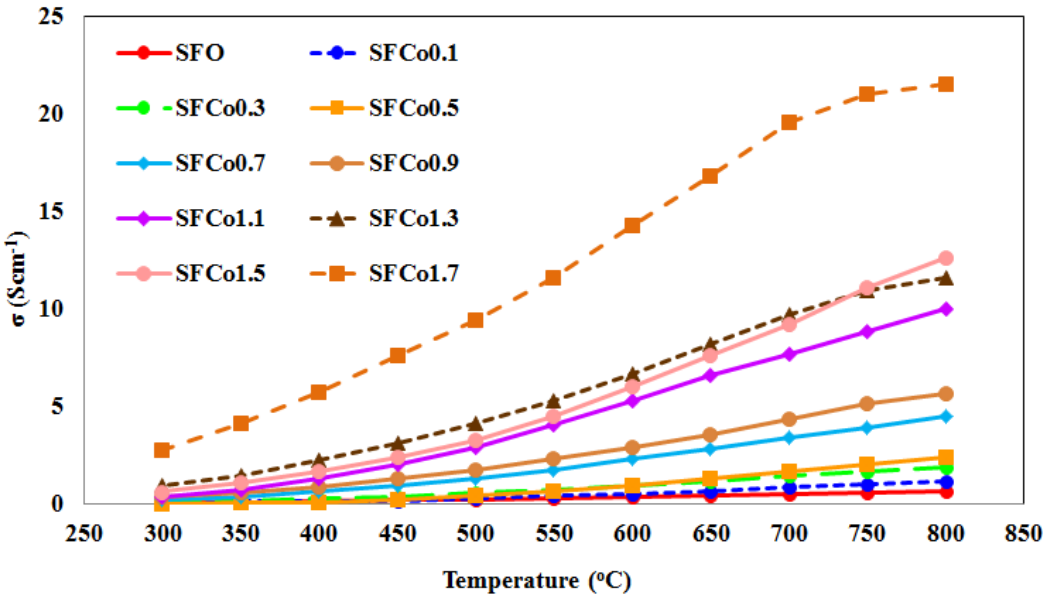

Figure 3. 12 Temperature – dependence electrical conductivity of SFCox oxides in air.

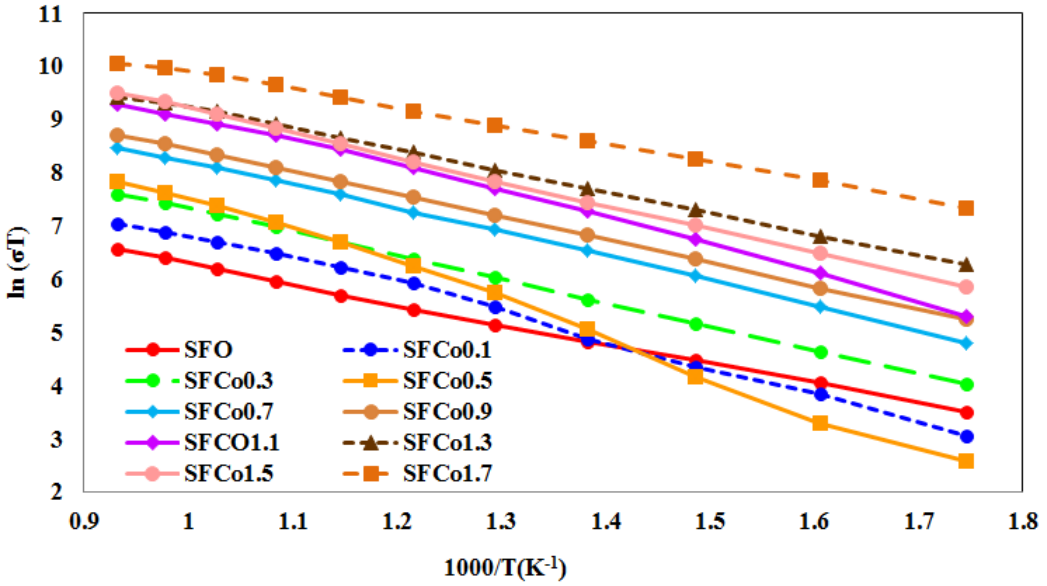

Figure 3. 13 Arrhenius plot for the electrical conductivity of SFCox oxides in air.

According to the temperature – dependence total electrical conductivity of SFCox oxides in air shown in Figure 3.12, the total electrical conductivity increases with increasing temperature and it is also evidenced by the linear relationship between ln(σT) and 1000/T in Figure 3.13. This indicates the polaronic mechanism for semiconducting behaviour as in the pure layered phase [68]. Moreover, upon raising

the concentration of Co dopant, the total electrical conductivity also increases and it possibly arises from several reasons. In term of the improvement in the electronic conduction, the substitution of Fe^{3+} with smaller ions either Co^{2+} or Co^{3+} weakens the M^{n+} - O bond between O 2p and M 3d orbitals, where M^{n+} is the transition metal ions, which in turn results in the increased total electrical conductivity [41, 63]. In addition, the substituting Co^{3+} ion is susceptible to charge disproportionation reaction into Co^{2+} and Co^{4+}in the polyhedral layer and generates more electronic charge carriers. The defect reaction is expressed below [56, 70].

$$2Co_{Fe}^{x} \rightarrow Co_{Fe}^{\cdot} + Co_{Fe}^{\prime} \tag{3.6}$$

The addition of Co dopant into the layered phase can also raise the hole mobility since the polaron energy level at Co sites is shallower than the Fe sites in the undoped layered phase [71]. Therefore, the Co sites are less likely to entrap electronic holes for longer period of time. For the enhanced ionic conduction, the replacement of Fe^{3+} with Co^{2+} induces the formation of oxygen vacancy by the following reaction [63].

$$2CoO + O_{O}^{x} + 2Fe_{Fe}^{x} \rightarrow V_{O}^{\cdot\cdot} + 2Co_{Fe}^{\prime} + Fe_2O_3 \tag{3.7}$$

Furthermore, the Co^{2+} ions are prone to thermal reduction at elevated temperatures and the reaction, which is described in equation 3.8, subsequently produces additional oxygen vacancies [56].

$$O_{O}^{x} + 2Co_{Fe}^{x} \rightarrow V_{O}^{\cdot\cdot} + 2Co_{Fe}^{\prime} + \frac{1}{2}O_2(g) \tag{3.8}$$

However, at the composition of x = 1.5, the total electrical conductivity slightly falls below that at x =1.3. The small decline in the total electrical conductivity may originate from the association of point defects to form defect clusters at high Co concentration [56] and these defect clusters reduce the numbers of ionic carriers. The plausible defect associates can be illustrated in the equations below.

$$V_{O}^{\cdot\cdot} + Co_{Fe}^{\prime} \rightarrow (V_{O}^{\cdot\cdot} - Co_{Fe}^{\prime})^{\cdot} \tag{3.9}$$

$$V_{O}^{\cdot\cdot} + 2Co_{Fe}^{\prime} \rightarrow (Co_{Fe}^{\prime} - V_{O}^{\cdot\cdot} - Co_{Fe}^{\prime}) \tag{3.10}$$

$$2V_{O}^{\cdot\cdot} + Co_{Fe}^{\prime} \rightarrow (V_{O}^{\cdot\cdot} - Co_{Fe}^{\prime} - V_{O}^{\cdot\cdot})^{\cdot\cdot\cdot} \tag{3.11}$$

But when the concentration of Co dopants reaches x = 1.7, the total electrical conductivity remarkably increases more than the lower dopant – concentration oxides. One factor that plays a role in the increased total electrical conductivity of SFCo1.7

could be probably due to the presence of the appreciable amount of the perovskite phase [56].

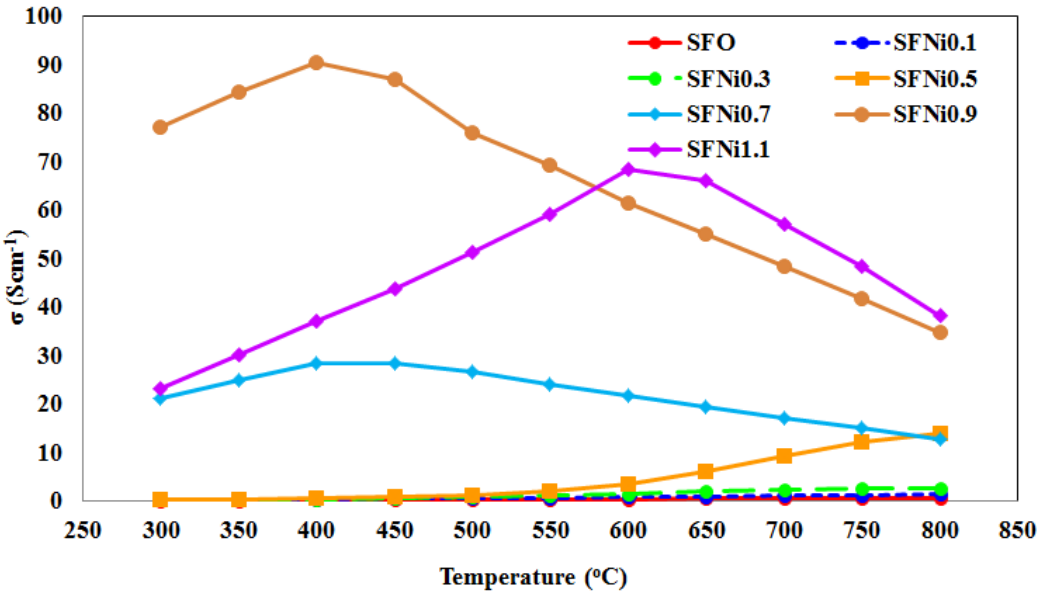

Figure 3. 14 Temperature – dependence electrical conductivity of SFNix oxides in air.

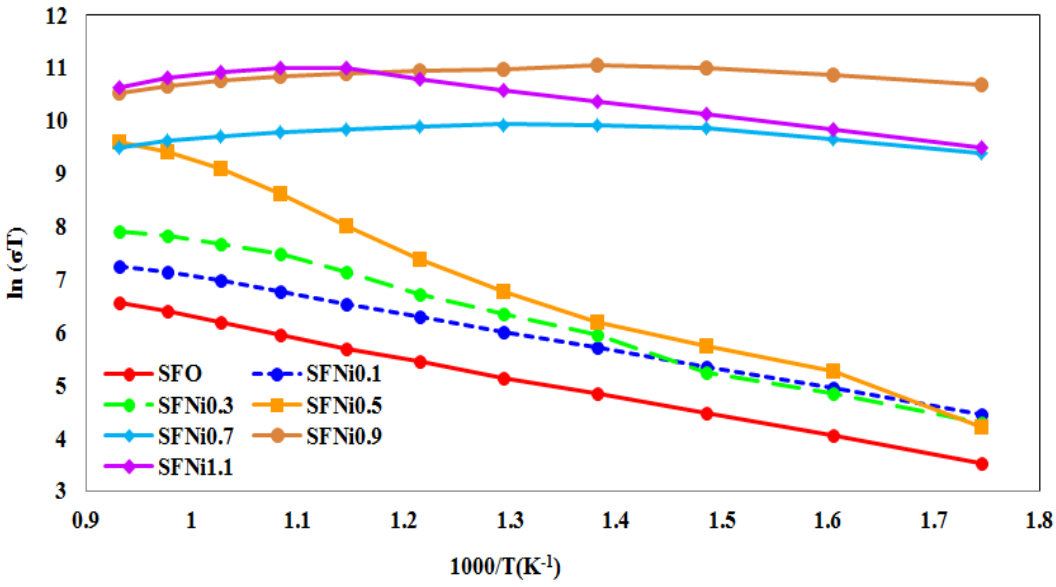

Figure 3. 15 Arrhenius plot for the electrical conductivity of SFNix oxides in air.

With regard to the dependency of the electrical conductivity on temperature in Figure 3.14, the electrical conductivity of SFNix oxides is raised as the Ni dopant content increases up to the composition of 0.9. The observation is likely to stem from

the nature of the dopant itself. Choi et al. [72] reported that Ni^{2+} ions had a tendency to generate holes when incorporated into perovskite and perovskite – related structures. The former statement is also supported by the presence of the perovskite phase in SFNix oxides since the composition of 0.3 onwards. In addition, the substitution of Fe^{3+} ions with Ni^{2+} ions provides the reinforcement of covalency for M^{n+} - O bonds and reduces the charge transfer gap between M 3d and O 2p orbitals [73]. Nevertheless, the electrical conductivity decreases when the composition of the Ni dopant is greater than 0.9. The reduction in the electrical conductivity may be ascribed to the structural distortion imposed by the excessive addition of Ni ions into the perovskite phase [74].

Moreover, the Arrhenius plots of SFNix oxides in Figure 3.15 demonstrate the linear relationship between ln(σT) and 1000/T in SFO, SFNi0.1,SFNi0.3, and SFNi0.5 oxides over the whole experimental temperature range and they apparently indicate the semiconducting behaviour that is dictated by small polaron hopping mechanism. However, the change in electrical conduction behaviour from semiconduction to metallic – like conduction is observed in SFNix oxides where x is above 0.5 and it is also evidenced by the changing slope in the Arrhenius plot of SFNi0.5 oxide. This behavioural transition can probably be described in term of the perturbation of the Fe – O – Fe periodic potential [75]. The incorporation of Ni dopants into the perovskite structure of SFNix oxides causes the irregularity in the periodic potential profile and introduces the Anderson localisation into the system. As a result, the localised state serves as a trap for any charge carriers, thereby decreasing the electrical conductivity at high temperatures.

จุฬาลงกรณ์มหาวิทยาลัย
Chulalongkorn University

Table 3. 2 Activation energy for the small polaron conduction mechanism of the transition metal – doped oxides.

Composition (x)	Activation Energy (eV)	
	Co – doped	Ni – doped
0.0	0.324	0.324
0.1	0.432	0.302
0.3	0.383	0.410
0.5	0.590[a], 0.501[b]	0.580
0.7	0.390	0.129
0.9	0.369	0.107
1.1	0.421	0.213
1.3	0.341	-
1.5	0.392	-
1.7	0.292	-

[a]calculated in the range from 450^{o}C to 800^{o}C
[b]calculated in the range from 300^{o}C to 450^{o}C

Likewise, the activation energy for small – polaron semiconduction of each transition metal – doped layered oxide is computed based on the equation 3.5 and their corresponding values are shown in Table 3.2. In SFCox oxides, the activation energy remains necessarily constant over the range of compositional variation but shows a decreasing trend at high dopant concentration. The decline in the activation energy results from the presence of the perovskite phase [69] that aid electronic charge carriers to migrate over the multiphase system. In relation to that, at the composition of 0.5, the activation energy reaches two maxima, 0.590 at higher temperature and 0.501 at lower temperature. The change in slopes for SFCo0.5 oxide may probably be due to either structural change or conduction mechanism change at elevated temperatures. In case of SFNix oxides, the similar trend in the activation energy is also observed and it peaks at x = 0.5 as well. Therefore, the explanation for the decrease in the activation energy of SFCox oxides might be applicable to this instance.

3.3 Thermogravimetric Analysis

Thermogravimetric analyses of all samples were carried out in air in the temperature range from 30°C to 1000°C with the heating rate of 5°C/min and oxygen non – stoichiometry for each oxide is calculated based on the following assumption that there are no exchanges between solid and gaseous phases except the evolution of oxygen gas [76-78].

$$Ln_xSr_{4-x}Fe_6O_{13-\delta_0}(s) \rightarrow Ln_xSr_{4-x}Fe_6O_{13-\delta}(s) + \frac{\Delta\delta}{2}O_2(g) \quad (3.12)$$

or $$Sr_4M_yFe_{6-y}O_{13-\delta_0}(s) \rightarrow Sr_4M_yFe_{6-y}O_{13-\delta}(s) + \frac{\Delta\delta}{2}O_2(g) \quad (3.13)$$

$$\Delta\delta = \delta - \delta_0 = \frac{\Delta m}{m_0} \times \frac{M_{mol}}{M_O} \quad (3.14)$$

where M_{mol} is the molecular weight of the complex oxide; M_O is the atomic weight of oxygen; m_0 is the weight of the sample under the initial condition of experiment; $\Delta\delta$ and δ are the relative and absolute values of oxygen non – stoichiometry; and δ_0 is the oxygen non – stoichiometry at the initial condition which is approximated as zero at room temperature.

3.3.1 $Ln_xSr_{4-x}Fe_6O_{13}$ (Ln = La, Pr, Sm)

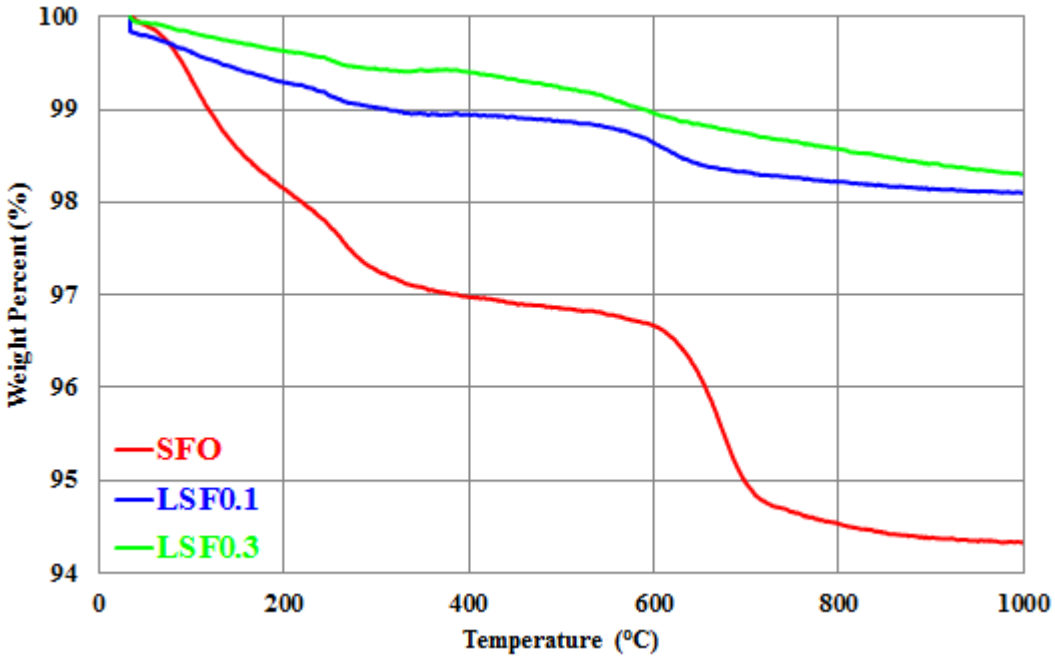

Figure 3. 16 Thermograms of LSFx oxides (x = 0.1, 0.3) in air with the heating rate of 5°C/min.

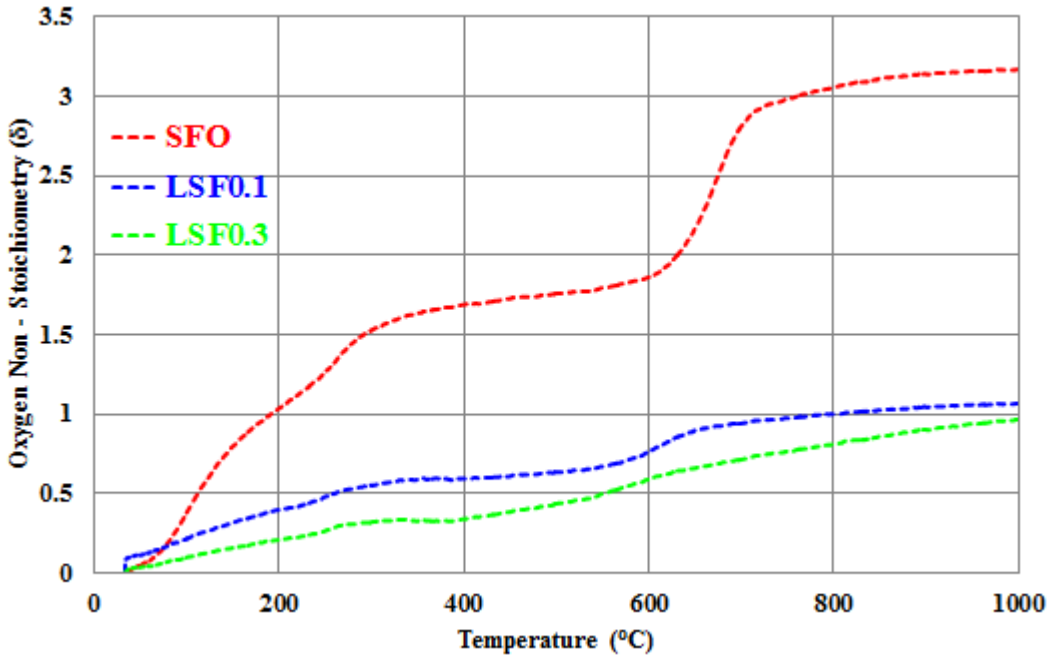

Figure 3. 17 Oxygen non stoichiometry of LSFx oxides (x = 0.1, 0.3) in air as a function of temperature.

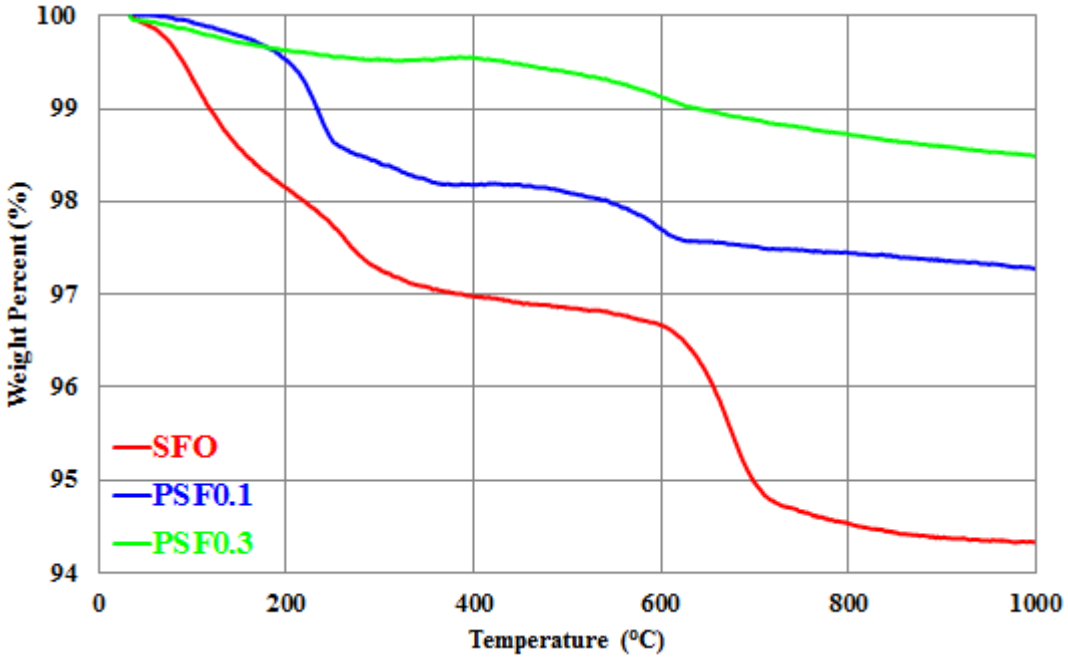

Figure 3. 18 Thermograms of PSFx oxides (x = 0.1, 0.3) in air with the heating rate of 5°C/min.

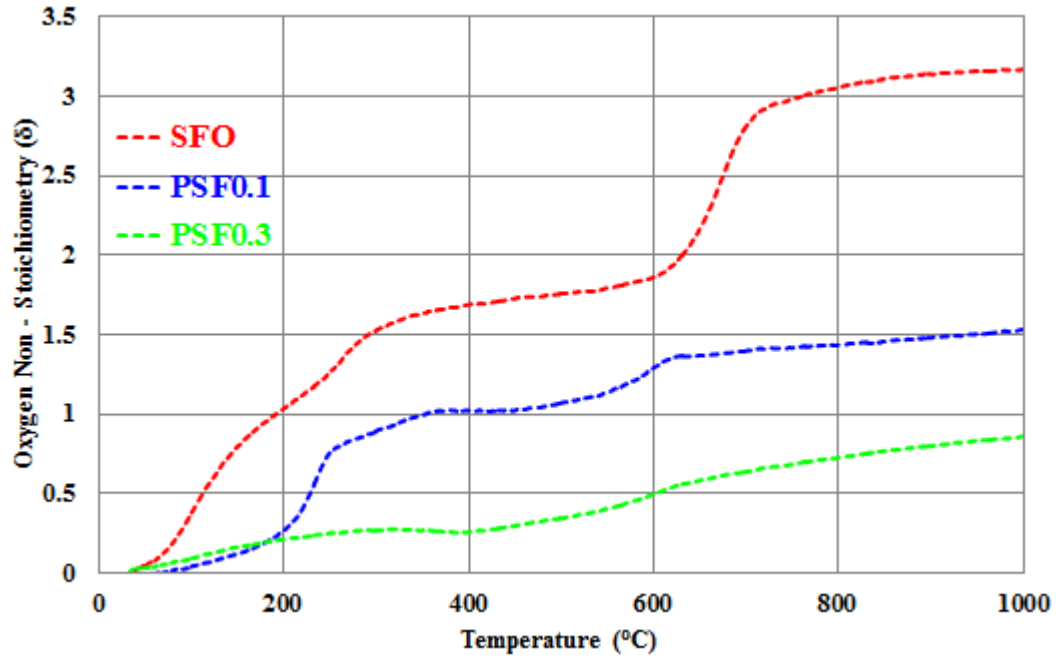

Figure 3. 19 Oxygen non stoichiometry of PSFx oxides (x = 0.1, 0.3) in air as a function of temperature.

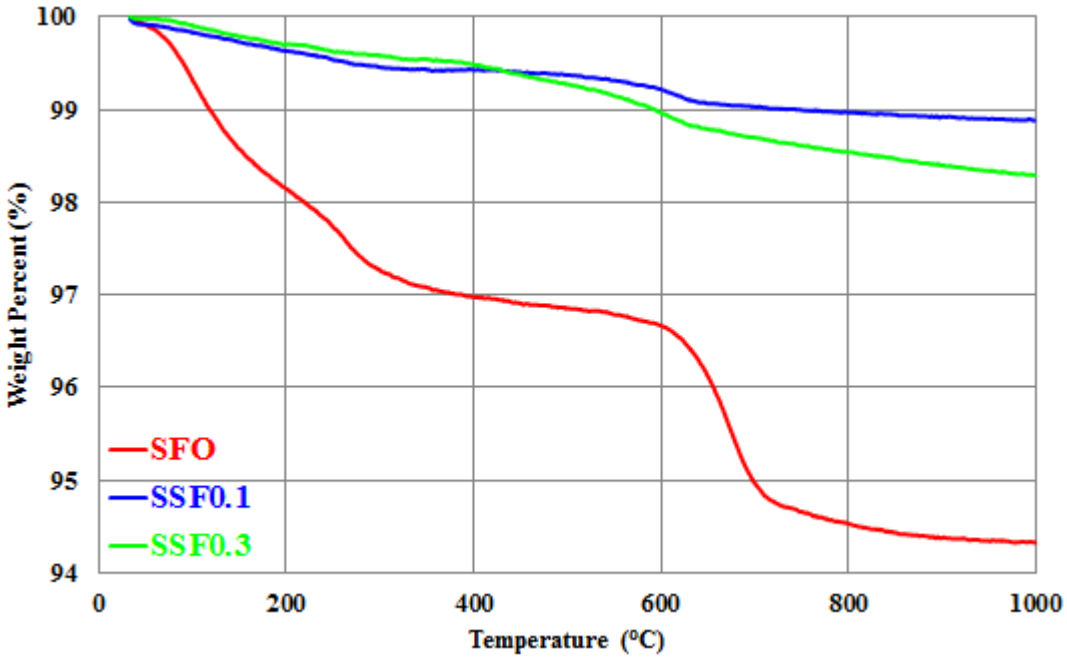

Figure 3. 20 Thermograms of SSFx oxides (x = 0.1, 0.3) in air with the heating rate of 5°C/min.

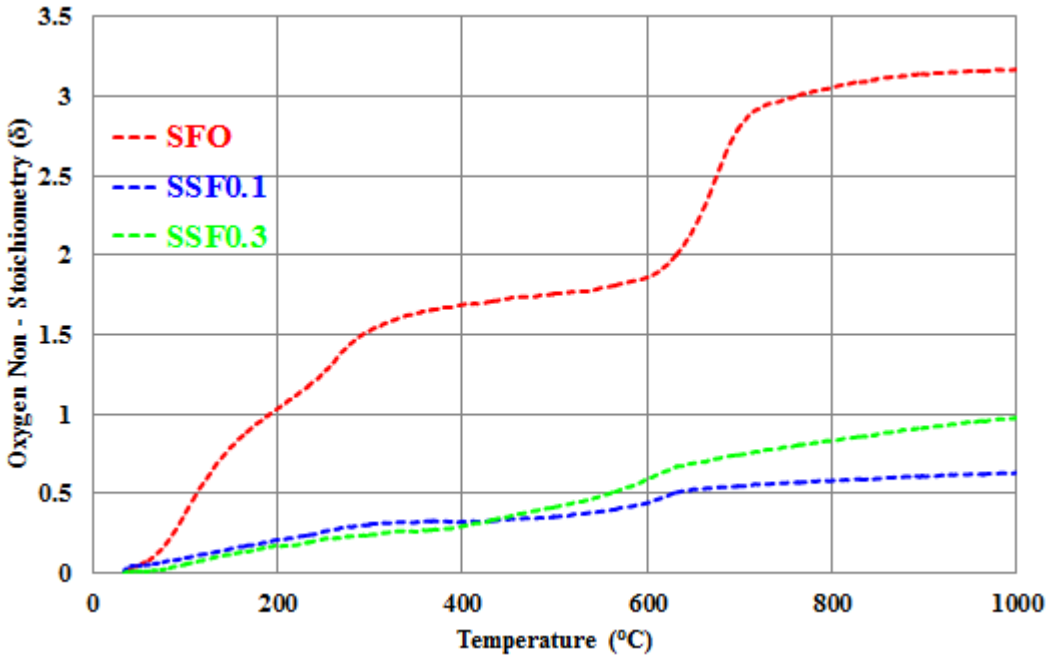

Figure 3. 21 Oxygen non stoichiometry of PSFx oxides (x = 0.1, 0.3) in air as a function of temperature.

Figures 3.16 – 3.21 show the thermograms of lanthanide – containing oxides at x = 0.1 and 0.3 in air with the heating rate of 5°C/min and the corresponding oxygen non – stoichiometry for each oxide. In general, all thermograms exhibit a similar trend in which the weight percent of the oxides decreases with increasing temperature. The weight loss at high temperature is attributed to the loss of lattice oxygen into molecular oxygen gas and the generation of electrons. This defect reaction is commonly found in oxide materials and it can be expressed as follow [79].

$$O_O^x \rightarrow V_O^{\cdot\cdot} + \frac{1}{2}O_2(g) + 2e' \qquad (3.15)$$

However, upon increasing lanthanide concentration, the weight percent increases; in other words, the oxygen non – stoichiometry decreases, and it raises a controversial issue against the general understanding that the increase in the dopant content would induce the formation of oxygen vacancy for charge compensation, thereby increasing the weight loss and oxygen non - stoichiometry. The contradictory observation may be corroborated by the segregation of lanthanide ions and the oxygen vacancy trapping at grain boundaries. For polycrystalline oxides, grain boundary is a two – dimensional defect that encompasses a particular crystallite and acts as an interface between two adjacent grains. In the present study, all LnSFx oxides also feature a multiphase system [44, 64] in which the layered, the perovskite and the *M* – type phases coexist and they lead to the formation of grain boundaries between each of them. Additionally, several

research groups have reported the presence of solute segregation at grain boundaries including lanthanide ions in both fluorite – and perovskite – based materials [80-83]. When these lanthanide ions are located at the grain boundaries, they prevent oxide ions from migrating and eventually evolving as the molecular oxygen because of its incomplete coordination number. At the grain boundary, most cations, especially lanthanide ions, are under – coordinated and lack oxide ions to complete their coordination sphere. Consequently, they would attract oxide ions and be surrounded to enhance their stability, which in turn impede the oxide ion migration across the grain boundary. Another factor that has an impact on the loss of lattice oxygen is oxygen vacancy trapping [84, 85]. Normally, structural discontinuities at grain boundaries are energetically unfavourable and they are stabilised by the existence of oxygen vacancies. In relation to that, when oxide ions migrate across the grain boundary, the oxygen vacancies are removed and it leads to the destabilisation at the interfacial boundary. As a result, in order to mitigate the adverse effect of oxide ion migration, oxygen vacancies cannot migrate away from the grain boundary and they are said to be trapped there. Upon increasing lanthanide concentration, both effects are more pronounced and they result in the weight gain compared to the undoped layered phase.

3.3.2 $Sr_4 M_yFe_{6-y}O_{13}$ (M = Co, Ni)

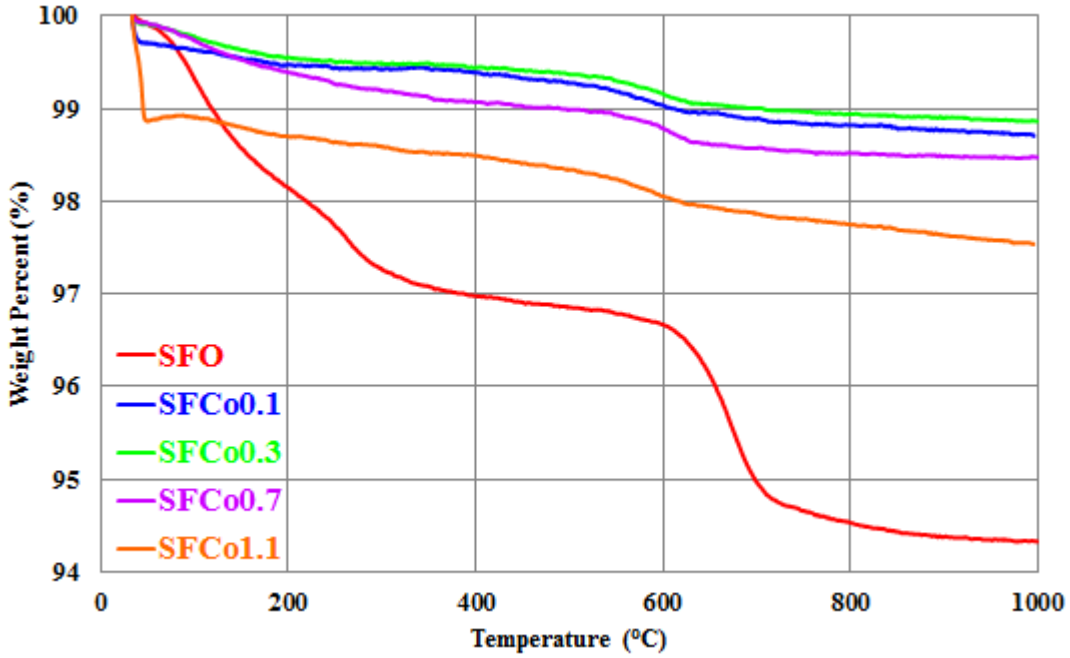

Figure 3. 22 Thermograms of SFCox oxides (x = 0.1, 0.3, 0.7, 1.1) in air and heating rate of 5°C/min.

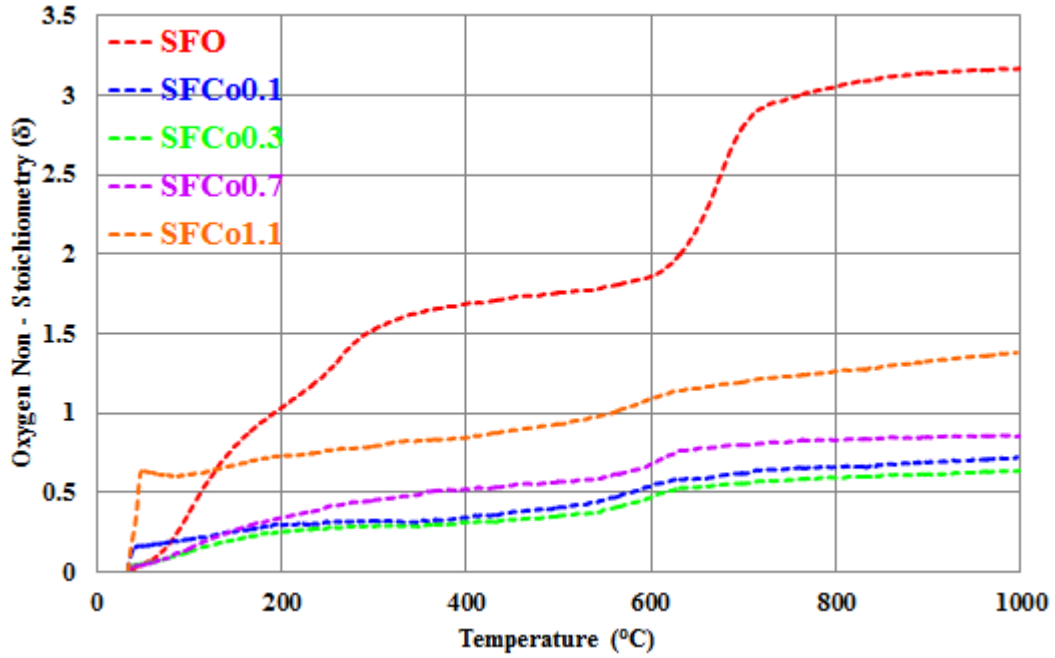

Figure 3. 23 Oxygen non stoichiometry of SFCox oxides (x = 0.1, 0.3, 0.7, 1.1) in air as a function of temperature.

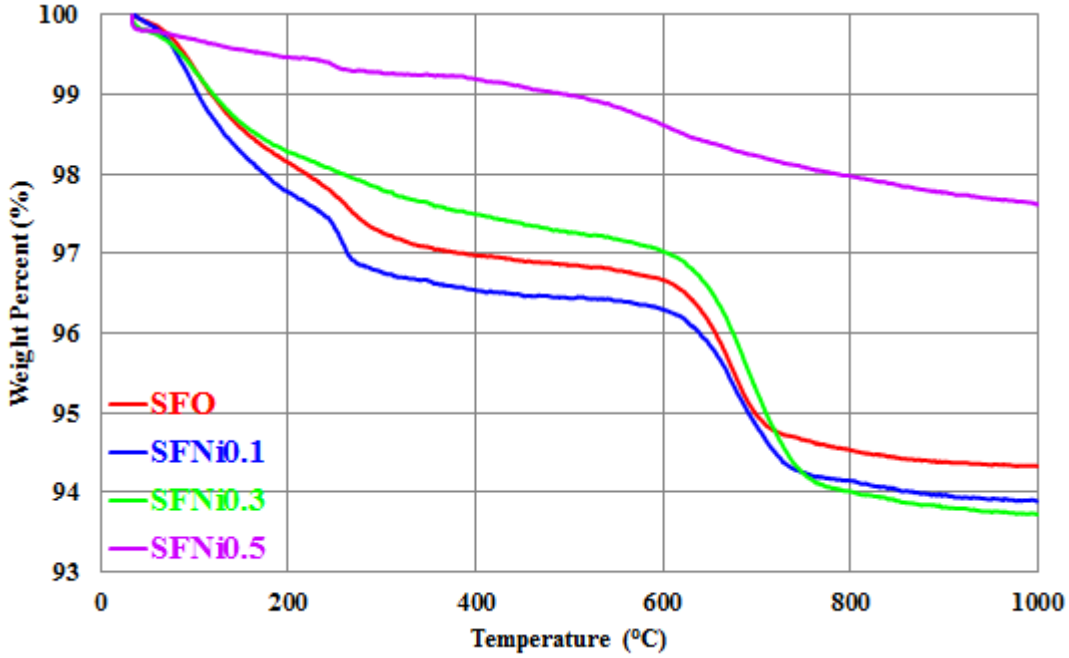

Figure 3. 24 Thermograms of SFNix oxides (x = 0.1, 0.3, 0.5) in air and heating rate of 5°C/min.

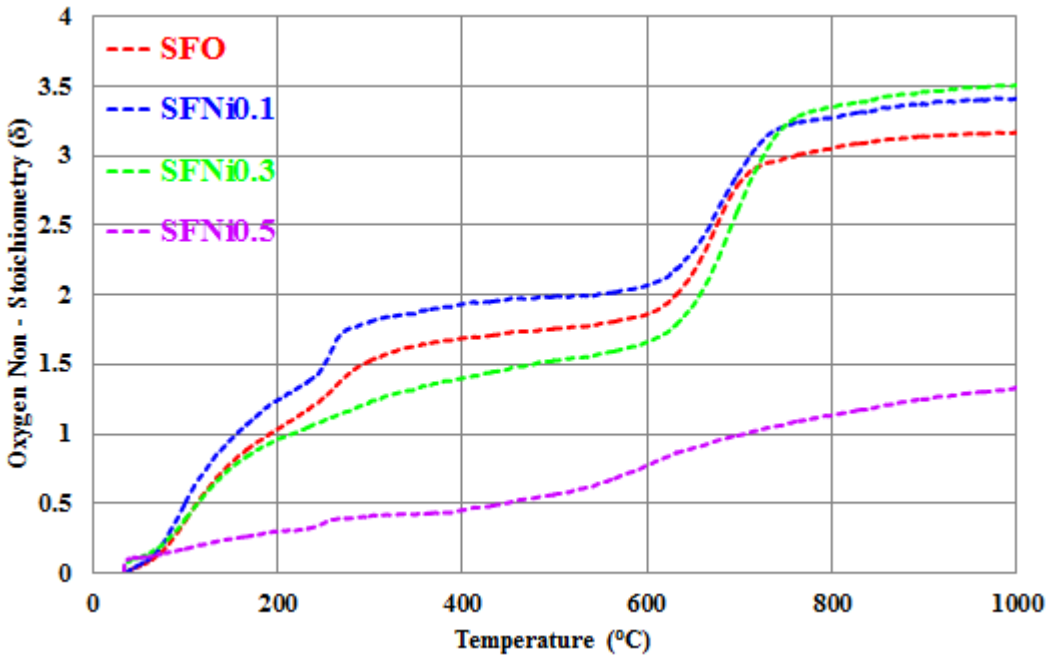

Figure 3. 25 Oxygen non stoichiometry of SFNix oxides (x = 0.1, 0.3, 0.5) in air as a function of temperature.

Similarly, the thermograms of SFCox oxides in air in Figure 3.22 and the related oxygen non – stoichiometry profile in Figure 3.23 reveal that the percent weight is raised appreciably for SFCo0.1 and SFCo0.3 oxides in comparison with the undoped layered phase but it continues to decrease for the compositions of 0.7 and 1.1. The increased weight loss or oxygen non – stoichiometry at high cobalt concentration probably arises from the formation of a large amount of oxygen vacancies despite the negligible amount of the perovskite phase present. As a consequence, the effects of the presence of grain boundaries and the cation segregation are minimal.

Unlike SFCox oxides, with regard to the thermograms of SFNix oxides (x = 0.1, 0.3, 0.5) in air in Figure 3.24 and the corresponding oxygen non – stoichiometry in Figure 3.25, they obviously indicate the insignificant difference in the weight loss between the undoped oxide and the doped ones with the compositions of 0.1 and 0.3 but they clearly show the considerable decrease in weight loss for SFNi0.5 oxide. The weight gain in the SFNi0.5 oxide possibly originates from the presence of the perovskite phase that triggers the formation of grain boundaries between these phases. Then, the observation can be explained on the grounds that have been previously mentioned.

3.4 Electrochemical Impedance Spectroscopy

Generally, electrochemical oxygen reduction reaction (ORR) of all oxides consists of multiple steps [52, 86-89] and they include gas – phase diffusion near the electrode surface, oxygen adsorption and dissociation on the electrode, surface diffusion of oxygen atoms, oxygen reduction to form oxide ions, incorporation of oxide ions into oxygen vacancies, and the oxide ion migration from the electrode to the electrode/electrolyte interface. In order to determine the degree to which each step contributes to the overall cathode polarisation, the deconvolution of Nyquist plots becomes the essential part. However, the aforementioned processes share similar time constants which complicate the deconvolution procedure. Therefore, in this study, a simple and reliable equivalent circuit model was employed on the basis that the processes involving the charge transfer steps have a smaller time constant while the diffusion – related steps have a larger one [90]. In addition, the Nyquist plot is fitted with the equivalent circuit model $R_{ohm}L_{wire}(R_1Q_1)(R_2Q_2)$, where R_{ohm} is the ohmic resistance generated from the electrolyte resistance as well as other ohmic losses due to Pt wires and meshes, electrode ohmic resistance, and contact resistance, L_{wire} is the inductive resistance caused by Pt wire, R_1 and CPE_1 are high – frequency resistor and constant – phase element related to charge transfer processes respectively, R_2 and CPE_2 are low – frequency resistor and constant – phase element related to diffusion processes respectively. The polarisation resistance (R_p) is the sum of R_1 and R_2 and is used for determining the activation energy of the ORR process. The example of the fitted Nyquist plot for PSF0.2 oxide is displayed in Figure 3.26.

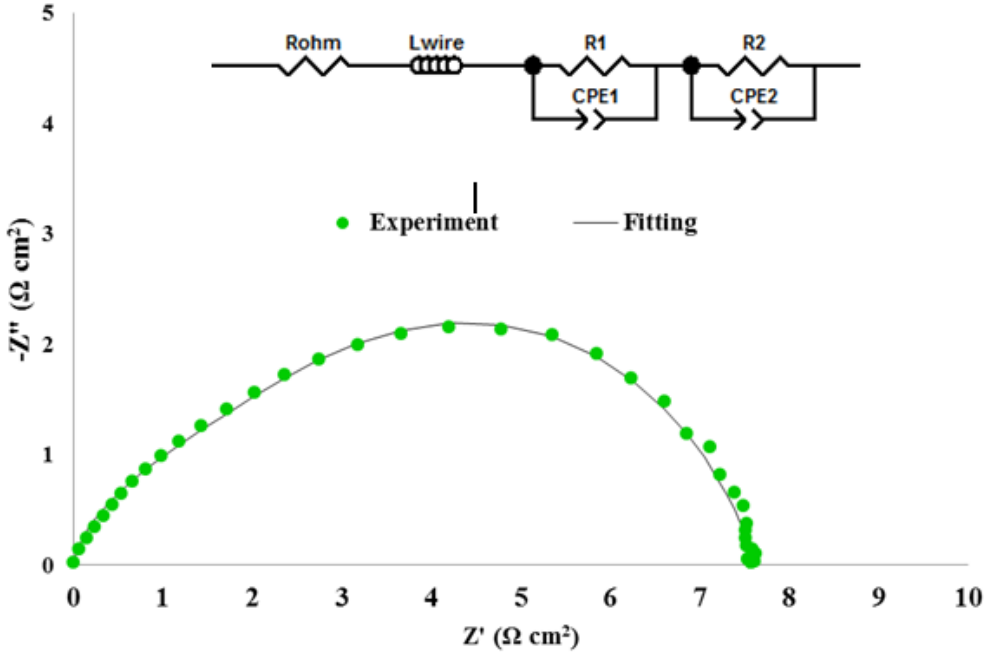

Figure 3. 26. Nyquist plots of PSF0.2 oxides at 800°C in air under open circuit conditions together with the fitting result.

3.4.1 $Ln_xSr_{4-x}Fe_6O_{13}$ (Ln = La, Pr, Sm)

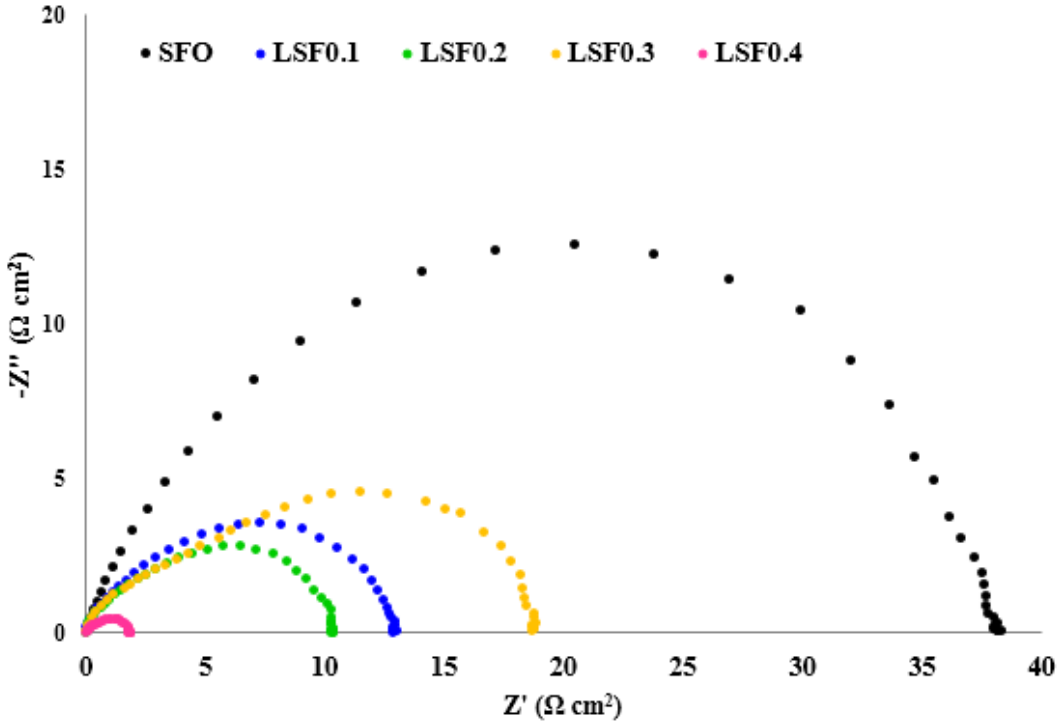

Figure 3. 27. Nyquist plots of LSFx oxides at 800°C in air under open circuit conditions.

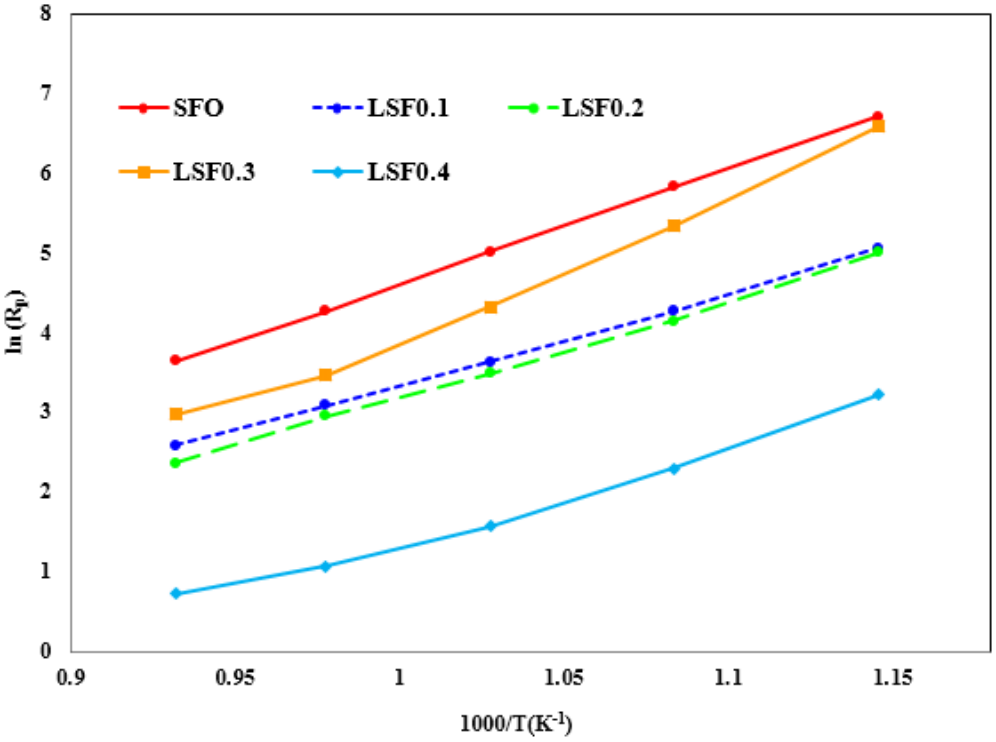

Figure 3. 28. Arrhenius plots for polarisation resistances of LSFx oxides in air under open circuit conditions.

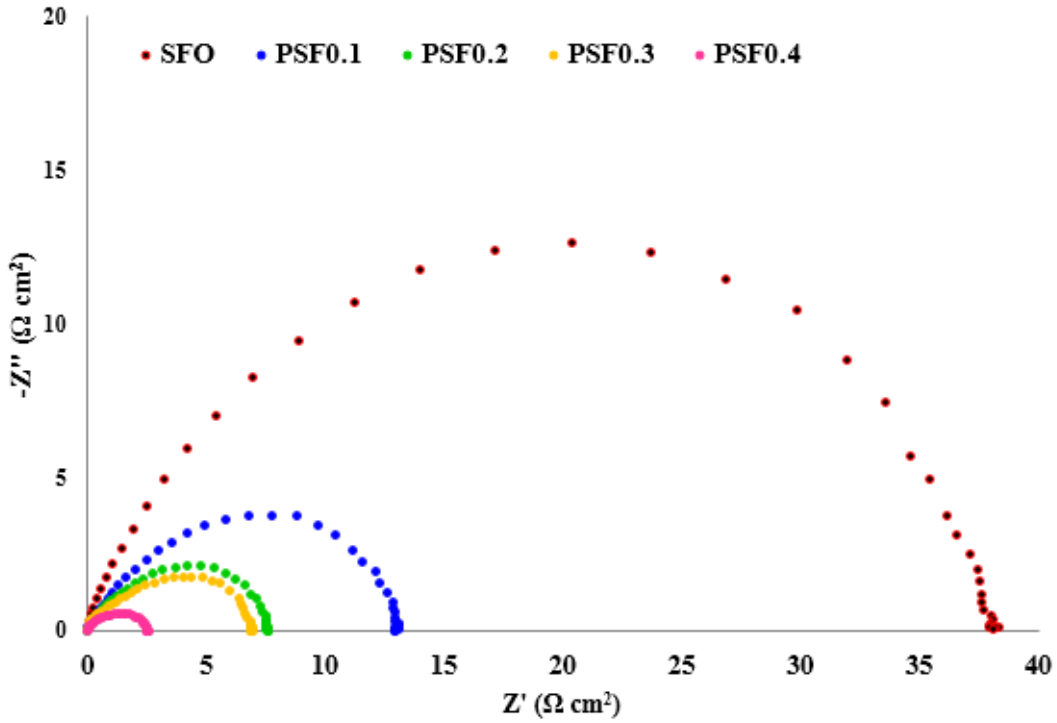

Figure 3.29. Nyquist plots of PSFx oxides at 800°C in air under open circuit conditions.

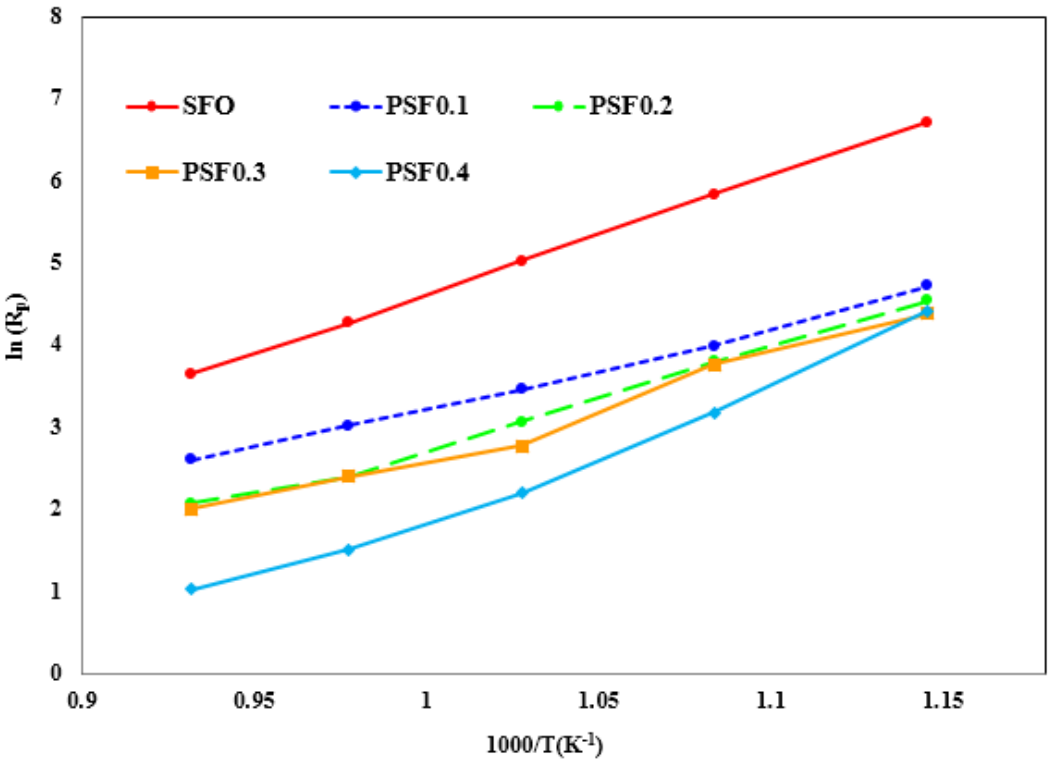

Figure 3.30 Arrhenius plots for polarisation resistances of PSFx oxides in air under open circuit conditions.

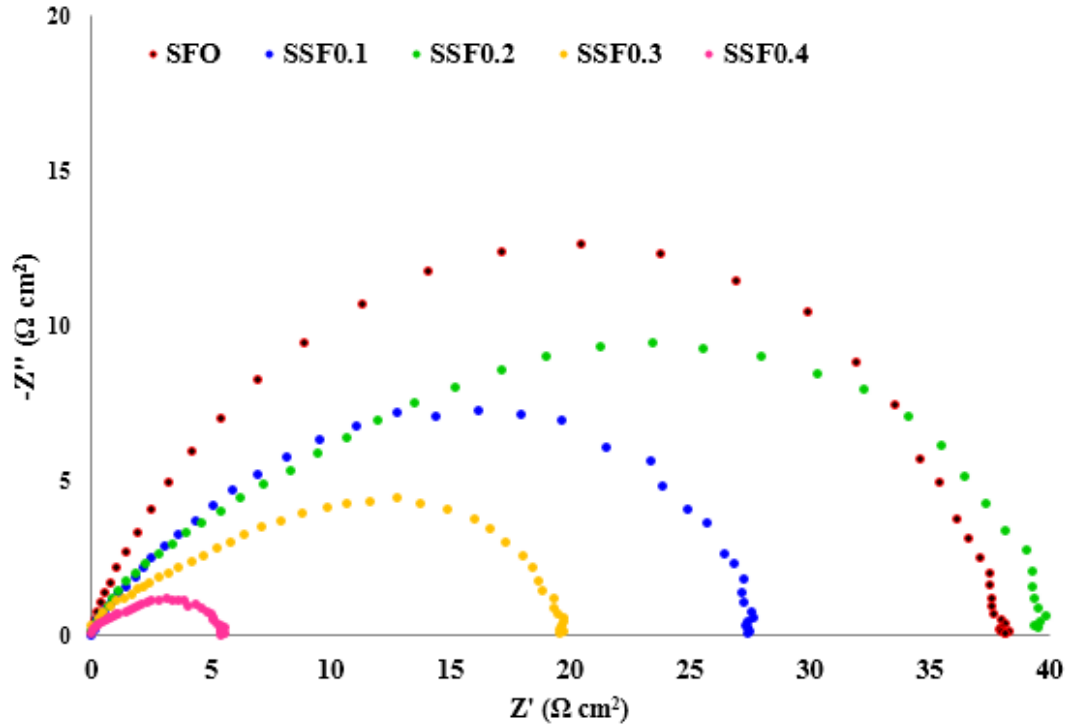

Figure 3. 31 Nyquist plots of SSFx oxides at 800°C in air under open circuit conditions.

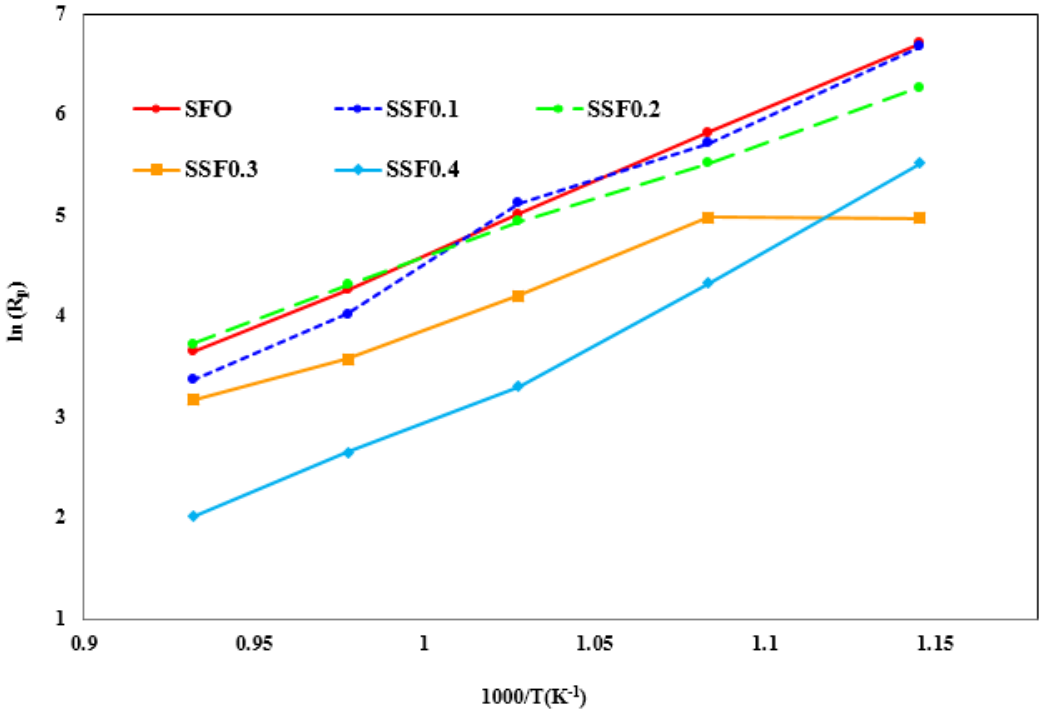

Figure 3. 32 Arrhenius plots for polarisation resistances of SSFx oxides in air under open circuit conditions.

Table 3. 3 Activation energy for the ORR process of lanthanide – containing oxides.

Composition (x)	Activation Energy (eV)		
	La – doped	Pr – doped	Sm – doped
0	1.24	1.24	1.24
0.1	0.95	0.84	1.34
0.2	1.05	1.03	1.02
0.3	1.48	0.99	0.80
0.4	1.01	1.38	1.42

According to the Nyquist plots of the lanthanide – doped oxides measured at 800^{o}C in air at open circuit conditions in Figures 3.27, 3.29, and 3.31, they share a common behaviour in which the polarisation resistance decreases with increased lanthanide content. The observation can be explained by introducing the synergistic effect of the layered phase and the perovskite phase [57]. In pure layered oxides, the oxide ion migration is considered anisotropic because they are confined to migrate within polyhedral layers. As a result, the ionic conduction is restricted. When increasing the lanthanide dopants, the perovskite phase content also increases as confirmed by XRD in Figures 3.1 – 3.3. Concerning the perovskite phase, oxide ions are able to migrate over the three – dimensional structure and it is assumed to be isotropic. Nevertheless, in the single – phase perovskite, the isotropic ionic conduction probably causes long migrating path length for oxide ion migration, which results in low oxygen diffusivity. Therefore, with the presence of both layered and perovskite phases where the perovskite dominates the entire system, the layered phase is embedded in the continuous network of the perovskite phase and it serves as a fast oxide ion diffusion channel. The schematic illustration is also demonstrated in Figure 3.33. Then, the oxygen reduction reaction is improved and reflected in the reduction in the activation energy of the oxides at the composition where the appreciable amount of the perovskite phase is observed.

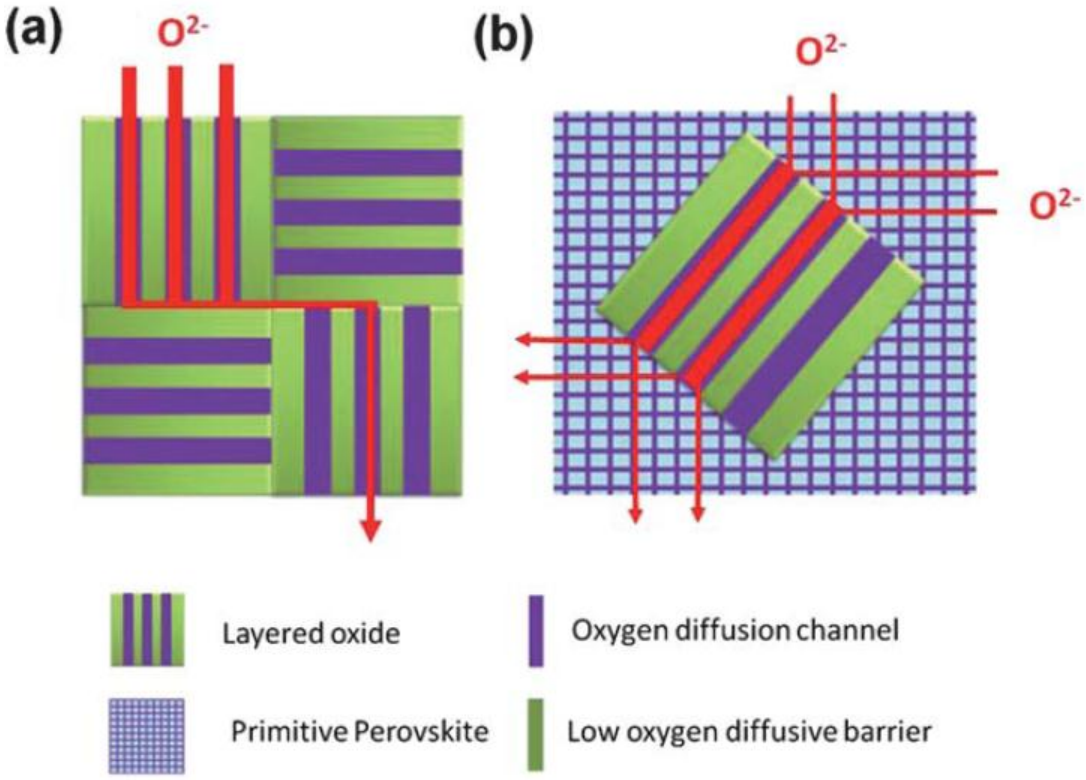

Figure 3. 33 Proposed mechanism of the facilitation of oxide ion diffusion in poly crystalline layered phase (a) and the layered phase embedded in perovskite (b).

However, LSF0.3 and SSF0.2 oxides do not follow the decreasing trend in polarisation resistance as reflected in the high activation energy for LSF0.3. Although the origin of this unusual behaviour has not been established in this study, several studies emphasised the microstructural and morphological effects on the increased polarisation resistance. Virka [91] described a number of important factors that adversely influenced the cathode polarisation. For instance, high cathode porosity and low tortuosity facilitated molecular oxygen diffusion and resulted in the reduced cathode polarisation resistance. Wang et al. [92] reported that the agglomeration of particles in $La_{0.8}Sr_{0.2}MnO_3$ caused the reduction in the triple phase boundary between the cathode and electrolyte and subsequently raised the cathode polarisation resistance. Another significant factor is the decreased oxygen vacancy concentration. Lee et al. [93] discovered that increasing Ce content in $SrMnO_3$ induced the strong hybridisation between Ce 4f or 5d and O 2p orbitals and resulted in the decrease in oxygen vacancy concentration. Consequently, the polarisation resistance in Ce – $SrMnO_3$ increased and the latter reference corresponds to the experimental investigation for the diminished oxygen non – stoichiometry of LSF0.3 in Figure 3.17.

3.4.2 $Sr_4M_yFe_{6-y}O_{13}$ (M = Co, Ni)

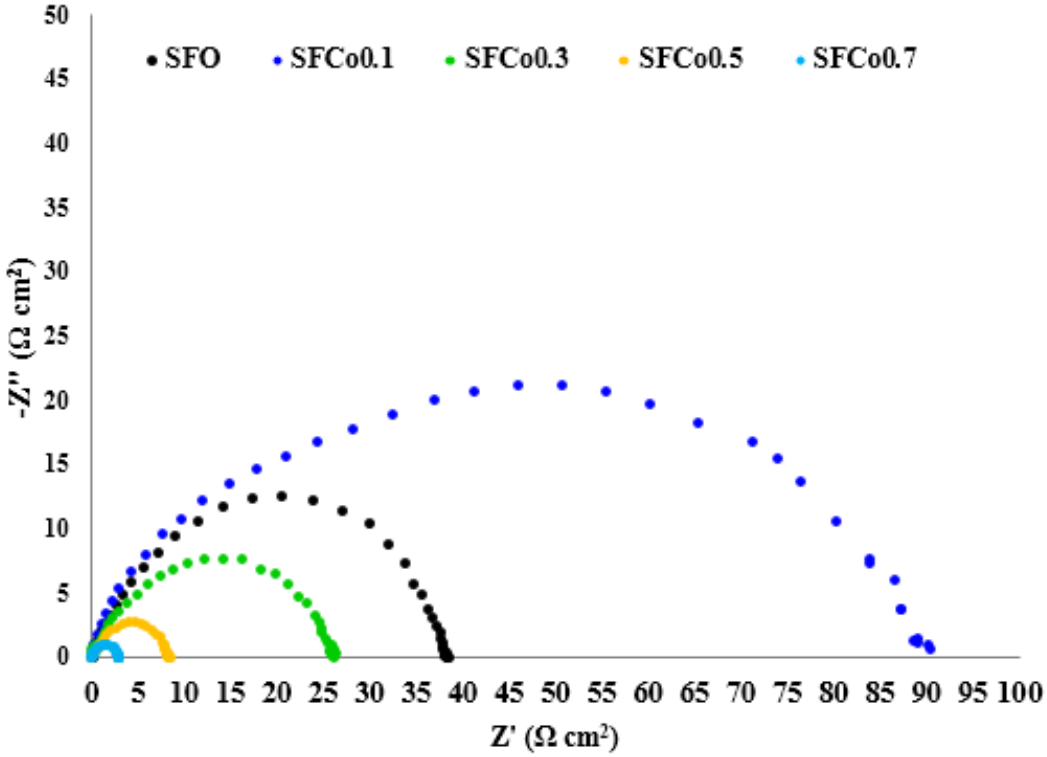

Figure 3. 34. Nyquist plots of SFCox oxides (x = 0.0 – 0.7) at 800°C in air under open circuit conditions.

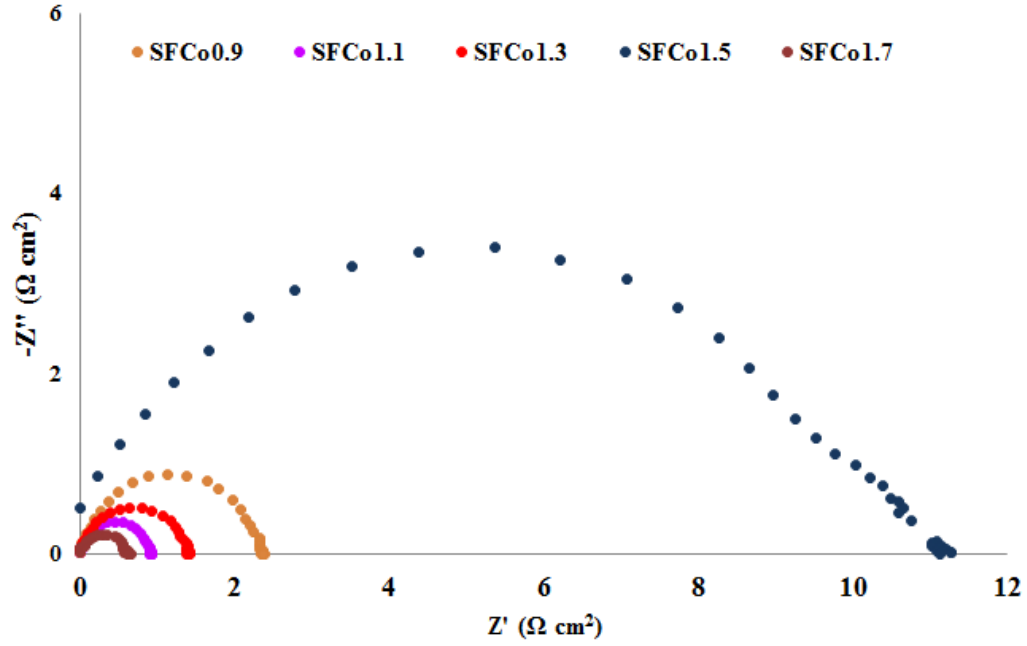

Figure 3. 35 Nyquist plots of SFCox oxides (x = 0.9 – 1.7) at 800°C in air under open circuit conditions.

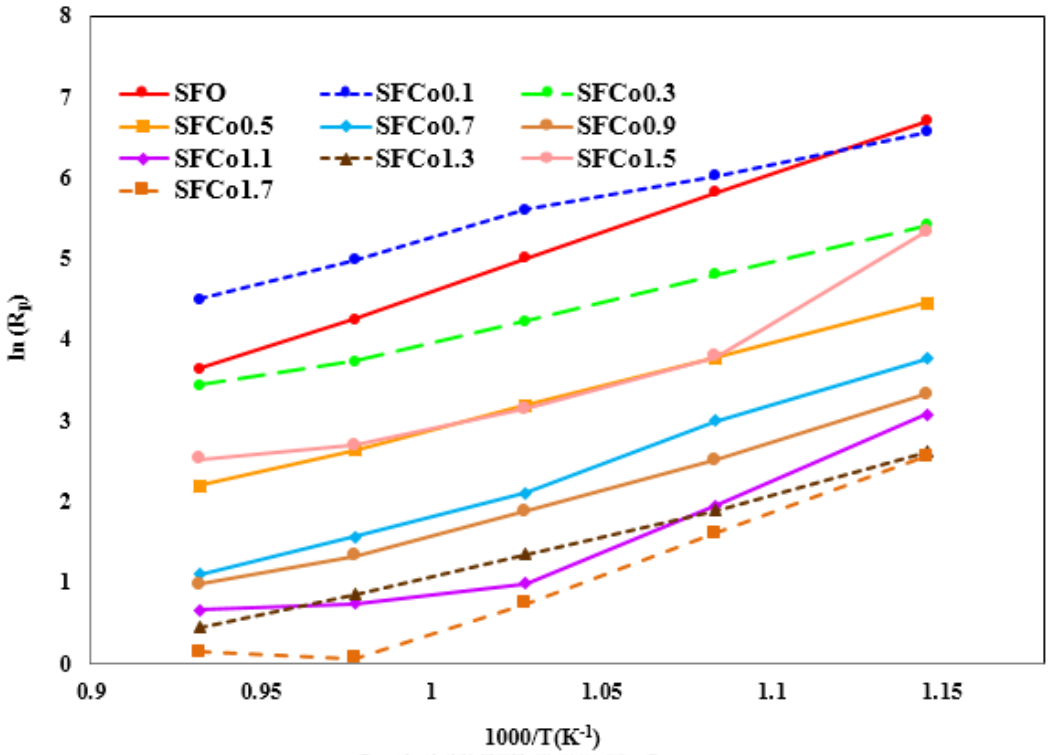

Figure 3. 36 Arrhenius plots for polarisation resistances of SFCox oxides in air under open circuit conditions.

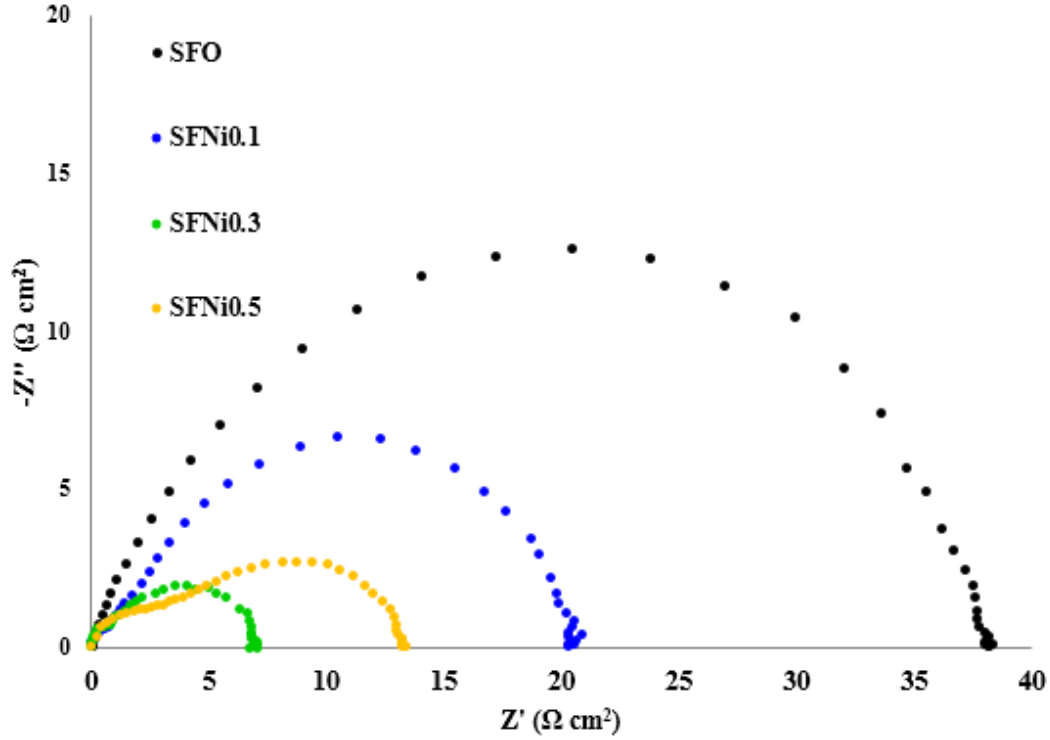

Figure 3. 37 Nyquist plots of SFNix oxides (x = 0.0 – 0.5) at 800°C in air under open circuit conditions.

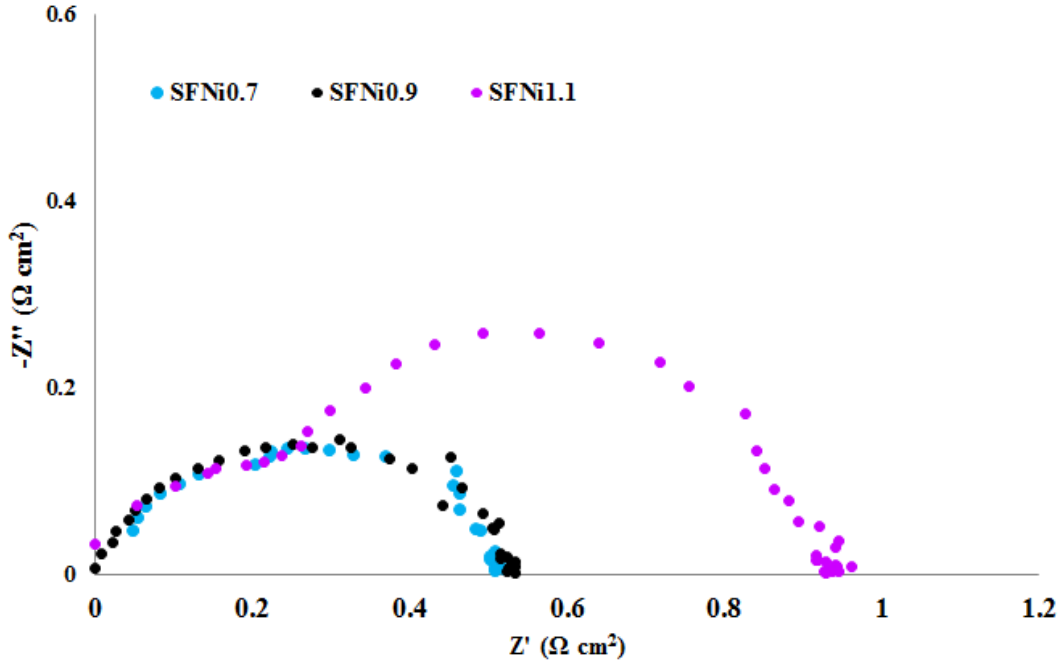

Figure 3. 38 Nyquist plots of SFNix oxides (x = 0.7 – 1.1) at 800°C in air under open circuit conditions.

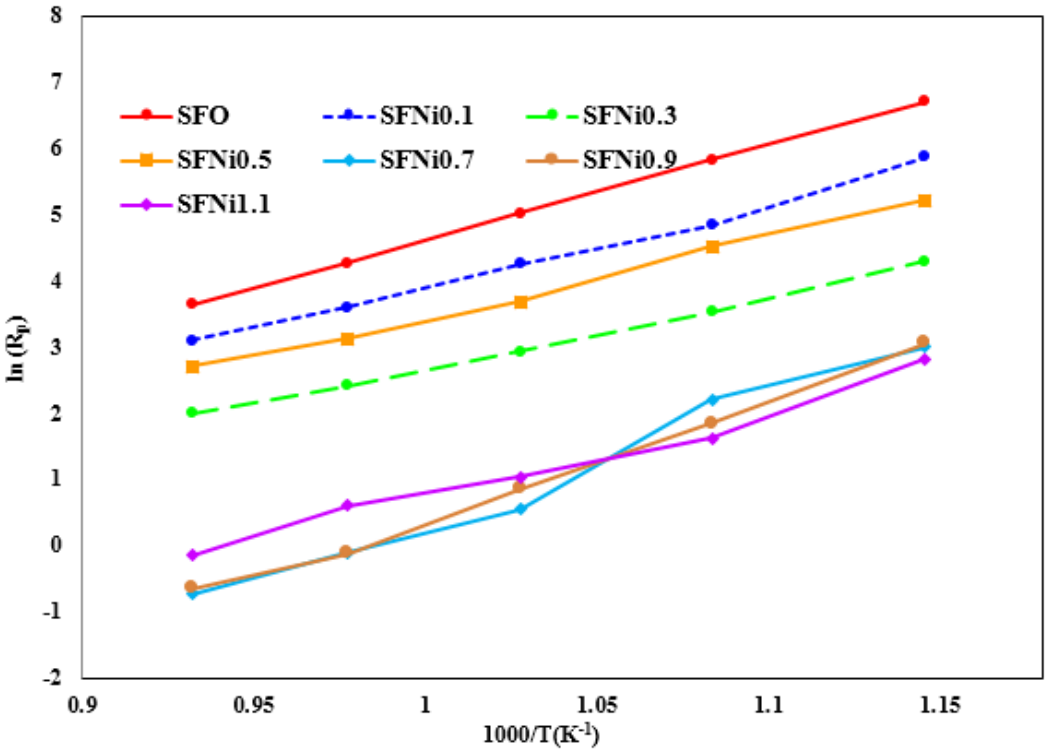

Figure 3. 39 Arrhenius plots for polarisation resistances of SFNix oxides in air under open circuit conditions.

The Nyquist plots of SFCox and SFNix oxides shown in Figures 3.34 – 3.35, 3.37 – 3.38, respectively, indicate the analogous relationship between the increasing dopant concentration and the decreasing polarisation resistance. The same explanation provided in case of lanthanide – doped oxides is also applicable to this instance. However, SFCo0.1, SFCo1.5, and SFCo1.3 oxides for the SFCox series and SFNi0.5 and SFNi1.1 for the SFNix series do not comply with the proposition of the synergy. Although the undoped layered phase exhibit the highest oxygen non – stoichiometry, which means the greatest oxygen vacancy content, the polarisation resistance is still large but less than that of SFCo0.1. This may be due to the microstructural impact on the oxygen reduction reaction process previously described. Likewise, the same reason can also be applied to the cases where the polarisation resistances of SFCo1.5 SFCo1.3, and SFNi1.1 oxides are larger than those of SFCo0.5, SFCo1.1, and SFNi0.7 respectively. In case of SFNi0.5 oxide, the increased polarisation resistance possibly stems from the decrease in oxygen non – stoichiometry, which is obviously seen in Figure 3.25.

Regarding the activation energy for the ORR process, there seems to have an independent correlation between the activation energy of the SFCox and SFNix oxides and the dopant composition, though.

Table 3. 4 Activation energy for the ORR process of transition metal – containing oxides.

Composition (x)	Activation Energy (eV)	
	Co – doped	Ni – doped
0.0	1.243208	1.243208
0.1	0.833511	1.099429
0.3	0.817029	0.923048
0.5	0.917614	1.040434
0.7	1.098911	1.624691
0.9	0.957375	1.51869
1.1	0.998603	1.126339
1.3	0.871384	-
1.5	1.110124	-
1.7	1.048541	-

3.5 X – ray Photoelectron Spectroscopy

3.5.1 $Ln_xSr_{4-x}Fe_6O_{13}$ (Ln = La, Pr, Sm)

3.5.1.1 Lanthanide spectra

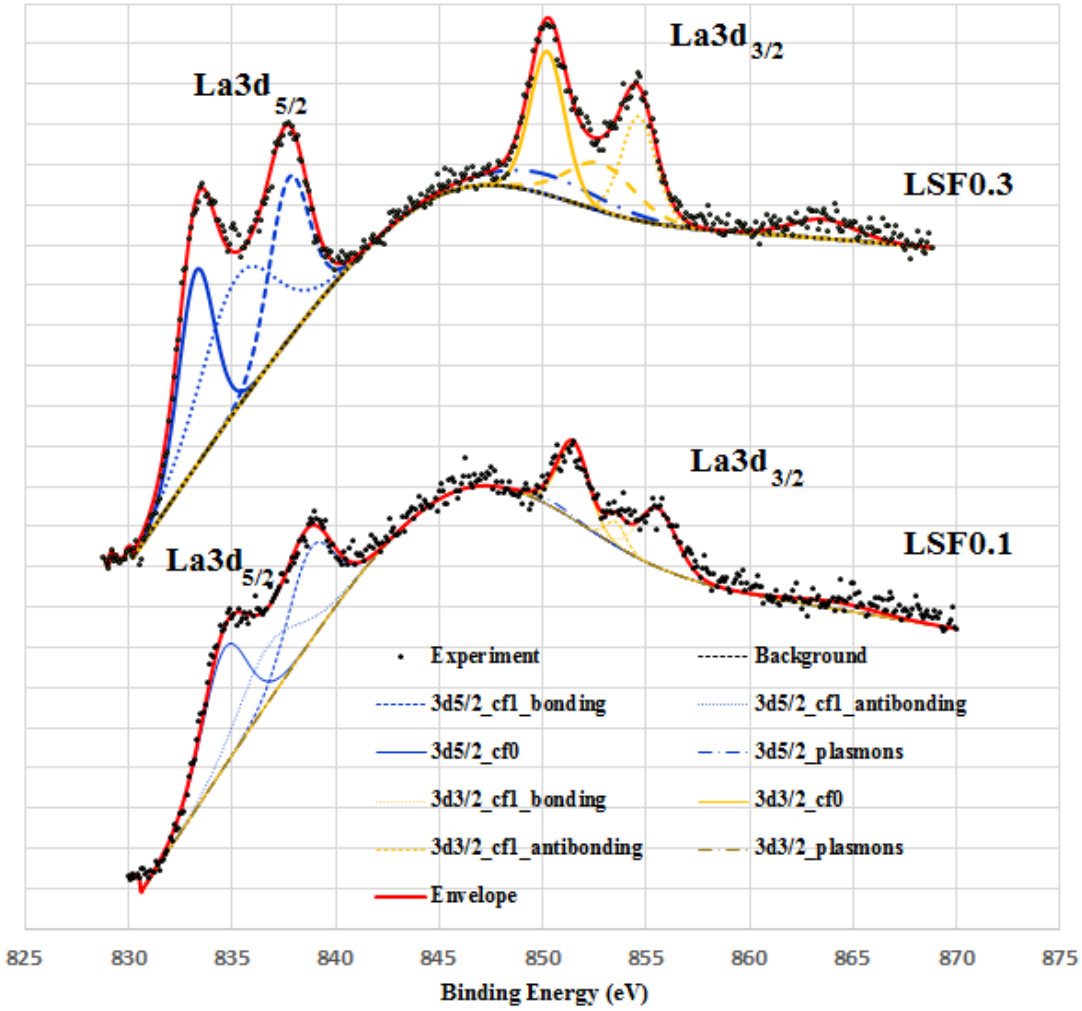

Figure 3. 40 La 3d core – level spectra of LSF0.1 and LSF0.3 oxides.

Figure 3.40 shows the deconvoluted spectra of La 3d core level for LSF0.1 and LSF0.3 oxides and they also share common spectral features [94, 95]. In relation to that, the La 3d core – level bands are split into La $3d_{5/2}$ and La $3d_{3/2}$ by the effect of spin – orbit splitting with the energy separation of approximately 17 eV for each peak pair. In addition, the split peak can be further broken down into four small peaks including the main core hole levels without charge transfer ($3d_{5/2}$ cf^0 and $3d_{3/2}$ cf^0), the satellites of the final state with charge transfer from ligand L to the 4*f* orbitals for bonding ($3d_{5/2}$ cf^1L - bonding and $3d_{3/2}$ cf^1L – bonding) and antibonding ($3d_{5/2}$ cf^1L - antibonding and $3d_{3/2}$ cf^1L – antibonding) components, and the plasmon peak resulting

from the component with the same quantum number ($3d_{5/2}$ – plasmons and $3d_{3/2}$ – plasmon). Concerning the intensity, LSF.0.1oxide exhibits the low signal – to – noise ratio due to the presence of extremely low La ions in the sample. However, the intensity of each peak obviously increases as the La dopant content increases. In essence, all peaks that are previously described correspond uniquely to La^{3+} ions and they imply that only La with +3 oxidation state exists in LSFx oxides.

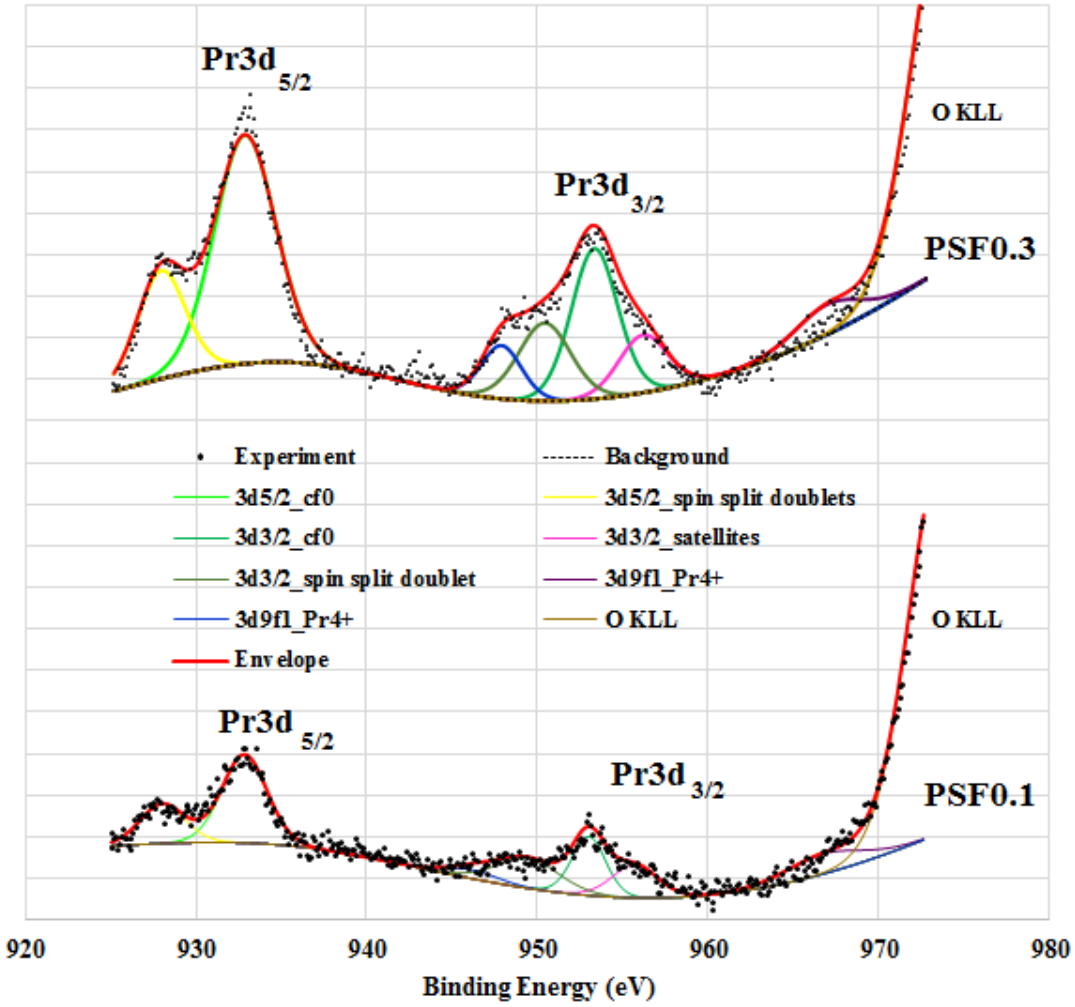

Figure 3. 41 Pr 3d core – level spectra of PSF0.1 and PSF0.3 oxides.

With regard to the deconvolution of the Pr 3d core – level spectra for PSF0.1 and PSF0.3 oxides in Figure 3.41, both spectra demonstrate the splitting behaviour of the Pr 3d core – level band induced by spin orbit coupling and the energy separation is found to be approximately 20 eV, which is in agreement with other literature data. Within the split peak [96, 97], it contains the primary the core – hole peaks without charge transfer ($3d_{5/2}$ cf^0 and $3d_{3/2}$ cf^0) and the relevant spin – split doublets ($3d_{5/2}$ – spin split doublet and $3d_{3/2}$ – spin split doublet). Apart from that, the satellite that is

superimposed in the Pr $3d_{3/2}$ band at around 956 eV is exclusively found. Also, the marker peaks responsible for the presence of Pr^{4+} are detected at approximately 967 and 947 eV and they belong to the electronic configuration of $3d^9 4f^1$ state. The high – intensity peak above 970 eV is caused by oxygen Auger electrons (O KLL). Nevertheless, the determination of the atomic ratio of $[Pr^{3+}]/([Pr^{3+}] + [Pr^{4+}])$ seems to be complicated by the overlapping of the marker peak for Pr^{4+} at 967 eV with the O KLL band. Therefore, in this study, the calculation based on Sinev et al. [98] is employed and expressed in the following equation.

$$\frac{[Pr^{3+}]}{[Pr^{3+}]+[Pr^{4+}]} = 1 - \frac{1}{0.28} \times \frac{area(Pr^{4+} marker\ at\ 947\ eV)}{area(3d_{5/2}cf^0)} \quad (3.16)$$

The corresponding peak areas, peak positions, and the ratio of $[Pr^{3+}]/([Pr^{3+}] + [Pr^{4+}])$ are summarised in Table 3.5.

Table 3. 5 Chemical states of Pr 3d in PSF0.1 and PSF0.3 oxides.

Peak	PSF0.1			PSF0.3		
	Area (a.u.)	Peak Position (eV)	$[Pr^{3+}]/([Pr^{3+}] + [Pr^{4+}])$	Area (a.u.)	Peak Position (eV)	$[Pr^{3+}]/([Pr^{3+}] + [Pr^{4+}])$
$3d_{5/2}$ – spin split doublets	915	928.02		2686	927.97	
$3d_{5/2}$ cf^0	2039	932.85	0.587	7207	932.87	0.457
$3d^9f^1$ for Pr^{4+} at low B.E.	236	946.18		1095	947.91	
$3d_{3/2}$ – spin split doublets	959	949.47		2082	950.44	
$3d_{3/2}$ cf^0	1014	953.03		3562	953.35	
$3d_{3/2}$ satellites	775	955.73		1434	956.19	
$3d^9f^1$ for Pr^{4+} at high B.E.	778	966.78		1001	967.01	

According to Table 3.5, the increased Pr concentration also reduces the ratio of $[Pr^{3+}]/([Pr^{3+}] + [Pr^{4+}])$ and it can be interpreted that the atomic fraction of Pr^{3+} ions decreases whereas that of Pr^{4+} increases. As a result, the presence of both Pr^{3+} and Pr^{4+} ions leads to the generation of electrons and the subsequent decrease in oxygen vacancy content [99]. The aforementioned assumption is also supported by the weight gain in

the thermograms of PSF0.1 and PSF0.3 or the decline in the oxygen non – stoichiometry as the Pr content rises. The corresponding defect reactions can be illustrated in equations 3.17, 3.18, and 3.19.

$$Pr_2O_3 \rightarrow 2Pr_{Sr}^{\cdot} + 3O_O^x + 2e' \quad (3.17)$$

$$PrO_2 \rightarrow 2Pr_{Sr}^{\cdot\cdot} + 2O_O^x + 2e' \quad (3.18)$$

$$\frac{1}{2}O_2(g) + 2e' + V_O^{\cdot\cdot} \rightarrow O_O^x \quad (3.19)$$

These responsible equation may be applied to the LSFx and SSFx oxides to account for the decreased oxygen non – stoichiometry as well.

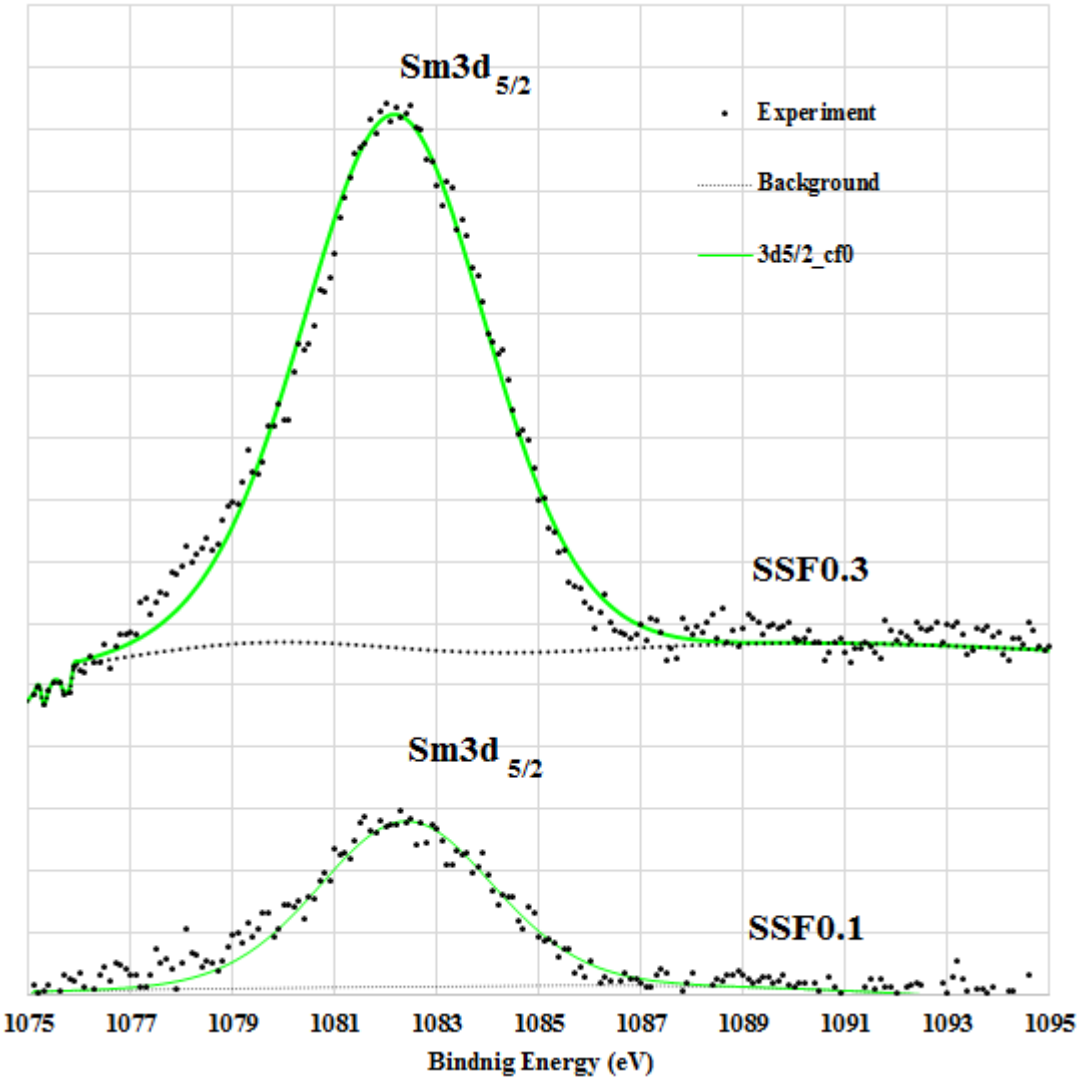

Figure 3. 42 Sm 3d core – level spectra of SSF0.1 and SSF0.3 oxides.

Similarly, the Sm 3d core – level spectra for SSF0.1 ad SSF0.3 oxides as shown in Figure 3.42 are also influenced by the spin – orbit splitting and it results in the presence of Sm $3d_{5/2}$ peak at around 1082 eV and Sm $3d_{3/2}$ peak at about 1100 eV (not shown here) [100-102]. With respect to the observation, these signature peaks belong to Sm^{3+} species and no other peaks which indicate the existence of Sm^{0} and Sm^{2+} are present. Therefore, it can be concluded that only Sm^{3+} ions uniquely dominate the speciation of Sm ions.

3.5.1.2 Iron spectra

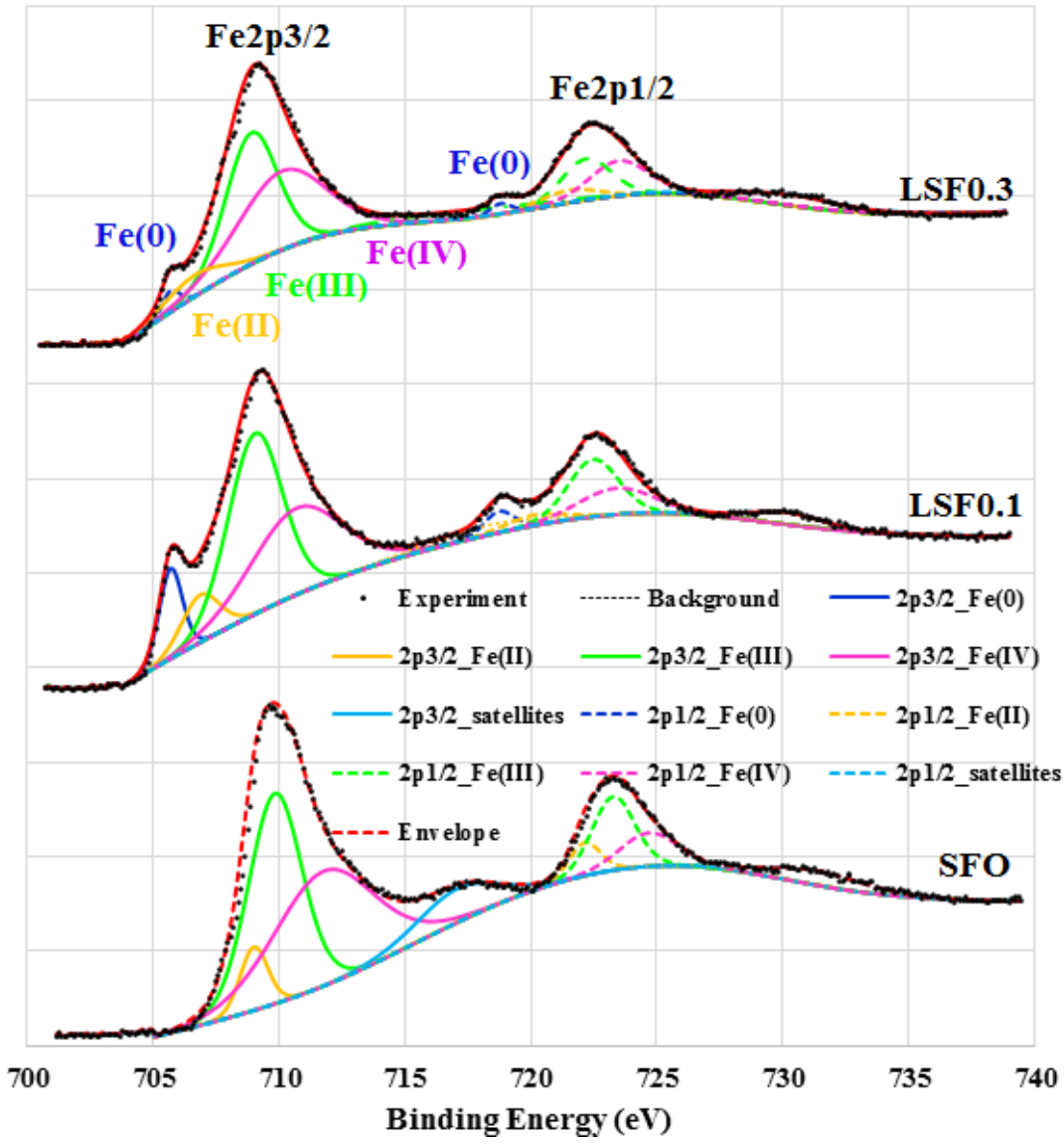

Figure 3. 43 Fe 2p core – level spectra of LSF0.1 and LSF0.3 oxides.

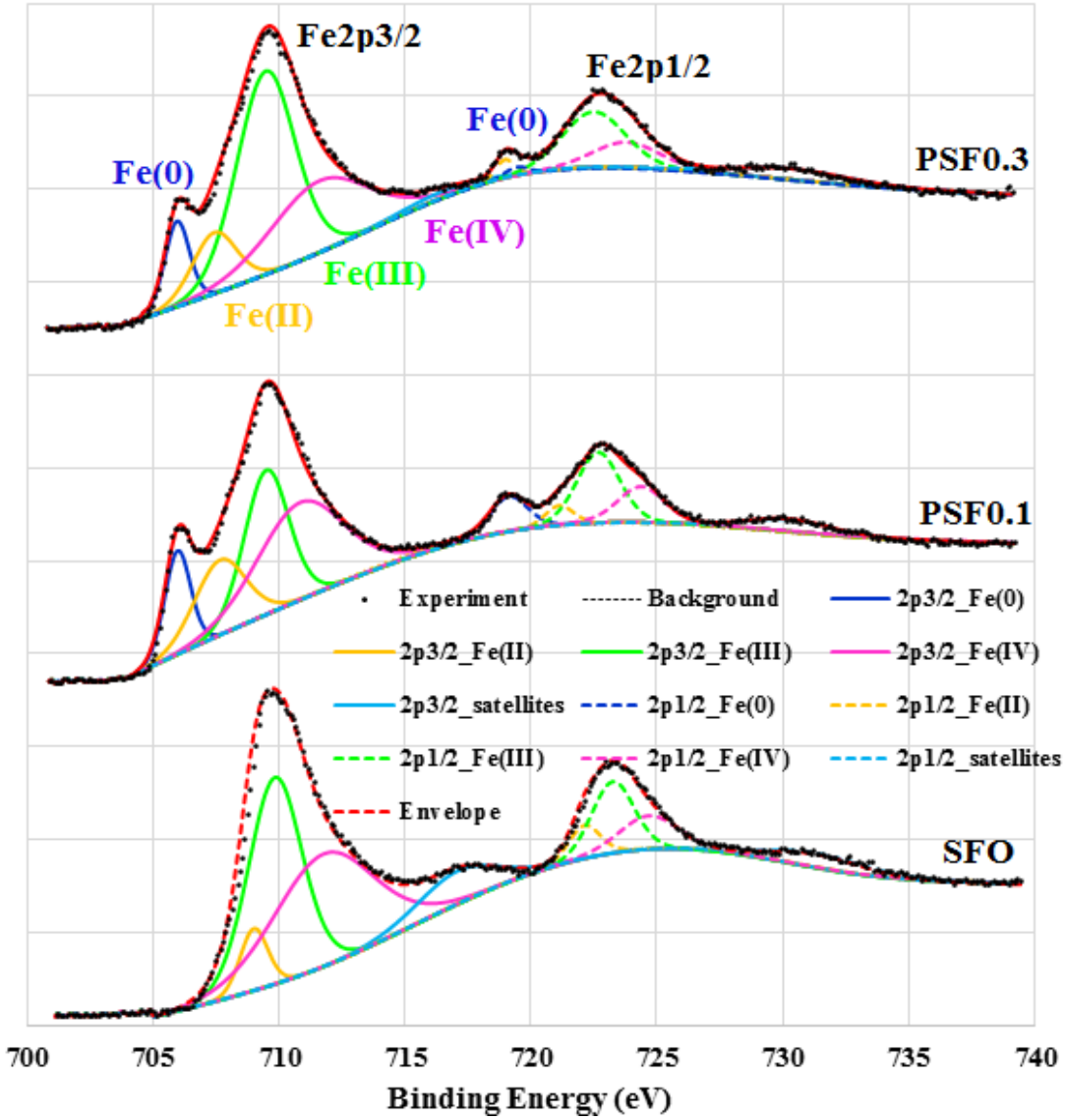

Figure 3. 44 Fe 2p core – level spectra of PSF0.1 and PSF0.3 oxides.

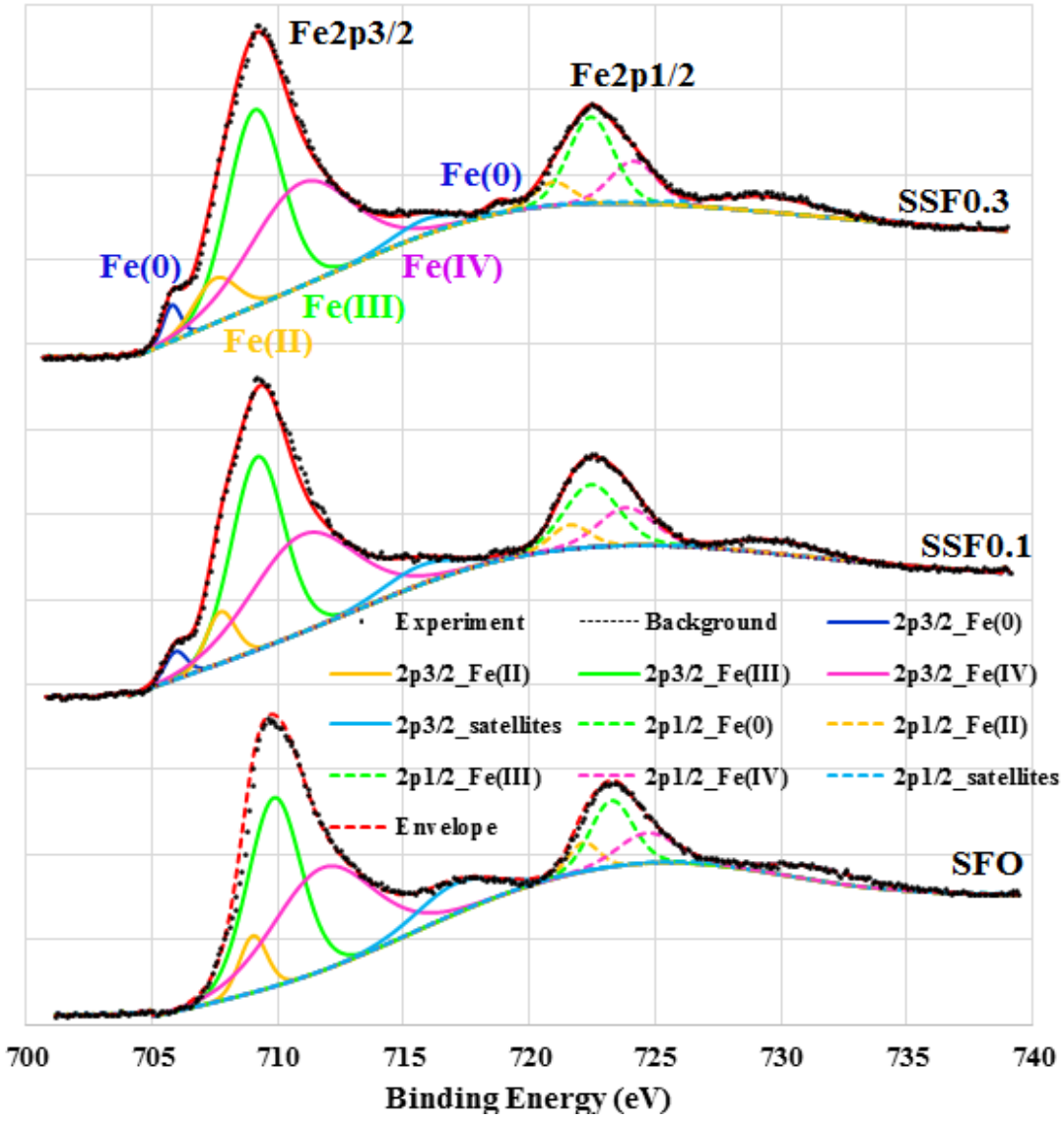

Figure 3. 45 Fe 2p core – level spectra of SSF0.1 and SSF0.3 oxides.

Table 3. 6 Summary of peak areas for each chemical state of Fe 2p in SFO, LSFx, PSFx, and SSFx oxides.

Peak Designation	SFO	LSFx oxides		PSFx oxides		SSFx oxides	
		LSF0.1	LSF0.3	PSF0.1	PSF0.3	SSF0.1	SSF0.3
$2p_{3/2}$_Fe(0)	0	2688	474	3490	2746	899	900
$2p_{3/2}$_Fe(II)	2225	2323	1612	5023	3461	2182	2717
$2p_{3/2}$_Fe(III)	14301	12545	8648	8329	15259	14412	15339
$2p_{3/2}$_Fe(IV)	14639	10004	8726	10868	9029	14357	14828
$2p_{3/2}$_satellites	3461	1421	1681	706	674	2052	1390
$2p_{1/2}$_Fe(0)	0	777	281	1716	433	151	372
$2p_{1/2}$_Fe(II)	1308	769	1042	731	286	1270	1285
$2p_{1/2}$_Fe(III)	3965	3715	2657	3921	4628	4721	5562
$2p_{1/2}$_Fe(IV)	2460	2666	2529	2076	2221	2870	2775
$2p_{1/2}$_satellites	1756	1131	1445	1347	1539	1657	2275

จุฬาลงกรณ์มหาวิทยาลัย
Chulalongkorn University

Table 3. 7 Percentage of iron chemical species in SFO, LSFx, PSFx, and SSFx oxides excluding satellites for calculation.

Oxidation State	SFO	LSFx oxides		PSFx oxides		SSFx oxides	
		LSF0.1	LSF0.3	PSF0.1	PSF0.3	SSF0.1	SSF0.3
Fe(0)	0.00	9.77	2.91	14.40	8.35	2.57	2.90
Fe(II)	9.08	8.71	10.22	15.91	9.84	8.45	9.14
Fe(III)	46.96	45.82	43.53	33.88	52.25	46.82	47.74
Fe(IV)	43.96	35.70	43.34	35.80	29.56	42.16	40.21

According to the Fe 2p XPS spectra for SFO, LSFx, PSFx, and SSFx oxides in Figures 4.43 – 4.45, they are deconvoluted into five main signals which originate from the 2p core – level excitation and pertain to the speciation of iron ions into Fe(0), Fe(II), Fe(III), and Fe(IV) and another satellite peak [103-106]. In addition, they also show the influence of the spin – orbit coupling which split the 2p core level into $2p_{3/2}$ and $2p_{1/2}$ and the respective peak positions for the oxidation states of Fe(0), Fe(II), Fe(III), and Fe(IV) within the $2p_{3/2}$ region are approximately 706, 707, 709, and 710 eV. However, Fe(0) species is absent in the undoped layered phase. Summaries of the related peak areas and the percentage speciation are summarised in Tables 3.6 and 3.7 respectively.

Upon increasing lanthanum and samarium concentration up to the composition of 0.1, they demonstrate a similar behaviour in which the percentage of Fe(III), which is integral to iron speciation in the layered phase, and Fe(0) remain roughly unchanged but that of Fe(IV) decreases sharply in LSFx oxides but slightly in SSFx oxides. On the contrary, the concentration of Fe(0) in LSFx and SSFx oxides rises moderately. These observations may be due to charge compensation effect in which the incorporation of lanthanide ions (La^{3+} and Sm^{3+}) imparts excessive positivity to the oxides. Consequently, more negatively – charged carriers are generated for charge balance, which are Fe(0) and Fe(II) in this instance. The same phenomenon also takes place in PSFx oxides but the concentrations of Fe(III) and Fe(IV) decline more sharply and those of Fe(0) and Fe(II) are raised more significantly due to the presence of both Pr^{3+} and Pr^{4+} ions.

Nevertheless, when the composition of the lanthanide ions reaches 0.3, in case of LSFx, the high percentages of Fe(III) and Fe(IV) are observed with an appreciable decline in Fe(0) concentration and a slight increase in Fe(II) percentage. This can be attributed to the effect of the perovskite phase in which the Fe(III) and Fe(IV) species in $SrFeO_3$ perovskite are preferred [107]. In relation to the relative percentage ratios of each chemical species, the Fe(IV)/Fe(II) ratio increases marginally while the Fe(0)/Fe(II) ratio drastically decreases at x = 0.3. Simultaneously, the oxygen non – stoichiometry of LSF0.3 drops as shown in Figure 3.19. For SSFx oxide, the relative concentration of each species is considered the same for both SSF0.1 and SSF0.3 oxides. This emphasises a less pronounced effect on the incorporation of Sm into the layered phase as reflected by the barely changed oxygen non – stoichiometry upon increasing Sm content. Likewise, the similar observation is also found in PSFx oxides but PSF0.3 shows a more a steep decrease in Fe(IV), Fe(0), and Fe(II) concentrations and the corresponding relative ratios of these ions with respect to Fe(III) decline. This observation evidently indicates the change in charge compensation mechanisms from the variation of the oxidation states of iron ions to the reduction in oxygen vacancy content.

To sum up, in spite of the formation of negatively – charged carriers by doping transition metals and the decrease in oxygen vacancy concentration, the electrical conductivities of all lanthanide – and transition metal - doped oxides still increase with increasing dopant contents. This clearly implies the importance of the synergistic effect of the perovskite phase and the layered phase.

3.5.2 $Sr_4 M_yFe_{6-y}O_{13}$ (M = Co, Ni)

3.5.2.1 Dopant spectra

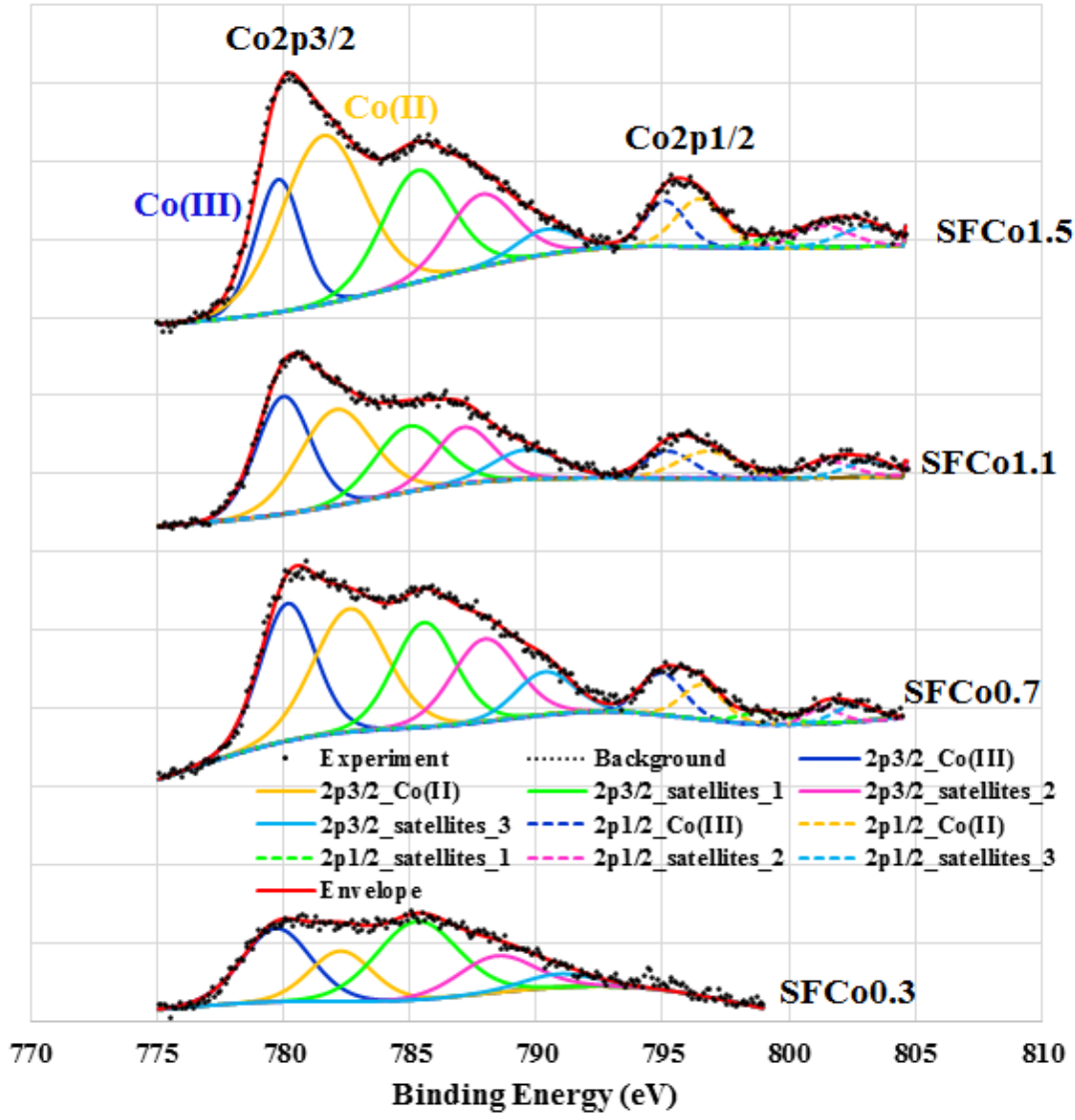

Figure 3. 46 Co 2p core – level spectra of SFCox oxides.

Table 3. 8 Summary of peak areas for each chemical state of Co 2p in SFCox oxides

Peak Designation	SFCox oxides			
.	SFCo0.3	SFCo0.7	SFCo1.1	SFCo1.5
$2p_{3/2}$_Co(III)	1925	2905	2450	2313
$2p_{3/2}$_Co(II)	1205	3422	2690	5337
$2p_{3/2}$_satellites_1	2447	2455	1714	3012
$2p_{3/2}$_ satellites_2	1062	2063	1269	1878
$2p_{3/2}$_satellites_3	371	948	763	567
$2p_{1/2}$_Co(III)	0	726	511	696
$2p_{1/2}$_Co(II)	0	531	642	895
$2p_{1/2}$_ satellites_1	0	210	60	140
$2p_{1/2}$_ satellites_2	0	212	304	471
$2p_{1/2}$_ satellites_3	0	259	318	414

จุฬาลงกรณ์มหาวิทยาลัย
Chulalongkorn University

Table 3. 9 Percentage of cobalt chemical species in SFCox oxides excluding satellites for calculation.

Oxidation State	SFCox oxides			
	SFCo0.3	SFCo0.7	SFCo1.1	SFCo1.5
Co(III)	61.51	47.88	47.06	32.56
Co(II)	38.49	52.12	52.94	67.44

With respect to the XPS spectra of Co 2p core level for SFCox oxides illustrated in Figure 3.46, the deconvolution of the spectra also displays the spin – orbit splitting of the Co 2p level into $2p_{3/2}$ and $2p_{1/2}$. Furthermore, within each sub – level, the spectra are further broken down into five peaks which consist of Co(III), Co(II) and three more

satellites [108-111] and their corresponding peak areas and oxidation states of cobalt ions are summarised in Tables 3.8 and 3.9 respectively. As the concentration of the Co dopant increases, the percentage of Co(II) increases while that of Co(III) decreases. As a consequence, this observation also confirms the presence of Co^{2+} and Co^{3+} in the system and supports the proposed defect reactions in equations 3.6 – 3.11 which explain the rise in the electrical conductivity and the oxygen non – stoichiometry with the increased Co concentration. Also, the increasing trend of Co^{2+} concentration correlates with the fact that Co^{2+} ions are preferred to be located in regular octahedral environment of the perovskite phase [112] and it is clearly confirmed by the rise in perovskite phase content of SFCox oxides.

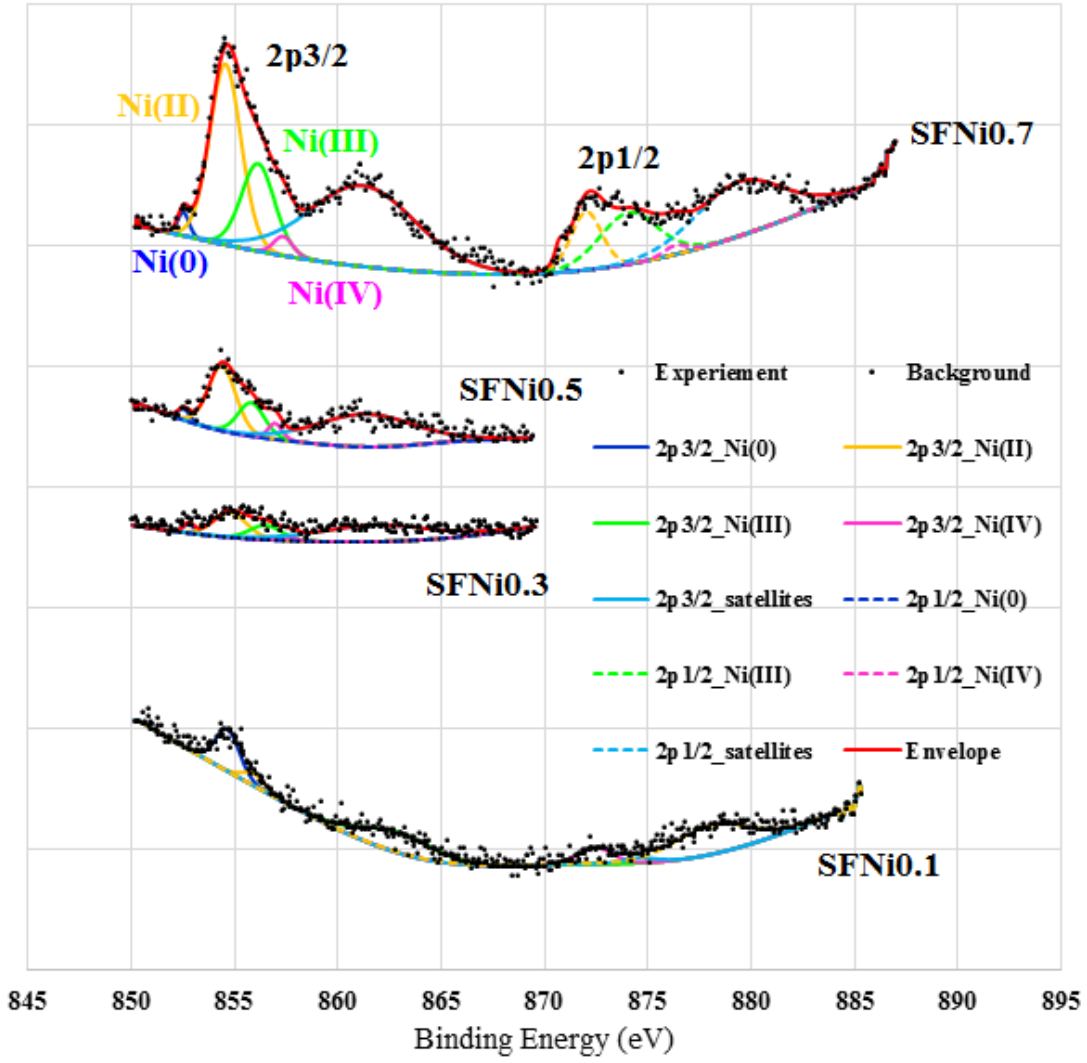

Figure 3. 47 Ni 2p core – level spectra of SFNix oxides.

Table 3. 10 Summary of peak areas for each chemical state of Ni 2p in SFNix oxides.

Peak Designation	SFNix oxides			
	SFNI0.1	SFNi0.3	SFNi0.5	SFNi0.7
$2p_{3/2}$_Ni(0)	0	30	40	79
$2p_{3/2}$_NI(II)	300	247	534	1687
$2p_{3/2}$_Ni(III)	82	137	264	870
$2p_{3/2}$_Ni(IV)	0	11	67	110
Satellites	445	559	948	2580
$2p_{1/2}$_Ni(0)	0	0	0	41
$2p_{1/2}$_NI(II)	171	0	0	537
$2p_{1/2}$_Ni(III)	54	0	0	895
$2p_{1/2}$_Ni(IV)	0	0	0	61
Satellites	0	0	0	1416

Table 3. 11 Percentage of nickel chemical species in SFNix oxides excluding satellites for calculation.

Oxidation State	SFNix oxides			
	SFNi.30.1	SFNi0.3	SFNi0.5	SFNi0.7
Ni(0)	0.00	6.95	4.40	2.80
Ni(II)	77.63	58.19	59.05	51.95
Ni(III)	22.37	32.21	29.20	41.25
Ni(IV)	0.00	2.65	7.36	4.00

According to the percentage composition of Ni species in SFNix oxides in Table 3.11 [113-116], only Ni(II) and Ni(III) ions are present in the pure layered phase of SFNi0.1 and Ni(II) ions are a major component. However, when increasing Ni concentration up to 0.7, the Ni(II) content appreciably drops and then remains essentially constant around 50 – 60% while Ni(III) concentration gradually increases. Moreover, negligible amounts of Ni(0) and Ni(IV) species are also found in which the Ni(0) content steadily falls but the Ni(IV) content fluctuates. The increase in Ni(III)

also correlates with the increase in electrical conductivity of SFNix oxides with the increased Ni content [117] due to the formation of redox couples of Ni^{2+}/Ni^{3+} and Fe^{3+}/Fe^{4+} as described by equation 3.20.

$$Ni'_{Fe} + Fe^{\cdot}_{Fe} \rightarrow Ni^{\times}_{Fe} + Fe^{\times}_{Fe} \tag{3.20}$$

where $Ni^{\times}_{Fe}$ and $Fe^{\times}_{Fe}$ represent Ni^{3+} and Fe^{3+} in the oxides. Furthermore, the increase in Ni(III) content possibly plays a major in charge compensation by electronic defects rather than ionic defect and it is reflected in the decrease in oxygen non – stoichiometry for SFNi0.5 oxide.

3.5.2.2 Iron spectra

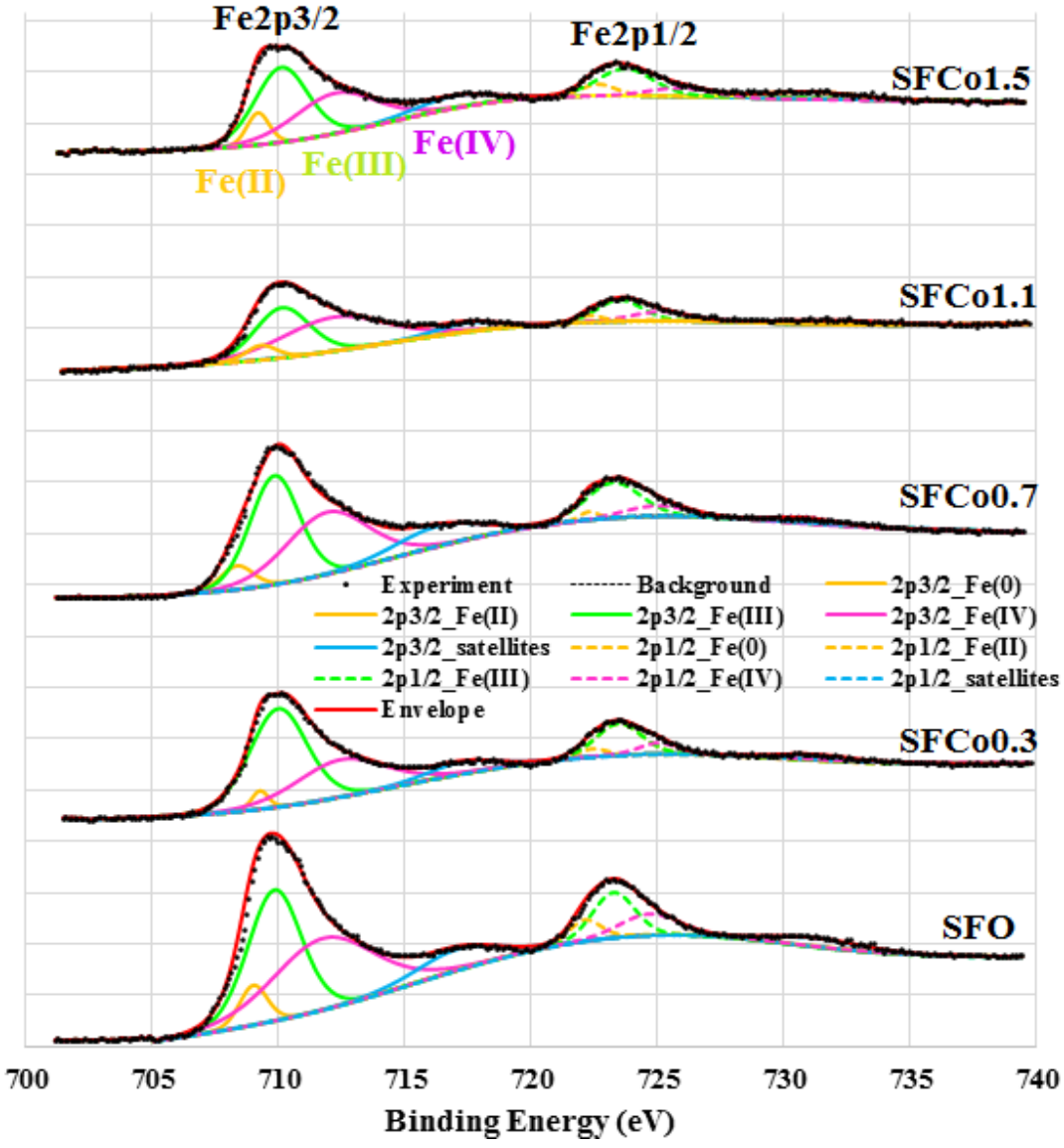

Figure 3. 48 Fe 2p core – level spectra of SFCox oxides.

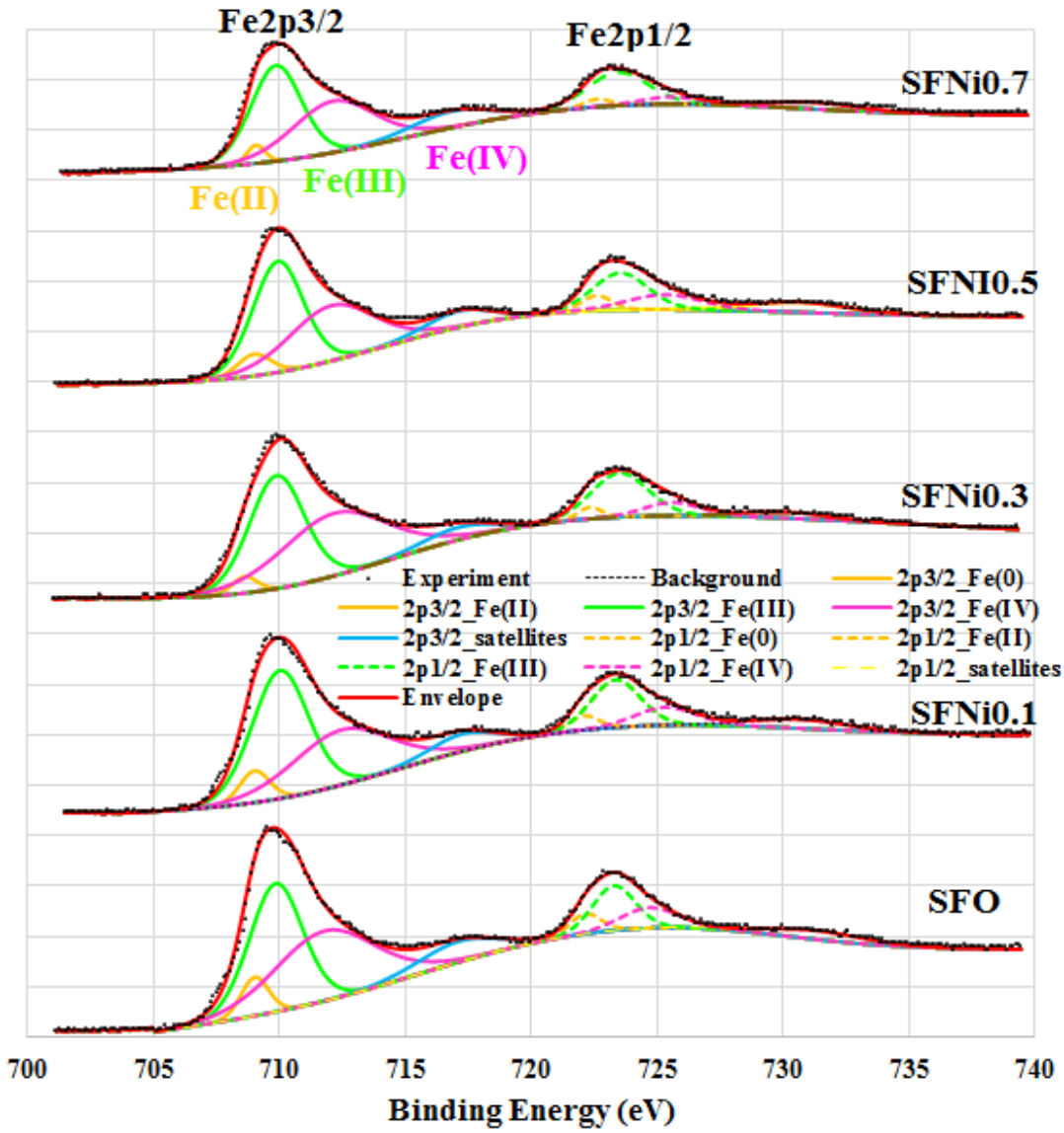

Figure 3. 49 Fe 2p core – level spectra of SFNix oxides.

Table 3. 12 Summary of peak areas for each chemical state of Fe 2p in SFO, SFCox, and SFNix oxides.

Peak Designation	SFO	SFCox oxides				SFNix oxides			
		SFCo 0.3	SFCo 0.7	SFCo 1.1	SFCo 1.5	SFNi 0.1	SFNi 0.3	SFNi 0.5	SFNi 0.7
$2p_{3/2}$_Fe(0)	0	0	0	0	0	0	0	0	0
$2p_{3/2}$_Fe(II)	2225	1259	1584	873	1466	1988	865	1514	692
$2p_{3/2}$_Fe(III)	14301	8359	11008	5512	8107	15123	13003	11741	10108
$2p_{3/2}$_Fe(IV)	14639	7648	10491	7169	6747	11294	13695	9886	8742
$2p_{3/2}$_satellites	3461	2131	3601	1153	1944	2394	1859	2209	2723
$2p_{1/2}$_Fe(0)	0	0	0	0	0	0	0	0	0
$2p_{1/2}$_Fe(II)	1308	534	284	285	803	885	589	956	446
$2p_{1/2}$_Fe(III)	3965	4525	3926	1893	2908	4899	5527	4216	4239
$2p_{1/2}$_Fe(IV)	2460	2188	1573	1016	1204	2280	1572	2308	872
$2p_{1/2}$_satellites	1756	2123	638	988	1323	1815	1053	2093	1241

จุฬาลงกรณ์มหาวิทยาลัย
Chulalongkorn University

Table 3. 13 Percentage of iron chemical species in SFO, SFCox, and SFNix oxides excluding satellites for calculation

Peak Designation	SFO	SFCox oxides				SFNix oxides			
		SFCo 0.3	SFCo 0.7	SFCo 1.1	SFCo 1.5	SFNi 0.1	SFNi 0.3	SFNi 0.5	SFNi 0.7
Fe(0)	0.00	0.00	0.00	0.00	0.00	0.00	0.00	0.00	0.00
Fe(II)	9.08	7.31	6.47	6.92	10.68	7.88	4.13	8.07	4.53
Fe(III)	46.96	52.56	51.74	44.21	51.87	54.90	52.57	52.11	57.16
Fe(IV)	43.96	40.13	41.79	48.87	37.44	37.22	43.31	39.82	38.31

Figures 3.48 and 3.49 represent the XPS spectra of Fe 2p core level for SFCox and SFNix oxides and the deconvolution of the spectra is also shown using the same procedure as those of the lanthanide – containing oxides. Summaries of peaks areas and the percentage composition of each chemical species for SFCox and SFNix oxides are provided in Tables 3.12 and 3.13 respectively.

In case of SFCox oxides, upon raising Co concentration, the percentage of Fe(II) gradually decreases but the concentration of Fe(IV) increases. The opposite trend of the Fe(II) and Fe(IV) concentrations can be attributed to the effect of charge compensation by doping cobalt. In relation to the speciation of cobalt, the increasing Co^{2+} content results in the relative negative charge of Co^{2+} with respect to the original Fe^{3+} as described in equation 3.7. Therefore, more positively – charged carriers are produced, which are Fe(IV) ions and possibly oxygen vacancies. However, at the composition of 1.5, the concentration of Fe(II) slightly increases whereas that of Fe(IV) decreases moderately. The increase in Fe(II) content and the decrease in Fe(IV) content, therefore, result in the reduction in positively – charged carriers and then the electrical conductivity and the polarisation resistance of SFCo1.5 oxide.

For SFNix oxides, upon increasing Ni content, the concentrations of Fe(III) and Fe(IV) are kept relatively constant whereas that of Fe(II) varies wildly. This observation means that the incorporation of either Ni(II) or Ni(III) ions into the oxides does not much affect the speciation of Fe ions. In addition, at low concentration of Ni dopant at which the concentration of Ni(III) ions is considered low, the formation of oxygen vacancies contributes more to charge compensation effect as shown in the comparable amount of oxygen vacancies for SFNi0.1 and SFNi0.3 oxides.

CHAPTER IV
CONCLUSIONS

The layered oxides including (i) $Sr_4Fe_6O_{13}$ (SFO) (ii) $La_xSr_{4-x}Fe_6O_{13}$ (LSFx, x = 0.0 -0.4) (iii) $Pr_xSr_{4-x}Fe_6O_{13}$ (PSFx, x = 0.0 – 0.4) (iv) $Sm_xSr_{4-x}Fe_6O_{13}$ (SSFx, x = 0.0 – 0.4) (iv) $Sr_4Co_xFe_{6-x}O_{13}$ (SFCox, x = 0.0 – 1.7) and (v) $Sr_4Ni_xFe_{6-x}O_{13}$ (SFNix, x = 0.0 – 1.1) were synthesised via conventional solid – state reaction method with the respective calcination and sintering temperatures of 850°C for 16 hours and 1185°C for 5 hours. Several characterisation techniques were performed for structural determination, oxygen non – stoichiometry, chemical speciation, electrical conductivity and electrochemical property for oxygen reduction reaction.

All layered oxides demonstrate a gradual phase transformation from the pure layered phase to the perovskite phase and the negligible magnetoplumbite phase as the concentrations of both lanthanide and transition metal ions increase. The transformation arises from the destabilisation of the layered structure that is caused by aliovalent doping and it is governed by the phase equilibrium relationship between the previously mentioned phases. In general, all oxide materials illustrate the increase in the electrical conductivity with the rise in dopant contents but only PSFx, SSFx, and SFCox oxides show semiconducting behaviors over the entire experimental conditions, which is dictated by small – polaron hopping mechanism. The electrical conductivity is raised due to the increasing perovskite content that serves as a three – dimensional network for the facilitation of electron transport. Conversely, LSFx and SFNix oxides exhibit the transition in electrical conduction from semiconduction to metallic – like mechanism and the change in electrical conductivity behavior is largely explained by the combined effect of charge redistribution within the structure when the layered phase is still present and the loss of lattice oxygen when the perovskite phase predominates. Among the oxides prepared, the average range of electrical conductivity of the multiphase oxides fall in the interval of 5 – 20 S cm^{-1}.

In addition, the polarization resistance that accounts for the oxygen reduction reaction decreases for all oxides as the concentration of dopants is raised. The reduction in the polarization resistance results from the interplay of the existing phases in which the layered phase is embedded in the continuous network of the perovskite phase and the former phase acts as the fast oxide ion diffusion channels. Similarly, the average polarisation resistance of the multiphase oxides covers the values from approximately 2 to 10 Ω cm^2. However, a few oxides with particular compositions do not follow the decreasing trend in polarisation resistance and the disorder is probably attributed to the change in microstructural features of the oxides which adversely affect molecular oxygen diffusion. In relation to that, thermogravimetric analyses also unravel the

contradictory trend in oxygen non – stoichiometry in which the oxygen non – stoichiometry tends to decline with additional dopant concentration for most of the oxides. The decrease is presumably caused by the effect of dopant segregation and related oxygen vacancy trapping at grain boundaries.

In case of chemical speciation of the oxide samples, XPS analyses reveal the different charge compensation mechanisms. For lanthanide – containing oxides, excessive positive charge induced by incorporating the lanthanide ions is balanced by the conversion of Fe(III) and Fe(IV) into Fe(0) and Fe(II). In contrast, the excess of negative charge is compensated by increasing Fe(IV) content and reducing Fe(II) concentration for transition metal – doped oxides.

To sum up, PSFx and SFCox oxides which show relatively low polarisation resistances and exhibit moderate electrical conductivities in the multiphase region should be further tested for fuel cell performance accompanied with long – term stability test as promising cathodes for IT – SOFCs.

จุฬาลงกรณ์มหาวิทยาลัย
Chulalongkorn University

REFERENCES

[1] Karakoussis, V., Brandon, N.P., Leach, M., and van der Vorst, R. The environmental impact of manufacturing planar and tubular solid oxide fuel cells. Journal of Power Sources 101(1) (2001): 10-26.

[2] Acres, G.J.K. Recent advances in fuel cell technology and its applications. Journal of Power Sources 100(1–2) (2001): 60-66.

[3] Smith, W. The role of fuel cells in energy storage. Journal of Power Sources 86(1–2) (2000): 74-83.

[4] Stambouli, A.B. and Traversa, E. Solid oxide fuel cells (SOFCs): a review of an environmentally clean and efficient source of energy. Renewable and Sustainable Energy Reviews 6(5) (2002): 433-455.

[5] Kendall, K. 1 - Introduction to SOFCs. in High-Temperature Solid Oxide Fuel Cells for the 21st Century (Second Edition), pp. 1-24. Boston: Academic Press, 2016.

[6] Kendall, K. 2 - History. in High-Temperature Solid Oxide Fuel Cells for the 21st Century (Second Edition), pp. 25-50. Boston: Academic Press, 2016.

[7] Minh, N.Q. 8 - Cell and stack design, fabrication and performance A2 - Kendall, Kevin. in Kendall, M. (ed.)High-Temperature Solid Oxide Fuel Cells for the 21st Century (Second Edition), pp. 255-282. Boston: Academic Press, 2016.

[8] Minh, N.Q. 9 - System designs and applications A2 - Kendall, Kevin. in Kendall, M. (ed.)High-Temperature Solid Oxide Fuel Cells for the 21st Century (Second Edition), pp. 283-327. Boston: Academic Press, 2016.

[9] Kendall, K. 10 - Portable early market SOFCs. in High-Temperature Solid Oxide Fuel Cells for the 21st Century (Second Edition), pp. 329-356. Boston: Academic Press, 2016.

[10] Sui, S. and Xiu, G.H. 14 - Fuels and fuel processing in SOFC applications A2 - Kendall, Kevin. in Kendall, M. (ed.)High-Temperature Solid Oxide Fuel Cells for the 21st Century (Second Edition), pp. 461-495. Boston: Academic Press, 2016.

[11] Ryan O'Hare, S.-W.C., Whitney Colella, Fritz B Prinz. Fuel Cell Fundamentals (2006).

[12] Raghvendra, Singh, R.K., and Singh, P. Electrical conductivity of barium substituted LSGM electrolyte materials for IT-SOFC. Solid State Ionics 262 (2014): 428-432.

[13] Khan, M.S., Lee, S.-B., Song, R.-H., Lee, J.-W., Lim, T.-H., and Park, S.-J. Fundamental mechanisms involved in the degradation of nickel–yttria stabilized zirconia (Ni–YSZ) anode during solid oxide fuel cells operation: A review. Ceramics International 42(1, Part A) (2016): 35-48.

[14] Curi, M.O., Ferraz, H.C., Furtado, J.G.M., and Secchi, A.R. Dispersant effects on YSZ electrolyte characteristics for solid oxide fuel cells. Ceramics International 41(5, Part A) (2015): 6141-6148.

[15] Shri Prakash, B., Senthil Kumar, S., and Aruna, S.T. Properties and development of Ni/YSZ as an anode material in solid oxide fuel cell: A review. Renewable and Sustainable Energy Reviews 36 (2014): 149-179.

[16] Kim, J., Park, Y., Sung, D.J., Moon, S., Lee, K.B., and Hong, S.-I. Preparation of thin film YSZ electrolyte by using electrostatic spray deposition. International Journal of Refractory Metals and Hard Materials 27(6) (2009): 985-990.
[17] Lee, K.-R., Ahn, K., Chung, Y.-C., Lee, J.-H., and Yoo, H.-I. Lattice distortion effect on electrical properties of GDC thin films: Experimental evidence and computational simulation. Solid State Ionics 229 (2012): 45-53.
[18] Izuki, M., et al. Interfacial stability and cation diffusion across the LSCF/GDC interface. Journal of Power Sources 196(17) (2011): 7232-7236.
[19] Kwon, T.-H., Lee, T., and Yoo, H.-I. Partial electronic conductivity and electrolytic domain of bilayer electrolyte Zr0.84Y0.16O1.92/Ce0.9Gd0.1O1.95. Solid State Ionics 195(1) (2011): 25-35.
[20] Morales, M., Roa, J.J., Tartaj, J., and Segarra, M. A review of doped lanthanum gallates as electrolytes for intermediate temperature solid oxides fuel cells: From materials processing to electrical and thermo-mechanical properties. Journal of the European Ceramic Society 36(1) (2016): 1-16.
[21] Kharton, V.V., Marques, F.M.B., and Atkinson, A. Transport properties of solid oxide electrolyte ceramics: a brief review. Solid State Ionics 174(1–4) (2004): 135-149.
[22] Borodianska, H., Badica, P., Uchikoshi, T., Sakka, Y., and Vasylkiv, O. Nanometric La0.9Sr0.1Ga0.8Mg0.2O3−x ceramic prepared by low-pressure reactive spark-plasma-sintering. Journal of Alloys and Compounds 509(5) (2011): 2535-2539.
[23] Preux, N., Rolle, A., and Vannier, R.N. 12 - Electrolytes and ion conductors for solid oxide fuel cells (SOFCs). in Functional Materials for Sustainable Energy Applications, pp. 370-401: Woodhead Publishing, 2012.
[24] Laukaitis, G., Dudonis, J., Orliukas, A.F., and Milcius, D. Properties of YSZ thin films deposited by e-beam technique. Solid State Ionics 179(1–6) (2008): 182-187.
[25] Sandoval, M.V., et al. Barium-modified NiO–YSZ/NiO–GDC cermet as new anode material for solid oxide fuel cells (SOFC). Solid State Ionics 261 (2014): 36-44.
[26] Wang, Z., Tian, Y., and Li, Y. Direct CH4 fuel cell using Sr2FeMoO6 as an anode material. Journal of Power Sources 196(15) (2011): 6104-6109.
[27] Cassidy, M., Connor, P.A., Irvine, J.T.S., and Savaniu, C.D. 5 - Anodes A2 - Kendall, Kevin. in Kendall, M. (ed.)High-Temperature Solid Oxide Fuel Cells for the 21st Century (Second Edition), pp. 133-160. Boston: Academic Press, 2016.
[28] Li, X., Zhang, H., Huang, J., Lu, J., and Feng, Z. Fast sintering GDC coated Ni powders synthesized by modified heterogeneous precipitation method. Journal of Alloys and Compounds 693 (2017): 882-886.
[29] Liu, L., et al. A novel doped CeO2–LaFeO3 composite oxide as both anode and cathode for solid oxide fuel cells. International Journal of Hydrogen Energy 37(17) (2012): 12574-12579.

[30] Sammes, N.M. and Hatchwell, C.E. Optimization of slip-cast La0.8Sr0.2CrO3 perovskite material for use as an interconnect in SOFC applications. Materials Letters 32(5) (1997): 339-345.
[31] Shaikh, S.P.S., Muchtar, A., and Somalu, M.R. A review on the selection of anode materials for solid-oxide fuel cells. Renewable and Sustainable Energy Reviews 51 (2015): 1-8.
[32] Kawada, T. and Horita, T. 6 - Cathodes A2 - Kendall, Kevin. in Kendall, M. (ed.)High-Temperature Solid Oxide Fuel Cells for the 21st Century (Second Edition), pp. 161-193. Boston: Academic Press, 2016.
[33] Nielsen, J., Jacobsen, T., and Wandel, M. Impedance of porous IT-SOFC LSCF:CGO composite cathodes. Electrochimica Acta 56(23) (2011): 7963-7974.
[34] Nielsen, J. and Hjelm, J. Impedance of SOFC electrodes: A review and a comprehensive case study on the impedance of LSM:YSZ cathodes. Electrochimica Acta 115 (2014): 31-45.
[35] Baharuddin, N.A., Muchtar, A., and Somalu, M.R. Short review on cobalt-free cathodes for solid oxide fuel cells. International Journal of Hydrogen Energy.
[36] Nielsen, J. and Mogensen, M. SOFC LSM:YSZ cathode degradation induced by moisture: An impedance spectroscopy study. Solid State Ionics 189(1) (2011): 74-81.
[37] Richter, J., Holtappels, P., Graule, T., Nakamura, T., and Gauckler, L.J. Materials design for perovskite SOFC cathodes. Monatshefte für Chemie - Chemical Monthly 140(9) (2009): 985-999.
[38] Pornprasertsuk, R., Cheng, J., Huang, H., and Prinz, F.B. Electrochemical impedance analysis of solid oxide fuel cell electrolyte using kinetic Monte Carlo technique. Solid State Ionics 178(3–4) (2007): 195-205.
[39] Kanamaru, F., Shimada, M., and Koizumi, M. Crystallographic properties of and mössbauer effect in Sr4Fe6O13. Journal of Physics and Chemistry of Solids 33(5) (1972): 1169-1171.
[40] Patrakeev, M.V., Mitberg, E.B., Leonidov, I.A., and Kozhevnikov, V.L. Electrical characterization of the intergrowth ferrite Sr4Fe6O13+δ. Solid State Ionics 139(3–4) (2001): 325-330.
[41] Deng, Z.-q., Zhang, G.-g., Liu, W., Peng, D.-k., and Chen, C.-s. Phase composition, oxidation state and electrical conductivity of SrFe1.5−xCoxOy. Solid State Ionics 152–153 (2002): 735-739.
[42] Fossdal, A., et al. Phase equilibria and microstructure in Sr4Fe6−xCoxO13 0≤x≤4 mixed conductors. Solid State Ionics 143(3–4) (2001): 367-377.
[43] Fossdal, A., Einarsrud, M.-A., and Grande, T. Phase equilibria in the pseudo-binary system SrO–Fe2O3. Journal of Solid State Chemistry 177(8) (2004): 2933-2942.
[44] Bredesen, R., Norby, T., Bardal, A., and Lynum, V. Phase relations, chemical diffusion and electrical conductivity in pure and doped Sr4Fe6O13 mixed conductor materials. Solid State Ionics 135(1–4) (2000): 687-697.
[45] Waerenborgh, J.C., Avdeev, M., Patrakeev, M.V., Kharton, V.V., and Frade, J.R. Redox behaviour of Sr4Fe6O13±δ by Mössbauer spectroscopy and neutron diffraction. Materials Letters 57(21) (2003): 3245-3250.

[46] Guggilla, S., Armstrong, T., and Manthiram, A. Synthesis, Crystal Chemistry, and Electrical Properties of the Intergrowth Oxides Sr4−xCaxFe6−yCoyO13+δ. Journal of Solid State Chemistry 145(1) (1999): 260-266.

[47] Tsuchida, T. and Kan, T. TG-DTA study of mixed conductor Sr4(Fe1−xCox)6O13±δ in air and argon. Journal of the European Ceramic Society 21(4) (2001): 555-560.

[48] Fadaei, M. and Mohammadi, R. A comprehensive simulation of gas concentration impedance for solid oxide fuel cell anodes. Energy Conversion and Management 106 (2015): 93-100.

[49] Nechache, A., et al. Diagnosis of a cathode-supported solid oxide electrolysis cell by electrochemical impedance spectroscopy. Electrochimica Acta 210 (2016): 596-605.

[50] Subotić, V., et al. In-situ electrochemical characterization methods for industrial-sized planar solid oxide fuel cells Part I: Methodology, qualification and detection of carbon deposition. Electrochimica Acta 207 (2016): 224-236.

[51] Bertei, A., Arcolini, G., Ouweltjes, J.P., Wuillemin, Z., Piccardo, P., and Nicolella, C. PHYSICALLY-BASED DECONVOLUTION OF IMPEDANCE SPECTRA: INTERPRETATION, FITTING AND VALIDATION OF A NUMERICAL MODEL FOR LANTHANUM STRONTIUM COBALT FERRITE-BASED SOLID OXIDE FUEL CELLS. Electrochimica Acta 208 (2016): 129-141.

[52] Huang, Q.-A., Hui, R., Wang, B., and Zhang, J. A review of AC impedance modeling and validation in SOFC diagnosis. Electrochimica Acta 52(28) (2007): 8144-8164.

[53] Chen, D., Wang, F., Shi, H., Ran, R., and Shao, Z. Systematic evaluation of Co-free LnBaFe2O5+δ (Ln = Lanthanides or Y) oxides towards the application as cathodes for intermediate-temperature solid oxide fuel cells. Electrochimica Acta 78 (2012): 466-474.

[54] Jin, F., Xu, H., Long, W., Shen, Y., and He, T. Characterization and evaluation of double perovskites LnBaCoFeO5+δ (Ln = Pr and Nd) as intermediate-temperature solid oxide fuel cell cathodes. Journal of Power Sources 243 (2013): 10-18.

[55] Bardal, A. and Bredesen, R. On the nano-size intergrowth of Sr4Fe6O13±δ and (Sr1−xLax)FeO3−δ phases in the mixed conductor Sr3.6La0.4Fe6Oz. Journal of Materials Science 36(22) (2001): 5357-5367.

[56] Bredesen, R. and Norby, T. On phase relations, transport properties and defect structure in mixed conducting SrFe1.5−xCoxOz. Solid State Ionics 129(1–4) (2000): 285-297.

[57] Jiang, S., Sunarso, J., Zhou, W., and Shao, Z. The significant effect of the phase composition on the oxygen reduction reaction activity of a layered oxide cathode. Journal of Materials Chemistry A 1(36) (2013): 11026-11032.

[58] Inoishi, A., Sakai, T., Ju, Y.-W., Ida, S., and Ishihara, T. Effect of Ni/Fe ratio on the performance and stability of the Fe-air rechargeable battery using a La0.9Sr0.1Ga0.8Mg0.2O3 electrolyte. International Journal of Hydrogen Energy 39(36) (2014): 21352-21357.

[59] H., S.B. Development of Solid Oxide Fuel Cell Electrodes with High Conductivity and Enhanced Redox Stability. (2010).
[60] Pérez, O., Mellenne, B., Retoux, R., Raveau, B., and Hervieu, M. A new light on the iron coordination in Sr4Fe6O13±δ: Super space formalism and structural mechanism. Solid State Sciences 8(5) (2006): 431-443.
[61] Shannon, R.D. Revised Effective Ionic Radii and Systematic Studies of Interatomic Distances in Halides and Chalcogenides. Acta Crystallographica A 32 (1976): 17.
[62] Yoshiasa, A., Ueno, K., Kanamaru, F., and Horiuchi, H. Structure of Sr4Fe6O13, a new perovskite-derivative in the Sr□Fe□O system. Materials Research Bulletin 21(2) (1986): 175-181.
[63] Fisher, C.A.J. and Islam, M.S. Mixed ionic/electronic conductors Sr2Fe2O5 and Sr4Fe6O13: atomic-scale studies of defects and ion migration. Journal of Materials Chemistry 15(31) (2005): 3200-3207.
[64] Fjellvag, H., C. Hauback, B., and Bredesen, R. Crystal structure of the mixed conductor Sr4Fe4Co2O13. Journal of Materials Chemistry 7(12) (1997): 2415-2419.
[65] Stølen, S., Mohn, C.E., Ravindran, P., and Allan, N.L. Topography of the Potential Energy Hypersurface and Criteria for Fast-Ion Conduction in Perovskite-Related A2B2O5 Oxides. The Journal of Physical Chemistry B 109(25) (2005): 12362-12365.
[66] Vidal, K., et al. Isolating the effect of doping in the structure and conductivity of (Ln1−xMx)FeO3−δ perovskites. Solid State Ionics 178(21–22) (2007): 1310-1316.
[67] Ren, Y., Küngas, R., Gorte, R.J., and Deng, C. The effect of A-site cation (Ln = La, Pr, Sm) on the crystal structure, conductivity and oxygen reduction properties of Sr-doped ferrite perovskites. Solid State Ionics 212 (2012): 47-54.
[68] Patrakeev, M.V., Leonidov, I.A., Kozhevnikov, V.L., and Kharton, V.V. Ion–electron transport in strontium ferrites: relationships with structural features and stability. Solid State Sciences 6(9) (2004): 907-913.
[69] Jiang, S., Zhou, W., Sunarso, J., Ran, R., and Shao, Z. A cobalt-free layered oxide as an oxygen reduction catalyst for intermediate-temperature solid oxide fuel cells. International Journal of Hydrogen Energy 40(45) (2015): 15578-15584.
[70] Tai, L.W., Nasrallah, M.M., Anderson, H.U., Sparlin, D.M., and Sehlin, S.R. Structure and electrical properties of La1 − xSrxCo1 − yFeyO3. Part 2. The system La1 − xSrxCo0.2Fe0.8O3. Solid State Ionics 76(3) (1995): 273-283.
[71] Tai, L.W., Nasrallah, M.M., Anderson, H.U., Sparlin, D.M., and Sehlin, S.R. Structure and electrical properties of La1−xSrxCo1−yFeyO3. Part 1. The system La0.8Sr0.2Co1−yFeyO3. Solid State Ionics 76(3) (1995): 259-271.
[72] Kim, K.H., Yoon, K.H., and Choi, J.S. Electrical conductivity and defect structure of Ni-doped and "CO-reduced" Ni-doped SrTiO3 single crystals. Journal of Physics and Chemistry of Solids 46(9) (1985): 1061-1066.
[73] Abe, S., Iwasaki, S., Shimonishi, Y., Komine, S., and Munakata, F. Effect of Ni and Ti substitutions on Li1.05Mn2O4-δ electrical conductivities at high temperature. Solid State Communications 244 (2016): 64-67.

[74] Li, S., Tu, H., Li, F., Anwar, M.T., and Yu, L. Investigation of Nd2Ni0.9M0.1O4+δ (M = Ni, Co, Cu, Fe, and Mn) cathodes for intermediate-temperature solid oxide fuel cell. Journal of Alloys and Compounds 694 (2017): 17-23.

[75] Lee, K.T. and Manthiram, A. Effect of cation doping on the physical properties and electrochemical performance of Nd0.6Sr0.4Co0.8M0.2O3−δ (M = Ti, Cr, Mn, Fe, Co, and Cu) cathodes. Solid State Ionics 178(13–14) (2007): 995-1000.

[76] Jin, W., Abothu, I.R., Wang, R., and Chung, T.-S. Sol−Gel Synthesis and Characterization of SrFeCo0.5O3.25-δ Powder. Industrial & Engineering Chemistry Research 41(22) (2002): 5432-5435.

[77] Lankhorst, M.H.R. and ten Elshof, J.E. Thermodynamic Quantities and Defect Structure of La0.6Sr0.4Co1−yFeyO3−δ(y=0–0.6) from High-Temperature Coulometric Titration Experiments. Journal of Solid State Chemistry 130(2) (1997): 302-310.

[78] Petrov, A.N., Cherepanov, V.A., Kononchuk, O.F., and Gavrilova, L.Y. Oxygen nonstoichiometry of La1−xSrxCoO3−δ (0 < x ≤ 0.6). Journal of Solid State Chemistry 87(1) (1990): 69-76.

[79] Zhao, H., Shen, W., Zhu, Z., Li, X., and Wang, Z. Preparation and properties of BaxSr1−xCoyFe1−yO3−δ cathode material for intermediate temperature solid oxide fuel cells. Journal of Power Sources 182(2) (2008): 503-509.

[80] Chroneos, A., Yildiz, B., Tarancon, A., Parfitt, D., and Kilner, J.A. Oxygen diffusion in solid oxide fuel cell cathode and electrolyte materials: mechanistic insights from atomistic simulations. Energy & Environmental Science 4(8) (2011): 2774-2789.

[81] Kwon, H., Lee, W., and Han, J.W. Suppressing cation segregation on lanthanum-based perovskite oxides to enhance the stability of solid oxide fuel cell cathodes. RSC Advances 6(74) (2016): 69782-69789.

[82] Wilkes, M.F., Hayden, P., and Bhattacharya, A.K. Surface segregation of lanthanum and cerium ions in ceria/lanthana solid solutions: comparison between experimental results and a statistical–mechanical model. Applied Surface Science 206(1–4) (2003): 12-19.

[83] Yang, H., Lee, H.S., Kotula, P.G., Sato, Y., Ikuhara, Y., and Browning, N.D. Amphoteric doping of praseodymium Pr3+ in SrTiO3 grain boundaries. Applied Physics Letters 106(12) (2015): 121904.

[84] Liu, B., Cooper, V.R., Zhang, Y., and Weber, W.J. Segregation and trapping of oxygen vacancies near the SrTiO3 Σ3 (1 1 2) tilt grain boundary. Acta Materialia 90 (2015): 394-399.

[85] Yuan, F., Liu, B., Zhang, Y., and Weber, W.J. Segregation and Migration of the Oxygen Vacancies in the Σ3 (111) Tilt Grain Boundaries of Ceria. The Journal of Physical Chemistry C 120(12) (2016): 6625-6632.

[86] Adler, S.B. Mechanism and kinetics of oxygen reduction on porous La1−xSrxCoO3−δ electrodes. Solid State Ionics 111(1–2) (1998): 125-134.

[87] Adler, S.B. Factors Governing Oxygen Reduction in Solid Oxide Fuel Cell Cathodes. Chemical Reviews 104(10) (2004): 4791-4844.

[88] Adler, S.B., Chen, X.Y., and Wilson, J.R. Mechanisms and rate laws for oxygen exchange on mixed-conducting oxide surfaces. Journal of Catalysis 245(1) (2007): 91-109.
[89] Hjalmarsson, P., Søgaard, M., and Mogensen, M. Electrochemical behaviour of (La1 − xSrx)sCo1 − yNiyO3 − δ as porous SOFC cathodes. Solid State Ionics 180(26–27) (2009): 1395-1405.
[90] Kulkarni, A.P., Giddey, S., and Badwal, S.P.S. Enhancing Oxygen Reduction Reactions in Solid Oxide Fuel Cells with Ultrathin Nanofilm Electrode–Electrolyte Interfacial Layers. The Journal of Physical Chemistry C 120(29) (2016): 15675-15683.
[91] Virkar, A.V. Chemical and Microstructural Effects in Electrode Polarization. SECA Core and Technology Workshop, Tampa, Florida (2005): 37.
[92] Ryu, J., O'Hayre, R., and Lee, H. Polarization resistance and composite cathode of Ce doped SrMnO3 system for intermediate temperature solid oxide fuel cells. Solid State Ionics 260 (2014): 60-64.
[93] Wang, X.-M., Li, C.-X., Li, C.-J., and Yang, G.-J. Microstructure and polarization of La0.8Sr0.2MnO3 cathode deposited by alcohol solution precursor plasma spraying. International Journal of Hydrogen Energy 37(17) (2012): 12879-12885.
[94] Oliveira, R.C., Hammer, P., Guibal, E., Taulemesse, J.-M., and Garcia Jr, O. Characterization of metal–biomass interactions in the lanthanum(III) biosorption on Sargassum sp. using SEM/EDX, FTIR, and XPS: Preliminary studies. Chemical Engineering Journal 239 (2014): 381-391.
[95] Sunding, M.F., Hadidi, K., Diplas, S., Løvvik, O.M., Norby, T.E., and Gunnæs, A.E. XPS characterisation of in situ treated lanthanum oxide and hydroxide using tailored charge referencing and peak fitting procedures. Journal of Electron Spectroscopy and Related Phenomena 184(7) (2011): 399-409.
[96] Gurgul, J., Rinke, M.T., Schellenberg, I., and Pöttgen, R. The antimonide oxides REZnSbO and REMnSbO (RE = Ce, Pr) – An XPS study. Solid State Sciences 17 (2013): 122-127.
[97] Yaremchenko, A.A., Patrício, S.G., and Frade, J.R. Thermochemical behavior and transport properties of Pr-substituted SrTiO3 as potential solid oxide fuel cell anode. Journal of Power Sources 245 (2014): 557-569.
[98] Borchert, H., et al. Electronic and Chemical Properties of Nanostructured Cerium Dioxide Doped with Praseodymium. The Journal of Physical Chemistry B 109(12) (2005): 5728-5738.
[99] Wang, X., Zhang, C., Zang, G., Lv, S., and Li, L. Effect of doping content of Pr ions on oxygen vacancies in SrTiO3 films. Journal of Alloys and Compounds 637 (2015): 277-280.
[100] Gheorghe, N.G., Lungu, G.A., Husanu, M.A., Costescu, R.M., Macovei, D., and Teodorescu, C.M. Structure, reactivity, electronic configuration and magnetism of samarium atomic layers deposited on Si(001) by molecular beam epitaxy. Applied Surface Science 267 (2013): 106-111.
[101] Nguyen, T.D., Dinh, C.T., and Do, T.O. Monodisperse samarium and cerium orthovanadate nanocrystals and metal oxidation states on the nanocrystal surface. Langmuir 25(18) (2009): 11142-8.

[102] Nguyen, T.-D., Mrabet, D., and Do, T.-O. Controlled Self-Assembly of Sm2O3 Nanoparticles into Nanorods: Simple and Large Scale Synthesis using Bulk Sm2O3 Powders. The Journal of Physical Chemistry C 112(39) (2008): 15226-15235.
[103] Jin, F., Shen, Y., Wang, R., and He, T. Double-perovskite PrBaCo2/3Fe2/3Cu2/3O5+δ as cathode material for intermediate-temperature solid-oxide fuel cells. Journal of Power Sources 234 (2013): 244-251.
[104] Bian, L.Z., Wang, L.J., Chen, N., Li, F.S., and Chou, K.-C. Enhanced performance of La0.7Sr0.3Fe0.9Ni0.1O3 cathode by partial substitution with Ce. Ceramics International.
[105] Lee, T.-H., et al. Robust NdBa0.5Sr0.5Co1.5Fe0.5O5+δ cathode material and its degradation prevention operating logic for intermediate temperature-solid oxide fuel cells. Journal of Power Sources 331 (2016): 495-506.
[106] Wu, X., et al. Stability and electrochemical performance of lanthanum ferrite-based composite SOFC anodes in hydrogen and carbon monoxide. Electrochimica Acta 208 (2016): 164-173.
[107] Falcón, H., Barbero, J.A., Alonso, J.A., Martínez-Lope, M.J., and Fierro, J.L.G. SrFeO3-δ Perovskite Oxides: Chemical Features and Performance for Methane Combustion. Chemistry of Materials 14(5) (2002): 2325-2333.
[108] Kochur, A.G., et al. Chemical bonding and valence state of 3d-metal ions in Ni1−xCoxCr2O4 spinels from X-ray diffraction and X-ray photoelectron spectroscopy data. Journal of Electron Spectroscopy and Related Phenomena 195 (2014): 208-219.
[109] Aghavnian, T., et al. Determination of the cation site distribution of the spinel in multiferroic CoFe2O4/BaTiO3 layers by X-ray photoelectron spectroscopy. Journal of Electron Spectroscopy and Related Phenomena 202 (2015): 16-21.
[110] Meza, E., Ortiz, J., Ruíz-León, D., Marco, J.F., and Gautier, J.L. Lithium-nickel cobalt oxides with spinel structure prepared at low temperature. XRD, XPS, and EIS measurements. Materials Letters 70 (2012): 189-192.
[111] Kim, J.H. X-ray photoelectron spectroscopy analysis of (Ln1−xSrx)CoO3−δ (Ln: Pr, Nd and Sm). Applied Surface Science 258(1) (2011): 350-355.
[112] Viola, M.C., et al. Structure and Magnetic Properties of Sr2CoWO6: An Ordered Double Perovskite Containing Co2+(HS) with Unquenched Orbital Magnetic Moment. Chemistry of Materials 15(8) (2003): 1655-1663.
[113] Thota, S., Kashyap, S.C., Sharma, S.K., and Reddy, V.R. Cation distribution in Ni-substituted Mn0.5Zn0.5Fe2O4 nanoparticles: A Raman, Mössbauer, X-ray diffraction and electron spectroscopy study. Materials Science and Engineering: B 206 (2016): 69-78.
[114] Srivastava, N., Shripathi, T., and Srivastava, P.C. Core level X-ray photoelectron spectroscopy study of exchange coupled Fe/NiO bilayer interfaced with Si substrate (Fe/NiO–nSi structure). Journal of Electron Spectroscopy and Related Phenomena 191 (2013): 20-26.
[115] Kim, H., Lee, K., Kim, S., and Kim, Y. Fluorination of free lithium residues on the surface of lithium nickel cobalt aluminum oxide cathode materials for lithium ion batteries. Materials & Design 100 (2016): 175-179.

[116] Kovács, G.J., Bertóti, I., and Radnóczi, G. X-ray photoelectron spectroscopic study of magnetron sputtered carbon–nickel composite films. Thin Solid Films 516(21) (2008): 7942-7946.
[117] Niwa, E., Uematsu, C., Mizusaki, J., and Hashimoto, T. Oxygen nonstoichiometry and electrical conductivity of LaNi0.6Fe0.4O3 − δ at high temperatures under various oxygen partial pressures. Solid State Ionics 274 (2015): 119-122.

จุฬาลงกรณ์มหาวิทยาลัย
Chulalongkorn University

APPENDIX

จุฬาลงกรณ์มหาวิทยาลัย
Chulalongkorn University

APPENDIX A

Ionic radius of related metal ions with their corresponding coordination numbers. [61]

Table A.1

Metal	Oxidation State	Coordination Number	Ionic Radius (Å)
La	3+	6	1.032
		8	1.160
		9	1.216
		10	1.270
Pr	3+	6	0.990
		8	1.126
		9	1.179
	4+	6	0.850
		8	0960
Sm	3+	6	0.958
		8	1.079
		9	1.132
Fe	3+	4	0.490
		5	0.580
		6 (LS)	0.550
		6 (HS)	0.645
	4+	6	0.585
Co	2+	4	0.580
		5	0.670
		6 (LS)	0.650
		6 (HS)	0.745
	3+	6 (LS)	0.545
		6 (HS)	0.610
Ni	2+	4	0.550
		5	0.630
		6	0.690
	+3	6 (LS)	0.560
		6 (HS)	0.600

จุฬาลงกรณ์มหาวิทยาลัย
Chulalongkorn University

VITA

Mister Kittiwat Kamlungsua was on May 19, 1991 in Samutprakarn, Pathumthani. He graduated with Bachelor Degree in 2012 and continued his Master Degree in Program of Chemistry (Inorganic Chemistry), Faculty of Science, Chulalongkorn University. He also completed his Master Degree in 2016 and will be pursuing his Doctor of Philosophy at Nanyang Technological University. During his study at Chulalongkorn University, he received a grant from Science Achievement Scholarship of Thailand (SAST) and participated in DESY Summer Student 2013 in Hamburg, Germany.

จุฬาลงกรณ์มหาวิทยาลัย
Chulalongkorn University